

**Chaotic Advection and Mixing in a Western Boundary Current-
Recirculation System: Laboratory Experiments**

By

Heather E. Deese

B.S., Georgetown University, 1998

Submitted in partial fulfillment of the requirements of the degree of

Master of Science

at the

MASSACHUSETTS INSTITUTE OF TECHNOLOGY

and the

WOODS HOLE OCEANOGRAPHIC INSTITUTION

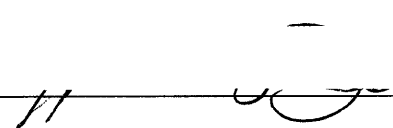
February 2001

© 2000 Heather E. Deese


All rights reserved.

The author hereby grants to MIT and WHOI permission to reproduce paper and electronic copies of this thesis in whole or in part and to distribute them publicly.

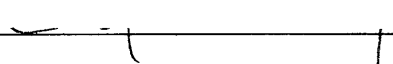
Signature of Author

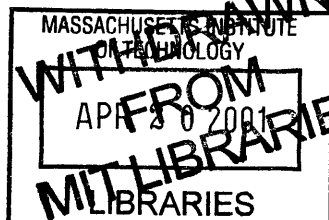

Joint Program in Oceanography
Massachusetts Institute of Technology
and Woods Hole Oceanographic Institution
December, 28 2000

Certified by


Larry Pratt
Thesis Supervisor

Accepted by


Carl Wunsch
Chair, Joint Committee for Physical Oceanography
Massachusetts Institute of Technology
and Woods Hole Oceanographic Institution





Chaotic Advection and Mixing in a Western Boundary Current-Recirculation System: Laboratory Experiments

By

Heather E. Deese

Submitted to the Department of Earth, Atmospheric, and Planetary Sciences at MIT and the Department of Physical Oceanography at WHOI on December 28, 2000 in partial fulfillment of the requirements for the degree of Master of Science in Physical Oceanography.

Abstract:

I study the exchange between a boundary current and flanking horizontal recirculations in a 'sliced-cylinder' rotating tank laboratory experiment. Two flow configurations are investigated: a single recirculation and a double, figure-8, recirculation. The latter case involves a hyperbolic point, while the former does not. I investigate the stirring and mixing under both steady and unsteady forcing.

I quantify the mixing in each case using effective diffusivity, κ_{eff} , and a corollary effective length, L_{eff} , as derived by Nakamura (1995, 1996). This approach involves diagnosing the geometric complexity of a tracer field. Geometric complexity is indicative of advective stirring. Because stirring creates high gradients, flows with high advective stirring also have high diffusion, and stronger overall mixing. I calculate effective length from images of dye in the tank and find much higher values of L_{eff} in the unsteady hyperbolic cases than in the other cases.

Slight unsteadiness in flows involving hyperbolic points gives rise to a chaotic advection mechanism known as 'lobe dynamics'. These lobes carry fluid in and out of the recirculations, acting as extremely effective stirring mechanisms. I demonstrate the existence of these exchange lobes in the unsteady hyperbolic (figure-8) flow. The velocity field in the tank is calculated utilizing particle image velocimetry (PIV) techniques and a time series $U(t)$ demonstrates the (forced) unsteadiness in the flow. Images of dye in the tank show exchange lobes forming at this same forcing period, and carrying fluid in and out of the recirculation.

Based on the results of these experiments, I am able to confirm that, at least in this controlled environment, basic geometry has a profound effect on the mixing effectiveness of a recirculation. I demonstrate radically increased stirring and mixing in the unsteady hyperbolic flow as compared to steady flows and flows without hyperbolic points.

Recirculations are ubiquitous in the world ocean; they occur on a variety of scales, in many different configurations, and at all depths. Some of these configurations involve hyperbolic points, while others do not. Chaotic advection via lobe exchange may be an important component of the mixing at multiple locations in the ocean where hyperbolic recirculation geometries exist.

Thesis Supervisor: Larry Pratt

Title: Senior Scientist, Physical Oceanography Department, Woods Hole Oceanographic Institution

I. Introduction:

The motivation for this work came from the realization that some basic recirculation geometries associated with enhanced mixing due to chaotic advection appear in multiple locations in the oceans. Analytical and numerical studies of geometries involving hyperbolic points have highlighted the importance of a chaotic advection mechanism known as ‘lobe dynamics’ (e.g. Rom-Kadart, et al. 1990, Wiggins 1992, and Miller, et al. 1997). Hyperbolic geometries arise wherever recirculations (of the same sign) occur next to each other. Exchange lobes arise whenever a flow with a hyperbolic point becomes slightly unsteady. These lobes carry fluid in and out of the recirculations, acting as extremely effective stirring mechanisms. Because stirring creates high gradients, flows with high advective stirring also have high diffusion, and stronger overall mixing. Lobe exchange may be an important component of the mixing at multiple locations in the ocean where hyperbolic recirculation geometries exist.

Recirculations are ubiquitous in the world ocean; they occur on a variety of scales, in many different configurations, and at all depths. Some of these configurations involve hyperbolic points, while others do not. There appear to be a series of recirculations along the course of the Deep Western Boundary Current (DWBC)¹ in the North Atlantic and these were the particular features that sparked my interest. In some locations two or more recirculations line the course of the DWBC, with hyperbolic points between each pair. These recirculations may have a profound effect on the path a parcel of deep water takes along the boundary (Fine, 1995). We would like to understand the effects of the recirculations in order to more fully describe the information pathways and delay times in the abyssal oceans and their role in the Meridional Overturning Circulation (MOC). In addition to this particular deep application, many questions remain about the effects of surface or mid-depth recirculations in the oceans. I wondered whether I could say something about the mixing that would occur in the region of a recirculation based on whether or not the basic geometry involved a hyperbolic point.

I study the exchange between a boundary current and flanking horizontal recirculations with and without hyperbolic geometries. Based on the results of a series of

¹ I use ‘dwbc’ or ‘dbc’ to specify the general phenomenon of deep (western) boundary currents and ‘DWBC’ to specify the Deep Western Boundary Current in the North Atlantic.

laboratory experiments, I am able to confirm that, at least in this controlled environment, basic geometry has a profound effect on the mixing effectiveness of a recirculation.

I use a ‘sliced-cylinder’ rotating tank to produce the boundary current and recirculations in the laboratory. The single layer of fluid displays a slow interior flow and a fast ‘western’ boundary current due to the stress of a differentially rotating lid and the topographic beta effect of a sloped tank bottom. At low lid rotation rates a single ‘Munk’ recirculation lies between the boundary current and the interior (Figure I1a). At higher forcing a second, ‘inertial’ recirculation forms ‘north’ of the first, resulting in a double recirculation, figure-8, geometry with a hyperbolic point (Figure I1b). I investigate both steady and unsteady cases (the unsteady cases are forced by adding a slight oscillation to the lid rotation).

I diagnose mixing in each case using effective diffusivity, κ_{eff} , and a corollary effective length, L_{eff} , as derived by Nakamura (1995, 1996). This approach involves diagnosing the geometric complexity of a tracer field. Geometric complexity is indicative of advective stirring, and strong stirring results in increased diffusive mixing. This has been demonstrated numerically by Nakamura (1996) and employed by Nakamura and others to diagnose mixing in the atmosphere (Nakamura 1995, Nakamura & Ma 1997, Haynes & Shuckburgh 2000). In this work I calculate effective length from images of dye in the tank.

In addition, I demonstrate the underlying lobe dynamics that I believe account for the higher effective diffusivity in the flow with a hyperbolic point. The velocity field is calculated utilizing particle image velocimetry (PIV) techniques, and a time series $U(t)$ demonstrates the (forced) unsteadiness in the flow. Images of dye in the tank show exchange lobes forming at this same forcing period, and carrying fluid in and out of the recirculation.

I am not attempting to model a particular geographical region, but instead to investigate generic flow geometries that occurs in many locations. (In the section on oceanographic observations I highlight the shared characteristics which contributed to our choice of geometries.) I do not investigate the cause of these deep recirculations, but rather attempt to elucidate their effects. I essentially create a model in the laboratory tank, and study the fundamental differences between two generic recirculation configurations.

My final goal is to learn something about the nature of exchange between the wbc, the recirculation(s), and the interior. What can I say about the mixing along the edges of

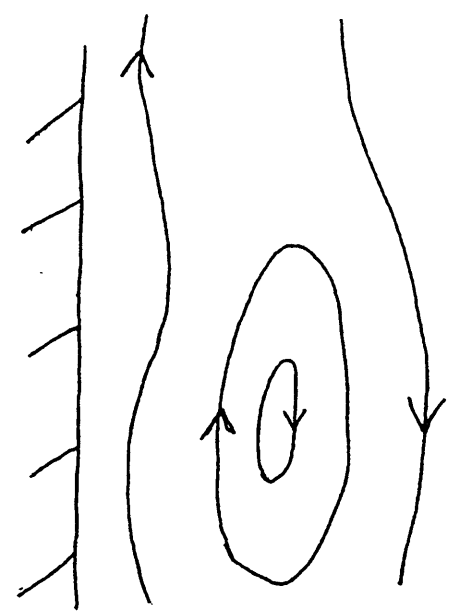
the recirculation(s)? Are particles more likely to exit back into the boundary current or into the interior flow to the east? How quickly and effectively do recirculations homogenize fluid trapped inside? How does altering the geometry of the recirculation region affect the mixing characteristics of the flow? What are the dynamics that underlie the mixing?

The rest of this work is presented in the following way. Sections II-III present background information and relevant oceanographic observations of the deep recirculations. In section IV I outline the theory of lobe dynamics, which combined with the observations determined our choice of flow geometries. Section V includes background information on our laboratory apparatus and procedures. The velocity calculation and dye pictures depicting the exchange lobes are presented in sections VI and VII, respectively. Section VIII contains the calculations of effective diffusivity, with further notes on the effects of the exchange lobes. In Section IX I summarize my findings and suggest directions for further work in the laboratory. In addition I briefly discuss the relevance to oceanographic situations and possible ways to incorporate the concepts of lobe dynamics and effective diffusivity into analysis of oceanographic observations.

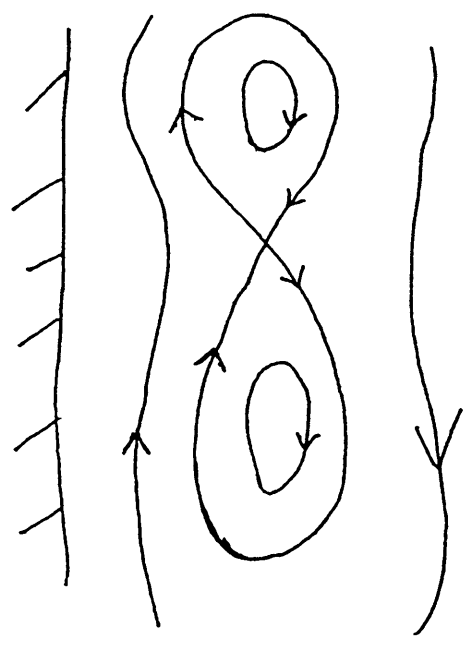
Figure I1: Schematic illustration of the two recirculation configurations investigated. Panel a: a single recirculation lies between a western boundary current and an interior flow. In the laboratory this 'Munk' recirculation represents the non-hyperbolic case. Panel b: a double, figure-8, pair of recirculations. This is obtained in the laboratory in a flow regime where the Munk recirculation and an 'inertial' recirculation coexist. A hyperbolic point is visible where the streamlines outlining the recirculations intersect.

a.

Figure I1



b.



II. Background:

Diagnosing the mixing around all types of recirculations is important, but understanding the recirculations along the deep boundary currents is an especially difficult and significant problem. This is because the deep boundary currents and surrounding features comprise the lower branch of the Meridional Overturning Circulation (MOC)¹. This circulation consists of the poleward transport of warm water near the surface and the equatorward flow of cold water at greater depths. The transformation of this surface water into deep water requires rare atmospheric and oceanic conditioning, and thus occurs sporadically and in only a few locations. It is the deep boundary currents that transport both this newly ventilated water and older deep waters throughout the world oceans.

The question of the content and characteristics of the deep transport system is especially important because these deep currents carry information about the climate conditions at the time of their formation and will eventually feed back this information into the world's surface waters. As this water upwells thousands of years later it will affect all sorts of systems from biological communities to weather patterns and the global climate.² We would like to understand the information pathways and delay times in the abyssal oceans so that we can describe and predict the Meridional Overturning Circulation more completely.

One analogue to these laboratory experiments is the important, but little understood, horizontal recirculations that flank the paths of the deep boundary currents. The most well-studied part of the deep ocean is the North Atlantic, and throughout this region investigators have identified deep boundary currents lined by recirculations of various sizes (McCartney 1992, Schmitz & McCartney 1993, Johns, et al. 1997, Lavender, et al. 2000). (see figures O1, O2, O3) Although for a combination of historical, political, social, and economic reasons, much less work has been done in the other oceans, some of the observations along other dwbcs indicate similar patterns. (for Pacific flows see Wijffels, et al. 1998. For South Atlantic flows see Stephens & Marshall 2000 and Spall 1994)

¹ I adopt Munk and Wunsch (1998) suggestion and use the term Meridional Overturning Circulation (MOC) instead of Thermohaline Circulation. The authors hold that since the forcing of this vertical overturning circulation is not necessarily exclusively thermohaline, the MOC is a more appropriate term.

² The time it takes deep water to upwell and effect surface waters is still not well known, in the case of some water that transits the world oceans, it could be much longer than O(1000) years. For newly formed water in the 'shallow' branch of the DWBC, the time could be much less than O(1000) years.

There are a number of ways in which recirculations may affect the transport of deep water and its interaction with other waters. Recirculations presumably modify both the time it takes a water parcel to move along the boundary and the exposure of that parcel to other water masses. Parcels of water which peel off from a wbc into a recirculation and spend some period of time 'trapped' there before returning to the core flow take a much longer time to move along the boundary. In addition they are exposed to a different mixing environment than they would have been otherwise; both the mixing intensity and neighboring water masses are presumably different due to the presence of the recirculation (Fine 1995).

Recirculations could therefore explain the disparity between the travel time one expects along the boundary from direct current measurements and the age of the deep water along its track as indicated by tracer fields (Fine, *ibid.*). Recirculations also seem to explain the regions of homogenized characteristics found at various locations alongside the dbcs (Fine, *ibid.*). In addition, the spatial distribution of vertical mixing in the oceans is still largely unknown, and recirculations may play some role in determining that pattern. An extreme example arises in the mid-depth water of the Labrador Sea. Various investigators have postulated that deep convection occurs in particular locations because water is trapped there for some time by horizontal recirculations. The air-sea dynamics work more effectively on this trapped water, conditioning it for convection through cooling (Clarke & Gascard 1983 and Lavender, et al. 2000).

We would like to answer some basic questions about this type of recirculation. How much time is a parcel likely to spend trapped in a recirculation? Are trapped parcels more likely to end up exiting into the interior flow or into the boundary current? How quickly and effectively do recirculations act to homogenize any fluid trapped inside? Do recirculations with certain underlying geometries tend to entrain and mix more than others? What are the mechanisms by which all of this exchange occurs? We must find answers to these questions before we can build even a basic understanding of the deep branch of the meridional overturning circulation.

Diagnosing the rate of feedback via the deep transport system is especially important because deep water formation is highly time dependent. For example, during the early 1990s there was extremely high production of Labrador Sea water in the northern North Atlantic. A series of observational studies have tracked this strong pulse of newly formed deep water as it has propagated down the course of the DWBC which hugs the

coast of North America (Curry, et al. 1998 and Molinari, et al. 1998). Others have investigated the interplay between this formation event and the variability in other deep water types (i.e. overflow water, etc. see Pickart, et al. 1999). While still others have investigated the connection between the strength of deep water formation and the strength of the overturning circulation (Mauritzen & Hakkinen 1999 and Munk & Wunsch 1998). In order to fully understand the long term effects of the time variability in the MOC we must be able to predict when anomalous signals will affect the surface properties of the oceans. This requires piecing together a better understanding of the deep transport system. If we clearly diagnose the delivery system, we may be able to develop powerful predictive capabilities.

III. Oceanographic Observations:

In terms of oceanographic observations I define a horizontal recirculation as a region where some offshore (or occasionally inshore) return flow transports water derived from the boundary current water as shown schematically in Figure II. In many cases deep recirculations have been postulated based on characteristics of the deep boundary current (dbc) in some region (i.e. otherwise inexplicable changes in transport and or tracer signals along a section of the boundary current). In most locations return flow has not yet been measured. In a few cases the return flow has been measured and I describe these cases below. This physical evidence is often bolstered by details of tracer distribution, which can indicate recirculations where tracer signals characteristic of the boundary current stretch toward the interior. These signals can be interpreted as indicating the area of a recirculation adjacent to the boundary current (e.g. Fine and Molinari, 1988).

Tracer data has also indicated some large-scale effects which have been linked to recirculations. Namely, the tracer-derived ages for the Deep Western Boundary Current are much older than the time it would take a parcel to move along the boundary at the observed current velocities. In her review of relevant tracer measurements, Fine (1995) notes that the tracer-derived DWBC velocities are $O(1 \text{ cm/s})$ while the observed DWBC velocities are $O(10-50 \text{ cm/s})$. Despite high uncertainty in the tracer-derived \bar{u} , this order of magnitude difference indicates that either significant mixing or horizontal recirculation (or more likely, both) are involved in the transport of parcels along the boundary.

The deep recirculations seem to occur on a variety of scales and for various reasons. Many of the smaller ‘meso-scale’ recirculations, $O(100-400 \text{ km})$, appear to be due to interactions of the flow with local topography, but the dynamics of other meso-scale recirculations are mysterious. The larger, ‘basin-scale’ recirculations, $O(500-1000 \text{ km})$, fill many of the abyssal plains which comprise the deep ocean floor. In the North Atlantic, these abyssal plains typically stretch from the continental margin to the mid-ocean ridge in

the zonal direction and are bounded in the meridional direction by smaller ridges or other topographic barriers. In some locations there appear to be both meso-scale and basin-scale recirculations in play, with some deep water recirculating close to the boundary and some recirculating much further from the boundary. In all of these locations there is some net throughflow along the boundary in the deep boundary current, but the characteristics of the water that exits the region may be strongly affected by the presence of the various recirculations.

The majority of the observations recounted here supply indicative, but not conclusive, evidence of recirculations. In a few cases, repeated sets of measurements of different kinds (moorings, hydrographic surveys, floats, and tracers) provide a preponderance of evidence for recirculation along the DWBC. The most well documented case of a recirculation abutting a deep boundary current is in the Abaco region ~ 24-30N in the western Atlantic. I review the work in this region below, after summarizing some observations in other areas.

Recent work in compiling float data into Eulerian fields in the Irminger and Labrador Basins has highlighted meso-scale cyclonic recirculations that are embedded in the larger, basin-scale looping of the DWBC as it enters and leaves each basin (Lavender, et al. 2000). The streamlines of this flow are reprinted by permission in Figure O1. The authors were able to diagnose the mean, mid-depth, horizontal circulation by compiling drift results from 200 PALACE and SOLO floats at 400, 700, and 1500 m depth. The resulting velocity field contains a series of cyclonic recirculations with the return flow in the interior ~1/4 the speed of the boundary currents, which is 12 cm/s maximum, and the total width of the recirculations is O(1-2) times the width of the boundary current. The highest velocities and the only clear time dependence (an annual signal in the transport) occurred in the cyclonic gyre north of the Flemish Cap (50N, 47W) and the figure-eight pair of recirculations east of Greenland (61N, 37W). Current meter results also show indications of return flows offshore of the Labrador and Greenland currents (Pickart, et al. 2000 and Clarke & Gascard 1983).

Lavender, et al. 2000 also note other phenomena associated with these recirculations. This first is that deep mixed layers and sluggish velocities O(1.5 cm/s) occurred during winter time in the region of a cyclonic recirculation in the western Labrador sea near 56.5N. This is a region where other investigators have found Labrador Sea Water

formation (Pickart, 1998). These results support the suggestion by Clarke and Gascard (1983) that deep water could be formed in a localized, offshore, cyclonic recirculation.

The second note is that extremely complex trajectories were found near the Flemish Cap. There are multiple flow components here, as the Labrador Current looping around the Cap from the north encounters the North Atlantic Current entering the region from the southwest. The float trajectories from the middle and deep layers bifurcate in this region, some recirculating north back into the Labrador Sea, a number heading east towards the Mid-Atlantic Ridge, and one continuing south (presumably in the core of the DWBC). The resulting “rapid exchange between the boundary current and offshore waters” (Lavender, et al. 2000, p.68) may be due to a hyperbolic point where the interior recirculation of the Labrador Sea encounters the larger-scale flow.

A number of basin-scale recirculations have been proposed, and some of these are shown schematically in Figure O2. I have sketched this cartoon based on the work outlined below; I have reprinted the bottom topography (with permission) from McCartney (1992). Examples include a recirculation consisting of both DWBC water and Antarctic Bottom Water (AABW) in the Guiana basin and a series of recirculations of AABW and Iceland-Scotland Overflow Water (ISOW) in the basins of the eastern North Atlantic (Van Aken 2000; McCartney 1992; Johns, et al. 1993; Schmitz & McCartney 1993). Investigators have proposed multiple explanations for the existence of these recirculations, including large-scale topographic beta effects, instability of the boundary current, and specified, non-uniform upwelling. (Nof & Olson 1993; Speer & McCartney 1992; Kawase 1993; Spall 1994).

McCartney (1992) employs hydrographic stations in the Madiera Basin to identify northward flow in the east at 2.2 Sv with a return flow southward in the west of 0.6 Sv, resulting in 1.6 Sv of throughflow of the coldest bottom water. Further north McCartney (1992) combines multiple hydrographic studies and a few current meter results in his diagnosis of 3.9 Sv flowing northward along the eastern edge of the West European basin with 1 Sv recirculating at the western edge of that basin.

Further work with inverse models (Gana and le Provost, 1993) and detailed water mass composition analysis (Van Aken, 2000) has bolstered the evidence for these cyclonic recirculations. Van Aken (2000) substantiates evidence for recirculations in Madiera and West European Basins by tracking the southward influence of ISOW (Iceland-Scotland

Overflow Water) as far south as the Madeira Basin at 30N, and proposes a similar feature in the Iberian Basin.

In addition to these large scale recirculations, the deep boundary current in the North Atlantic is characterized by huge meanders or intrusions into the subpolar basins. In all four northern basins (Rockall Trough, Iceland Basin, Irminger Basin, and Labrador Sea) McCartney (1992) identifies the signature of deep boundary current water looping in and out of the basins in a cyclonic manner. He does not identify these loops as closed recirculations, but more recent work indicates a closed recirculation is likely in the Iceland Basin (personal communication, Cecilie Mauritzen).

Another basin-scale recirculation (possibly made up of a series of recirculations) was predicted between the equator and 30N in the western Atlantic by Schmitz & McCartney 1993. This would involve both NADW and AABW contributing to a cyclonic recirculation, with northward flow along the western flank of the mid-ocean ridge and southward flow (in the DWBC) along the continental margin. Observational work in progress (Guiana Abyssal Gyre Experiment, McCartney and Mauritzen, co P.I.s) aims at directly measuring the northward flow. There are also indications of basin-scale recirculating components in the Canary Basin/Gambia Abyssal Plain and Brazil Basin. (Stephens & Marshall, 2000).

In addition to these deep recirculations, there are many surface intensified recirculations, some of which have very deep signatures stretching almost throughout the entire water column. Examples include: the Great Whirl in the Gulf of Aden off Somalia, the Mann Eddy in the Newfoundland basin, the Alboran Gyre north of Morocco in the Mediterranean Sea, the inertial gyres that lie on either side of the Gulf Stream between Cape Hatteras and Grand Banks and a similar, but smaller, feature to the south of the Kurishio. Many investigators have studied the recirculations on either side of the Gulf Stream, including the entrainment of the DWBC water as it passes through the region (Hogg, N.G. 1992, Spall 1996 (I&II), and Bower and Hunt 1999 (I&II)). The recirculations in this region are extremely complex due to the interaction of intense boundary currents traveling in different directions at different depths, and presumably involve a number of hyperbolic points, so that chaotic advection may play an important role in the regional mixing.

MESO-SCALE CASE STUDY: ABACO

The Abaco area east of the Bahamas is a well studied region that demonstrates the complex structure of the DWBC. The results from a long-standing current meter array across the DWBC at 26.5N demonstrated a surprisingly high total transport which hinted at an offshore recirculation (Lee, et al. 1996). Additional work, in the form of hydrographic and chemical tracer surveys, PEGASUS current profiles, moored measurements, dropsondes, and RAFOS floats, has refined our understanding of the circulation in this region (Fine & Molinari 1988; Leaman & Vertes 1996; Johns, et al. 1997). This work has elucidated meso-scale recirculations and hinted at basin-scale recirculations that contribute to the high mass flux along the boundary. The many types of measurements in this area have allowed investigators to state with confidence that this region is characterized by enhanced advective and diffusive mixing: “the DWBC recirculation gyres, and enhanced mixing due to topographic influences, appear to be an effective means for ventilation of the interior and dilution of the DWBC tracer concentrations” (Johns, et al. 1997, p. 2206) Figure O3 presents approximate streamlines in the region showing the local, meso-scale recirculation (panel a from Johns, et al. 1997, reprinted with permission) and the bottom topography in the region (panel b from Leaman and Vertes, et al. 1996, reprinted with permission, I have added a bold line at the 4500m isobath).

Lee, et al. (1996) present the cumulative data of 5.8 years of moored current meter measurements from a section along 26.5 N. They calculate a total southward transport of 40 ± 13 Sv (Sv = Sverdrup is defined as a million cubic meters) in the DWBC.¹ Of this total southward boundary flow, they approximate 27 Sv must recirculate somewhere in the western North Atlantic, as only 13 Sv is required to balance the Meridional Overturning Circulation at this latitude.

Johns, et al. (1997) detail the portion of this 27 Sv which is recirculated locally in a meso-scale recirculation (Figure O3a). This recirculation, which the authors diagnose as carrying 12 Sv, spins most strongly over a ‘bump’ in the bottom topography which is the southern extension of the Blake Bahama Outer Ridge (Figure O3b). This bump lies

¹ This total transport was obtained by selectively removing data from periods when the DWBC was in an offshore position. Their moored array, which stretched to 85 km offshore for most of the 5.8 years, and to 125 km offshore for the last two year deployment, did not capture the full core of the DWBC during these offshore excursions. (They find the DWBC ‘offshore’ 32% of the time). They attribute these offshore excursions to interactions with westward propagating baroclinic Rossby waves with a period of 70-100 days. They also find inshore recirculations of northward flow during these periods when the DWBC is located further offshore $O(100 \text{ km})$.

between 74-74.5W and 26-29N. The cyclonic gyre stretches from 75.5W-74W (300 km) and from 25N-29.5N (500 km). Embedded within this recirculation are two smaller features O(100 km) which transport 4-8 Sv each.

Tracer signals in the region also support the local recirculation hypothesis, with a CFC minimum in the DWBC at the depth of the recirculation (indicating dilution by recirculating interior waters) and high CFC and tritium signals stretching into the interior. (Fine 1995; Johns et al. 1997). The tracer signals characterizing DWBC water are clearly found in the cyclonic recirculation where “high but patchy” CFC concentrations suggest “a complicated mixing zone tending toward homogenization” (Johns, et al. 1997, p. 2198).

Lee et al. (1996) also report time dependence with high energy in the 70-100 day period resulting in meandering of the DWBC core. The DWBC meanders from an ‘onshore’ position O(50 km) from the boundary to an ‘offshore’ position O(150 km) on a time scale of 30-150 days. In addition to the variable location, the transport of the DWBC core shows a clear annual cycle, which Lee, et al. explain as a barotropic response to remote wind forcing.

Leaman and Vertes (1996) deployed a total of 23 floats into the three levels of interest in the DWBC and their findings confirm the existence of a local cyclonic recirculation during both phases of the DWBC meanders. This indicates that the time dependence in the core position does not destroy the offshore recirculation. They found floats moved along the boundary at high velocities ($u > 40$ cm/s) in the DWBC core, but were often detoured into recirculations, so that, on average floats moved along the boundary at 1.97 ± 0.19 cm/s (which is similar to the tracer-derived speeds and smaller than the core speeds observed in the DWBC by an order of magnitude).

The authors further found that the San Salvador Spur plays a vital role in steering the flow. Much like in the region of the Flemish Cap mentioned above, Leaman and Vertes (1996) found complicated float paths in the region which indicate high eddy activity and mixing in the flow. Almost all of the floats shoot out from the boundary as the DWBC rounds the Spur and as they do so their paths bifurcate, with floats North of 24.4N recirculating North and neighboring paths, just south of this point veering South. They attribute this evidence of a hyperbolic point in the ocean to a hyperbolic or ‘saddle’ point in the local topography.

In addition to fully investigating this meso-scale feature, Johns, et al. (1997) identify deep flows that suggest connections to basin-scale recirculations. They identify

water that they believe to be DWBC water that was deflected at the Gulf Stream/DWBC crossover and recirculated in the southern inertial gyre before exiting the recirculation and joining back up with the DWBC within the study region. They also note a water mass which may be part of the large-scale recirculation gyre suggested by Schmitz and McCartney (1993). As noted above, this large scale recirculation composed of NADW and AABW (or a series of smaller recirculations) would stretch from the equator to 30N. These elements summed with the meso-scale recirculations would explain the large total long-time flux in the boundary current found in the initial WOCE study.

The important note here is that the underlying geometry of this flow entails an offshore recirculation with two embedded recirculations forming a 'figure-eight' within the larger closed streamlines. As noted in the introduction, this configuration results in a saddle point or hyperbolic point between two recirculations. This double recirculation geometry is one of the configurations I study in the laboratory tank. There is also strong observational evidence for hyperbolic points in the flow where this local meso-scale recirculation meets the interior flow, particularly at the San Salvador spur.

For our purposes the most important observations of this recirculation include its size, transport, and stability. The approximate width of this mesoscale feature is 200-400 km (including the full width of the boundary current in the west). The meridional length-scale is 300-500 km. The embedded recirculations are $O(100 \text{ km})$. The transport is around 12 Sv, with an additional 4-10 Sv due to embedded recirculations. Velocities are approximately 20 cm/s in the DWBC and 4 cm/s in the offshore return flow over the Bahama Ridge.

The stability of the feature is uncertain; when the DWBC core moves offshore an inshore recirculation develops and the measurements of the offshore recirculation during those times are sparse. Nevertheless, it appears from float tracks that the offshore cyclonic recirculation is a persistent feature. The period of these DWBC excursions is on the order of 70-100 days. Which is comparable to a typical 'winding' period $O(150 \text{ days})^2$ for a parcel to circulate once around this meso-scale feature. There is also an annual variability in the DWBC transport: the mean transport is diagnosed at 40 Sv with an annual variation of $\pm 13 \text{ Sv}$.

²I approximate the winding time, $T = O(150 \text{ days})$, by assuming a total path of 800 km, 400 km along the DWBC at 20 cm/s and 400 km in the interior at 4 cm/s.

SUMMARY OF OBSERVATIONS:

I have noted basin scale recirculations in the Madiera, West European, and Iberian basins in the eastern North Atlantic. There may also be closed recirculations as the DWBC loops in and out of the four northern basins of the Atlantic (Rockall, Iceland, Irminger, and Labrador). In addition to the regions mentioned above, there appear to be basin-scale recirculations in the Brazil basin and the Guiana basin in the tropical western Atlantic and there are some indications of recirculating components in the Canary Basin/ Gambia Abyssal Plain.

The evidence for a meso-scale recirculation off Abaco (25-30N) is now very strong, while more recent work indicates a chain of meso-scale recirculations in the Irminger and Labrador basins. Leaman and Vertes (1996) suggest the northern extent of the Windward Isles as another likely location for a deep meso-scale recirculation along the DWBC based on topographic similarity to the Abaco region.

We can glean some basic characteristics of recirculations along the deep boundary currents in the world's oceans from this review of the observational literature. First of all, in the North Atlantic the huge majority of these features appear to be cyclonic and offshore of the deep boundary current. These features occur on two different length scales, on the $O(100)$ km as meso-scale features and $O(500-1000)$ km as basin-scale features. In both cases the recirculating flux tends to be $O(0.5)$ the boundary current flux. The meso-scale recirculations have a width $O(2-3)$ width of the dbc, while the basin-scale recirculations are $O(10)$ width of the dbc.

Little is known about the time dependence and detailed structure of these features. From present measurements, most appear to be persistent features, but their size, transport, and exact location may be time dependent. In the best-observed recirculation region (Abaco) the winding time required for one recirculation is on the order of the strongest time dependent signal in the velocity field. Hyperbolic points presumably exist in some of these regions, but are difficult to observe directly. Float studies in the Abaco region does provides direct evidence for a hyperbolic point in the 'gate' at San Salvador Spur (Leaman and Vertes 1996) and the float study in the Labrador Sea provides similar evidence for a hyperbolic area near the Flemish Cap (Lavender, et al. 2000).

These meso-scale recirculations appear in particularly interesting configurations with respect to lobe dynamics. Two or more recirculating features of the same sign lining

the DWBC would meet at hyperbolic points. If there is time-dependence in the right frequency range, this would indicate that ‘turnstile’ lobe exchange might be an important mixing mechanism in these regions.

Some of these observations indicate single recirculations sitting along a section of the boundary current, while others outline a series of recirculations linked by hyperbolic points. In this study I explore the differences between these two generic geometries and show that in a case with some internal variability the mixing is radically affected by the geometry.

Figure 01

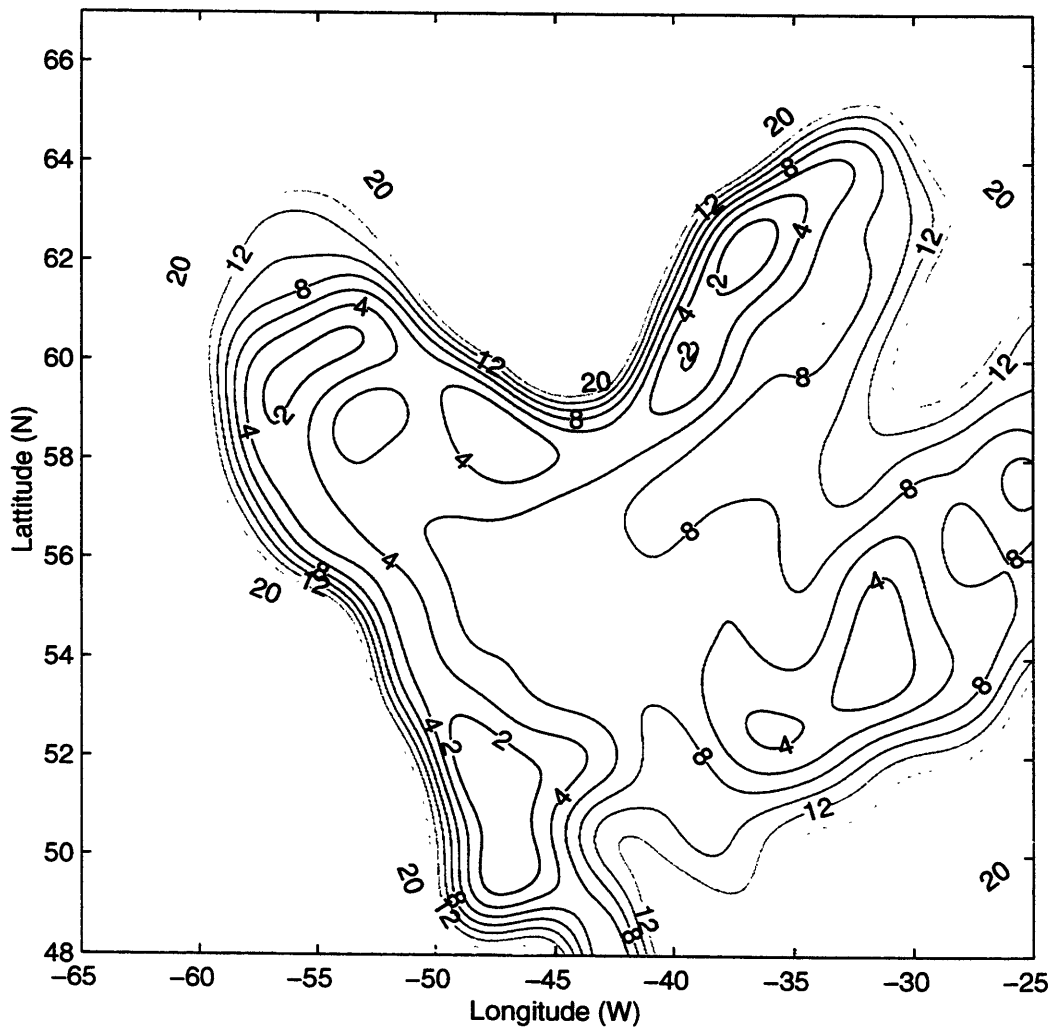


Figure 01 caption: Streamlines in the Labrador and Irminger seas compiled from float tracks by Lavender, et al. (2000) (reprinted with permission) indicate a string of cyclonic recirculations lining the course of the DWBC. Streamlines are calculated from drift tracks of floats at 400, 700, 1500 m depth, all rectified to 700 m using Levitus climatological shear.

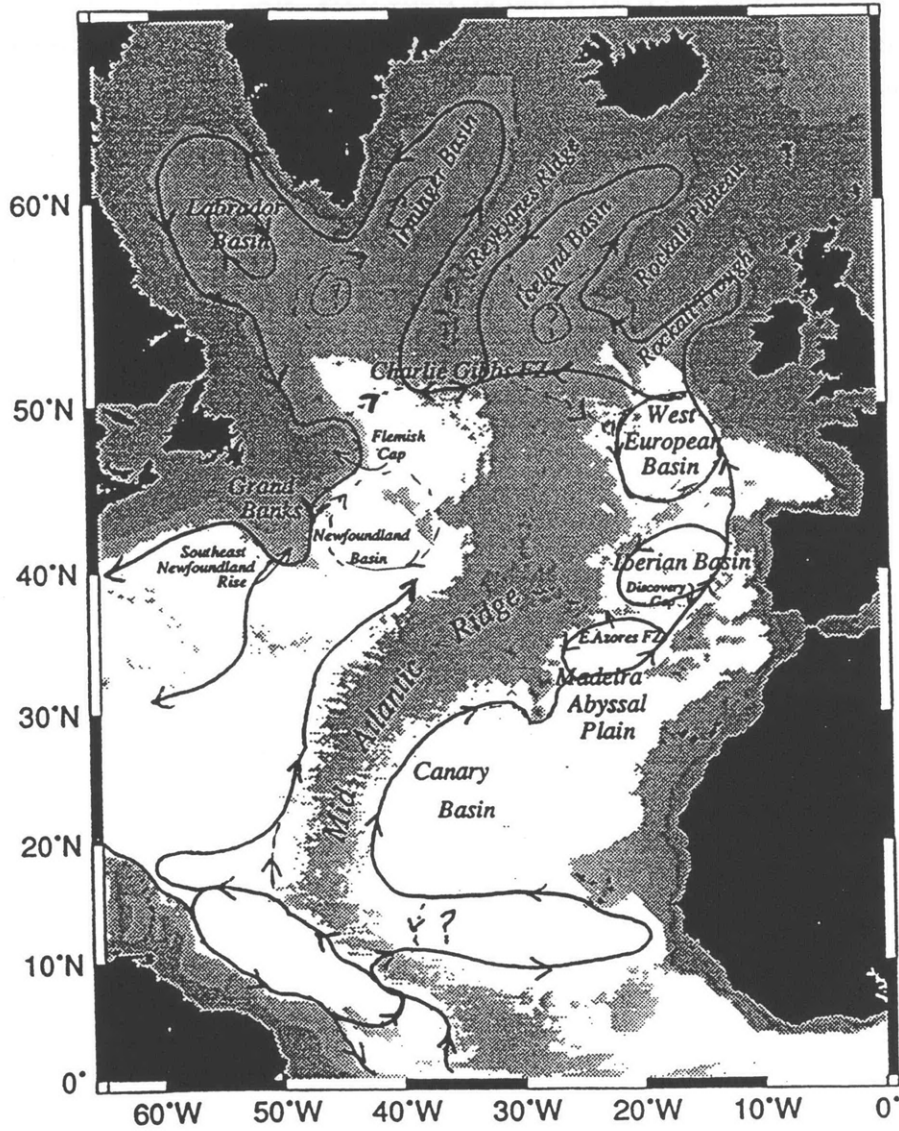
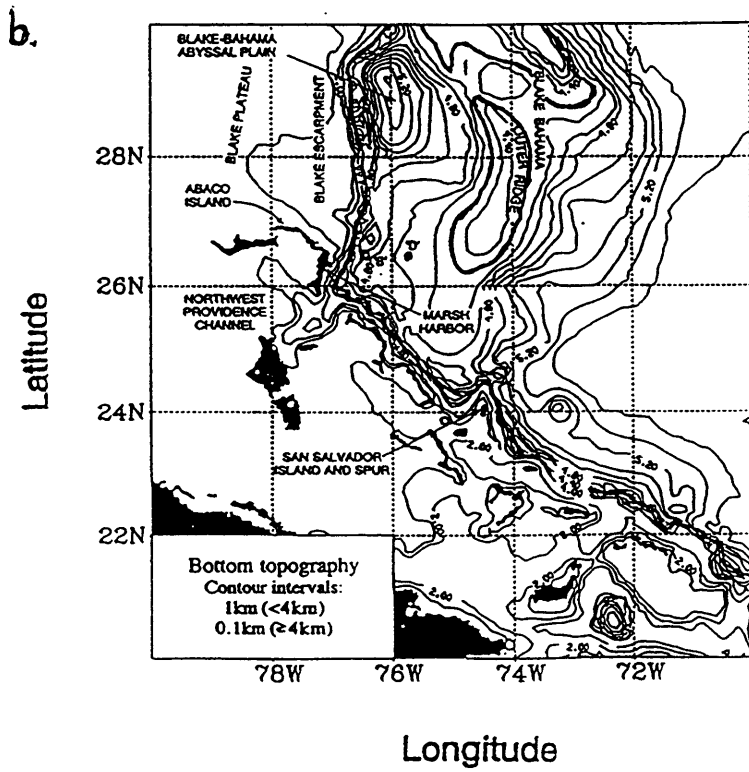
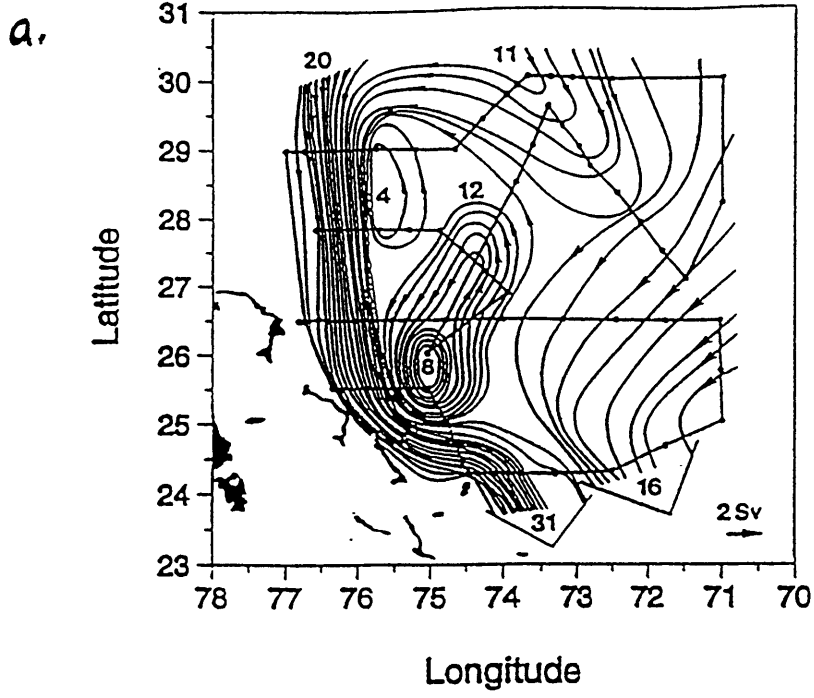


Figure O2 caption: Cartoon of basin scale recirculations in North Atlantic. My sketches incorporate work by McCartney (1992), Gana & Provost (1993), Van Aken (2000), Stephends & Marshall (2000), and personal communication with Mike McCartney with respect to present data analysis of flow in Guiana basin. Topography of basins is from McCartney (1992) (reprinted with permission).

Figure O3 caption : Evidence for meso-scale recirculation in the Abaco region. Panel a: Steady streamlines in the Abaco region approximated by Johns, et al. (1997) incorporating almost ten years of long-time current meter moorings and hydrographic surveys (reprinted by permission). One streamline \equiv 2 Sv. Panel b: Bottom topography in the Abaco region from Lee, et al. (1996) contours are drawn at 100m for the deep regions ($d > 4$ km). I have added a bold contour at 4500m (reprinted with permission).

Figure 03



IV. Dynamical Systems background:

Now that I have reviewed some of the observations which inspired this study, I will outline the work on lobe dynamics which highlights the importance of hyperbolic points in recirculation configurations. This is a brief review, for more detailed explanation of the theoretical basis for lobe dynamics see the text by Wiggins, 1992. The power of dynamical systems theory is in interpreting the extremely complex trajectories that arise in unsteady flows. In any physical system the point of this type of description is to illuminate underlying geometrical structures in the system's phase space. When the behavior of a system becomes too complex to describe directly, a description of these structures and how they transform under varying conditions can be invaluable. In the case of fluid flows this method is especially intuitive, because the phase space of the system is simply physical space; the relevant geometry is demonstrated by the steady streamlines of $\vec{u}(x, y)$.

In some fluid flows, this geometry involves hyperbolic stagnation points. There are two types of stagnation points in two dimensional fluid flows: hyperbolic and elliptic. These are shown in the left and right panels of Figure D1a. At a hyperbolic point fluid is both converging and diverging. At an elliptic point fluid is neither converging nor diverging. In either case, a fluid parcel sitting exactly at a stagnation point has no velocity and will (theoretically) remain at that point for all time. In the case of a hyperbolic point however, all fluid parcels in the nearby area are either approaching or heading away from the hyperbolic point. In fact, the hyperbolic point sits at the intersection of two distinctive material curves which define the directions of strongest convergence and divergence. These are termed the 'stable manifold' and 'unstable manifold', respectively.

These manifolds reveal critical information about a flow. In steady flows the manifolds clearly outline the underlying structures in the phase space (in this case physical space), so I make the following definitions for a steady case. There are two types of hyperbolic geometries: 'heteroclinic' and 'homoclinic' (see Figure D1 b & c). In a heteroclinic geometry, the unstable manifold of a hyperbolic point is also the stable manifold of a neighboring point. One example of this type of geometry arises when a number of recirculations (of the same sign) are aligned next to each other, as in Figure D1b. In a homoclinic geometry the unstable manifold of a hyperbolic point is also the stable manifold of the *same* point. One example of this type of geometry is the 'figure-eight' shown in Figure D1c.

As we can see in Figure D1, these manifolds delineate the boundaries between regions of closed and open streamlines, and are therefore sometimes called ‘separatrices’. Diffusion alone will result in transport across the manifolds in a steady case, so that recirculating and streaming regions are largely isolated. If the system becomes unsteady the manifolds themselves will move resulting in a flux between regions via ‘turnstile’ exchange (explained below) which can result in intense advective stirring. Note that a single recirculation lying towards the interior of a boundary current is bounded by a material curve separating the closed and open streamlines, but there are no hyperbolic points or manifolds (so there will not be turnstile exchange in this case).

Turnstile exchange occurs in unsteady, periodic hyperbolic flows because the bounding manifolds become contorted and tangled. In other words, the stable and unstable manifolds connecting two heteroclinic points or a single homoclinic point no longer overlap, but actually intersect each other an infinite number of times (see Figure D1 d & e). By comparing the tangled manifolds with the ‘undisturbed’ manifolds from the steady flow, we can better understand the chaotic exchange into and out of recirculation regions. (Note in the following when I refer to a recirculation, I mean the regions of closed streamlines outlined by the undisturbed manifolds in a steady state). This process is called ‘lobe dynamics’.

The ‘lobes’ consist of the area between the now tangled manifolds. The fluid within each lobe is mapped in a predictable way into the space delineated by other lobes. In this way fluid is carried into or out of the ‘recirculations’ outlined by the undisturbed manifolds. There are two kinds of lobes. ‘Delivery’ lobes carry fluid into a recirculation and ‘retrieval’ lobes convey fluid out. In these experiments the fluid in each lobe is mapped onto the next lobe of the same type after one period of the unsteady forcing. This process of fluid mapping from inside to outside of a recirculation via lobes is called turnstile exchange.

Figure D1 shows this process in both a homoclinic and heteroclinic geometry. In the heteroclinic case (Figure D1b) the stable manifold of point ‘B’ (bold) and the unstable manifold of point ‘A’ tangle and outline a series of lobes. In the homoclinic case (Figure D1c) the stable manifold of point A (bold) tangles with the unstable manifold of point A. Both geometries entail both kinds of lobes, but the delivery lobes are shaded in the heteroclinic case, while the retrieval lobes are shaded in the homoclinic case. The darkening shading in each indicates the direction of mapping with time ($t = t_0 + nT_F$ where

T_f is the forcing period). Note that lobes are only drawn on one side of the heteroclinic recirculation, but in reality would occur on both.

Another feature of the unsteady flows depicted in Figure D1 are small closed trajectories around the elliptic stagnation points within each recirculation. These are schematic representations of phenomena known as KAM tori. Even when the flow is unsteady the motion of parcels within a KAM tori is regular in that they never leave the area of the torus in the x,y,t space. This means that they are restricted to recirculate around the elliptic point in the x,y plane. The lobes become very contorted within the recirculation, but never enter these KAM tori, leaving a small isolated region immune to the turnstile lobe exchange. The size and location of this isolated region within the original recirculation depends on the type and extent of unsteady forcing. In section VII where I present evidence for lobes in the laboratory flows, I also show some examples of isolated regions that may be associated with KAM tori.

This turnstile mechanism provides us with an intuitive and geometric view into the workings of chaotic advection. It helps explain why chaotic, ‘non-integrable’ regions occur first in the neighborhood of the manifolds, as noted by other investigators (see for example Polvani and Wisdom, 1990). Knowledge of this mechanism could also help us predict mixing in the area of a recirculation, based on whether the basic geometry contains hyperbolic points. If there are hyperbolic points, then in the presence of unsteadiness, lobes will carry fluid in and out of the recirculations acting as extremely effective stirring mechanisms. Although stirring is a reversible process, it creates very high property gradients which enhance irreversible mixing. In flows without hyperbolic points, there will be no manifolds, no lobes, and presumably much less mixing.

It is important to note the type of unsteady flows where this description is useful. Most analytical treatments of unsteady hyperbolic flows assume a time-scale separation between the Lagrangian (recirculation) time scale and the Eulerian time scale associated with the unsteady forcing. This is inherent in the linearization of the equations of motion. In analytical solutions of linearized systems, investigators can solve for the actual locations of the hyperbolic points and the locations of the manifolds (see for example, del-Castillo Negrete and Morrison, 1993). In numerical work, this time scale separation is also often assumed, but is not necessary, as the manifolds are found empirically by marking patches of fluid and the hyperbolic points are assumed to lie at the intersections of these manifolds (see for example, Rogerson, et al. 1999 and Miller, et al. 2001). In the laboratory results

presented here I identify approximate unstable manifolds by injecting a dye streakline into the fluid. I do not have the time scale separation in these experiments. As explained below, the forcing (Eulerian) period is comparable or less than the recirculation (Lagrangian) period. Although I do not have the time scale separation in these experiments, the coherent structures (recirculations and hyperbolic point) are persistent and long-lived relative to the forcing. This implies that in thinking about oceanographic flows, chaotic advection may be important, even in regions where a time scale separation does not exist, as long as the coherent structures and associated hyperbolic points are persistent on a time that is long compared to any unsteadiness. I return to this point in discussing my laboratory results below.

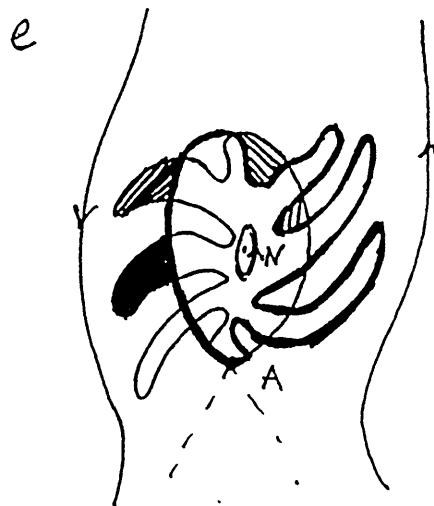
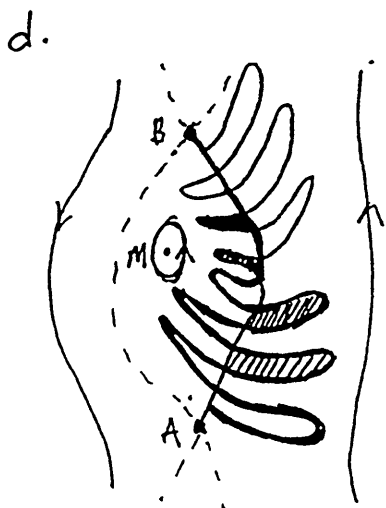
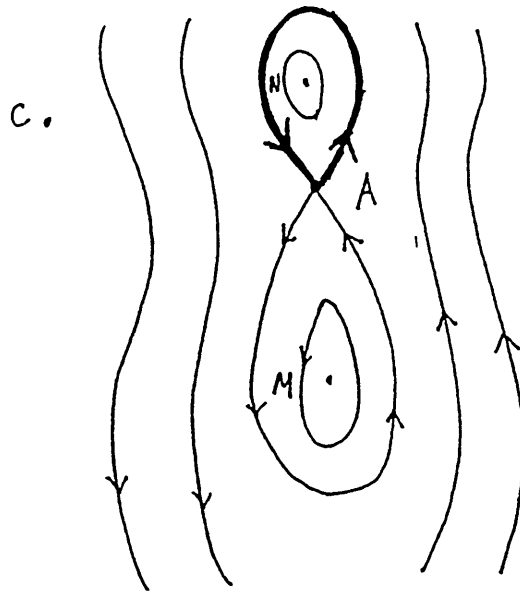
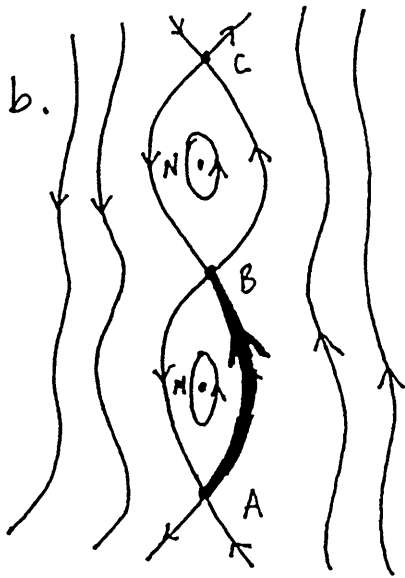
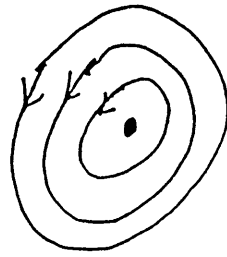
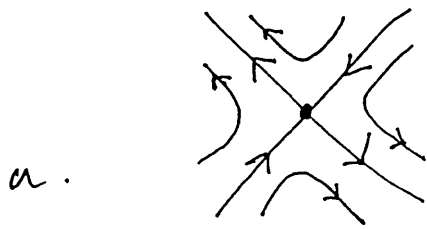
There are some examples of discussions of oceanographic phenomena using the language and processes of dynamical systems theory. Losier, et al. (1997) explore the exchange within the Gulf Stream by comparing RAFOS float trajectories to trajectories of parcels in a numerically simulated flow field. By viewing the float trajectories in a frame of reference moving with the phase speed of the primary Gulf Stream meanders, the authors are able to observe geometric structures in the vicinity of the jet that are predicted by dynamical systems analysis. (These structures look much like the heteroclinic geometry in Figure D1.) Further explorations of this jet geometry were carried out by Miller et al. (1997) and Rogerson, et al. (1999) who explored fluxes between a jet and small recirculations along its path using periodic and aperiodic forcing in numerical models. del-Castillo Negrete and Morrison (1993) utilize a similar jet geometry to explicate the destruction of barriers to mixing in a shear flow. They compare analytical results to a kinematic numerical flow and laboratory experiments.

Miller, et al. (2001) utilize lobe dynamics to analyze a recirculation to the east of a meridional island. The authors employ a numerical model to analyze the role lobes play in potential vorticity exchange and outline the regime in which this type of analysis is useful. In addition, they observe streaklines indicating exchange lobes in a laboratory tank.

In sections VI and VII I present evidence that exchange lobes arise in the unsteady hyperbolic laboratory flows. By dyeing fluid near the unstable manifold of a homoclinic hyperbolic point, I am able to show the shape and movement of the exchange lobes. The fluid in each lobe is mapped into the next lobe of the same type at exactly T_f , the forcing period of unsteadiness in the tank. The hyperbolic geometry in the laboratory tank is very similar to that shown in Figure D1 c & e.

(Figure D1 caption: a: Stagnation points: hyperbolic (left) and elliptic (right). b: ‘Heteroclinic’ hyperbolic points in a steady jet-recirculation geometry. Note the elliptic (M, N) and hyperbolic (A, B, C) stagnation points and the manifolds. The bold line is a portion of *both* the unstable manifold of point A and the stable manifold of point B. c: A ‘homoclinic’ hyperbolic point in a steady figure-eight configuration. The bold line is a portion of *both* the unstable and stable manifolds of hyperbolic point A. d: Contorted manifolds in an *unsteady* heteroclinic configuration. Lobes arise between the stable (bold) and unstable (fine) manifolds. Progressively darker shading marks the position of the same dyed patch of fluid at times $t = t_o + nT_f$ where T_f is the forcing period. e) same as in panel d) but for homoclinic hyperbolic point.)

Figure D1



V. Lab apparatus & procedure:

I explore two generic recirculation geometries in a rotating tank experiment. In one case a single recirculation sits between a boundary current and the interior. In the other case there are two recirculations, which meet at a hyperbolic point. (see Figure I1a & b) I produce these recirculations in a ‘sliced cylinder’ rotating tank similar to the original model introduced by Pedlosky & Greenspan (1967). A schematic of the apparatus is shown in figure Lab1. In this section I will briefly discuss the sliced-cylinder apparatus and the general flow regimes in the tank. I will then outline the particular procedures I employed in my data collection.

Sliced-Cylinder Apparatus:

The tank is placed on a rotating table that is spun counterclockwise at $\Omega=2$ (rad/s). The tank is 42.5 cm in diameter and is fitted with a sloping bottom and a submerged ‘lid’ that is differentially rotated (at a rate $\Delta\Omega$) in order to create a ‘surface’ stress on the homogeneous fluid. The resulting flow is a single layer on a topographic beta plane forced by uniform upwelling or downwelling (due to the surface stress of the lid). The mean fluid depth is $H=20$ cm with a total change in depth $\Delta H=6$ cm. The resulting bottom slope $s=0.15$, combined with the standard rotation rate for these experiments produces a topographic beta, $\beta = fs/H = 3(ms)^{-1}$. For the remainder of this work I adopt northern hemisphere terminology in referring to the shallow (poleward) end of the tank as ‘north’, and the deeper end as ‘south’. In addition, in discussing the velocity field below I utilize and coordinate system with $+x$ to the east and $+y$ to the north. I generally ignore any motion in the $+/-z$ direction, as the flow is assumed to be horizontal except in the frictional boundary layers.

The transparent, rotating lid fits within the circumference of the tank, supported by a ring that sits on the top edge of the tank (the top view of the tank is left open for imaging). I control the rate of rotation of the lid through a computer interface system and a stepping motor. (Please see Appendix A for the details on this motor control system). In these experiments the lid is always rotated in the clockwise (anticyclonic) direction. This results in a surface stress producing uniform Ekman downwelling over a layer thickness:

$$\delta_{EK} = \sqrt{\frac{\nu}{\Omega}} \quad w_{EK} = \Delta\Omega \cdot \delta_{EK}$$

where $\nu = .01$ (cm^2 / s^{-1}) is the kinematic viscosity of water, the working fluid, and the lid rotation range from $.0076 < \Delta\Omega < .2777$ (rad/s), (with the majority of experiments performed in the range: $.0173 < \Delta\Omega < .048$ (rad/s)). Further details on these and other dimensional and non-dimensional values for the tank are given in Table Lab1.

With the topographic beta and surface stress, a number of different flow regimes are conceivable. In all of these experiments the bottom slope is held constant and the lid rotation rate is variable. At low to moderate lid rotation rates, the interior the flow is close to the Sverdrup solution as the change in potential vorticity due to the Ekman downwelling is balanced by vortex columns stretching as they move ‘south’ across the sloped bottom. This balance is confirmed by the small value of $U_s / \beta L^2 = O(2 \times 10^{-4})$.

A return flow must balance this southward flow in the interior, and this occurs in a narrow boundary current along the western wall of the tank. On the scale of the boundary current, the surface forcing is unimportant and the structure of current depends on the primary physical factor balancing the change in topographic beta: inertia, bottom friction, or lateral friction. In this case the effects of lateral friction (which would give a Munk boundary layer solution) and bottom friction (likewise a Stommel boundary layer) are comparable, but δ_M (at 0.7 cm) is larger than δ_s (at 0.5 cm). Therefore the Munk solution best describes the flow in the tank at low inertial values. At higher inertial values (i.e. with stronger lid forcing) the primary balance is between the topographic beta and inertia so the western boundary becomes more jet-like. Here the boundary layer thickness’ are defined as (Pedlosky, 1987):

$$\delta_M = \left(\frac{\nu}{\beta} \right)^{1/3} \quad \delta_s = \frac{r_{ek}}{\beta} \quad \delta_l = \left(\frac{U_s}{\beta} \right)^{1/2}$$

where $r_{ek} = \delta_{EK} f / D$ is the inverse of the spin-down time determined by the Ekman bottom layer and is equal to .0014 (1/s) in this tank. U_s is the interior Sverdrup velocity. Again, please see Table Lab1 with the dimensional values for this tank. Many previous investigators have explored aspects of similar experimental flows. Since my goal in this investigation is to compare two specific flow configurations, I refer readers to previous work for detailed description of the flow regimes in a sliced-cylinder tank. (Pedlosky & Greenspan (1967), Beardsley (1969, 1975(II)), Beardsley and Robbins(1975), Pedlosky,

etal. (1997) and Griffiths & Kiss (1999)). Griffiths and Kiss (1999) present an excellent account of the mechanical and technical details in this type of set-up.

As the lid forcing is increased the flow speeds up and the inertial terms in the equations of motion become more important than the frictional terms. In our present notation, this means that $\delta_l \geq \delta_M$. The highly inertial boundary current shoots up the western edge of the tank, separates from the wall, and forms a wave-like pattern across the northern section of the tank. (see Figure U1 c-f which is described in the next section) At $\delta_l/\delta_M = 1.10$ a set of closed streamlines arises in the tank south of the first large meander in the inertial jet. This ‘inertial’ recirculation forms north of the ‘Munk’ recirculation.

For a small window of lid forcing, ($1.10 < \delta_l/\delta_M < 1.40$) both of these recirculations: the ‘inertial’ and the ‘Munk’ exist simultaneously (see Figure U1). In cases with uniform lid forcing (i.e. the closest we get to steady flow) a unique hyperbolic point exists between these two recirculations, and it is exactly this feature of the flow I investigate. The balance between the Munk and inertial boundary layer thickness’ determines whether the single or double recirculation configuration exists, so I use the value $\delta = \delta_l/\delta_M$ to describe the forcing. This parameter is easily computed as, with the above parameter settings we find, $\delta = \delta_l/\delta_M = 8.1(\Delta\Omega/\Omega)^{1/2}$

In order to investigate the flow in the region of a hyperbolic point in an unsteady case, I sometimes force the lid in an unsteady fashion (so that the lid rotation rate oscillates slightly around an average value). The lid rotation rate is then:

$$\Delta\Omega_{unsteady} = \Delta\Omega(1 + A_{osc} \sin(2\pi t / T_{osc}))$$

where $\Delta\Omega$ is the average or ‘background’ lid rotation rate, A_{osc} is the amplitude of oscillation, and T_{osc} is the period of the oscillation. Most of the unsteady runs are at $A_{osc} = 0.05$, although a few are at values up to $A_{osc} = 0.15$. The period of oscillation is always set equal to the time it takes the lid to complete one full rotation because there is some slight unsteadiness at that period due to imperfections in the glass lid. Therefore $T_{osc} = T_{rot}$ and is usually on the order of a few minutes.

Data Collection Procedure:

The Pulnix camera is attached to a frame rotating with the table so that images are stationary with respect to the tank. In the resulting images we are looking down on the tank and only the lid and particles and/or dye appear to be moving. I used neutrally buoyant particles in the tank for two purposes : first I created ‘trajectory’ diagram which give a

general qualitative image of the flow and then I calculated the velocity field in order to quantify the time dependence in the tank. I also injected neutrally buoyant dye into the flow. Images of the dye were used for qualitative description of the flow and in calculating the effective diffusivity.

I encountered some amount of trouble with lighting the images well, both getting enough desired light and blocking out background light. Ideally, all light comes from sources rotating with the tank, so that no outside light biases the images as the tank spins.

For the particles runs I wanted to see only the laser light in the final images. I used a 6W Argon ion laser to supply light for the particles runs. The laser itself was water-cooled and sat away from the rotating table. A fiber-optic cable carried the laser beam onto the table via a coupling. Once on the table a specialized lens generated a horizontal sheet of light which shone through tank about 5 cm below the lid.

For the dye runs, I found the images were cleanest when the tank was lit from below. I therefore positioned two 20W fluorescent light bulbs facing upward below the tank. For all experiments I utilized black-out cloths suspended from the ceiling and pinned around the tank to cut down as much as possible on background light. Unwanted light did not pose a significant problem for the dye runs. Some unsteadiness in the lighting (due to both the laser and background light) may have affected the velocity calculations from the particles runs. (I return to this point in describing the velocity data in section VI).

In order to match the density of the particles to the density of the liquid in the tank I used Pliolite plastic particles $\rho = 1.024 \text{ (kg/m}^3\text{)}$ and salt water from a seawater intake $\rho \cong 1.022 \text{ (kg/m}^3\text{)}$ filtered at $50\mu\text{m}$. These particles are hand ground with a mortar and pestle and then sorted into size classes using a series of sieves. I chose particles of (diameter) $d \geq 250\mu\text{m}$ for the runs leading to trajectory diagrams and particles of (diameter) $150\mu\text{m} \leq d \leq 250\mu\text{m}$ for the runs used for PIV analysis.

For the particle runs the lab routine was as follows. First I pumped the seawater into the tank. I then prepared whichever particles were necessary and added them to the tank water. The number of particles in the flow varied between runs, the ‘trajectory’ diagrams looked better with a fairly low density while the PIV routine clearly worked better with a very high particle density. The next step was to arrange the laser lighting, camera focus, and black-out cloths (as noted above). The VCR or Mv-1000 digital imaging software was set to record images from the camera. Just before spinning up the tank, the lid rotation was started.

I allowed 12 minutes spin-up time for all of my experimental runs. This time was based on empirical evidence gathered from the general nature of the ‘trajectory’ diagrams of the flow. Unsteadiness in the flow associated with the spin-up process were not seen after about 7 or 8 minutes (the time for the fastest topographic Rossby wave to cross the tank is 32 seconds and the calculated spin-up time associated with the Ekman bottom layer ($1/r_{ek}$) is 70 seconds); twelve minutes allowed a generous margin of error. Once spin-up was completed I recorded images.

The trajectory diagrams were created by adding together a series of snapshots taken over some period of time (this process is described below in section VI). In order to calculate the velocity field I utilized a method known particle image velocimetry (PIV). This process finds the velocity field implied by the difference in particle locations between two snapshots taken in close succession (again, see section VI).

In addition to observing the motion of neutrally buoyant particles, I also injected neutrally buoyant dye into the flow. The dye for these experiments is McCormick red food coloring $\rho = 1.02391(kg/m^3)$. In order to create a neutrally buoyant dye [relative to pond water in tank $\rho \cong 1.022(kg/m^3)$], I mixed this dye with pond water and fresh water, in the approximate ratio: dye:pond:fresh = 50:40:10. This mixture sat in a reservoir (on the rotating table) and was pumped through tygon tubing and into the feed needle by a variable flow, peristaltic pump. I found the pump worked best if I primed the entire injection system before filling the tank. This Variable Flow Mini Pump fed the dye flow through a section of tubing: 1/50” I.D. at a rotor rpm ~ 0.5 . This results in a calculated flow rate of approximately $6 \times 10^{-3}(cm^3/s)$, which would result in a total input of $8 cm^3$ over the course of each run.

The dye was injected for twenty-three minutes in each case used for effective diffusivity calculations. This time was equal to a single ‘winding’ time for the slowest case ($r=2.5\text{ cm } \delta = \delta_l / \delta_M=1.00$) so that the dye line formed a closed circuit before being shut off (For more details on effective diffusivity see section VIII). To show the development of exchange lobes in the tank I simply captured images while the dye was still being injected. (for details see section VII). In terms of specific procedure, I simply followed the routine outlined above, skipping the addition of particles, using bottom lighting rather than the laser, and beginning the dye injection after 12 minutes of spin-up.

Table Lab1: Constant Dimensional and Non-Dimensional values for sliced-cylinder lab tank:

$L = 40 \text{ cm}$	$\beta = 3 \text{ (ms)}^{-1}$	$\beta = fs / H$
$D = 20 \text{ cm}$	$\beta^* = 0.3$	$\beta^* = \beta L / f$
$s = 0.15$	$\delta_M = 0.7 \text{ cm}$	$\delta_M = (v / \beta)^{1/3}$
$\Omega = 2 \text{ rad/s}$	$\delta_S = 0.5 \text{ cm}$	$\delta_S = r_{ek} / \beta = \delta_{EK} f / \beta D$
$f = 2\Omega = 4 \text{ rad/s}$	$\delta_{EK} = 0.07 \text{ cm}$	$\delta_{EK} = (v / \Omega)^{1/2}$
$v = .01 \text{ cm}^2 / \text{s}$	$E^{1/2} = .0035 \text{ (nd)}$	$E^{1/2} = \delta_{EK} / D$

Table: Lab2 Variable Dimensional and Non-Dimensional values for sliced-cylinder lab tank:

$\Delta\Omega \text{ (1/s)}$.0076	.0173	.0480	.2777
$\varepsilon = \frac{\Delta\Omega}{\Omega} \text{ (nd)}$.0038	.0087	.0240	.0139
$\delta = \frac{\delta_l}{\delta_M} = 8.1 \sqrt{\frac{\Delta\Omega}{\Omega}} \text{ (nd)}$	0.50	0.75	1.25	3.00
$w_{EK} = \Delta\Omega \cdot \delta_{EK} \text{ (cm/s)}$.00053	.00120	.00336	.0194
$U_S = w_{EK} / s \text{ (cm/s)}$.0035	.008	.022	N/A
$U_{whc} = U_S \cdot L / \delta_{whc} \text{ (cm/s)}$.047	.107	.293	N/A
$U_S / \beta L^2$	7.3×10^{-5}	1.7×10^{-4}	4.6×10^{-4}	N/A
$Re = UL / v \text{ (nd)}$	14	32	88	516
$Ro = U_S / fL \text{ (nd)}$	2.2×10^{-5}	5.0×10^{-5}	1.4×10^{-4}	N/A
$Ro = \Delta\Omega / 2\Omega \text{ (nd)}$.0019	.0044	.012	.070
$\frac{\varepsilon}{E^{1/2}} \text{ (nd)}$	1.08	2.47	6.86	39.71

Figure Lab1

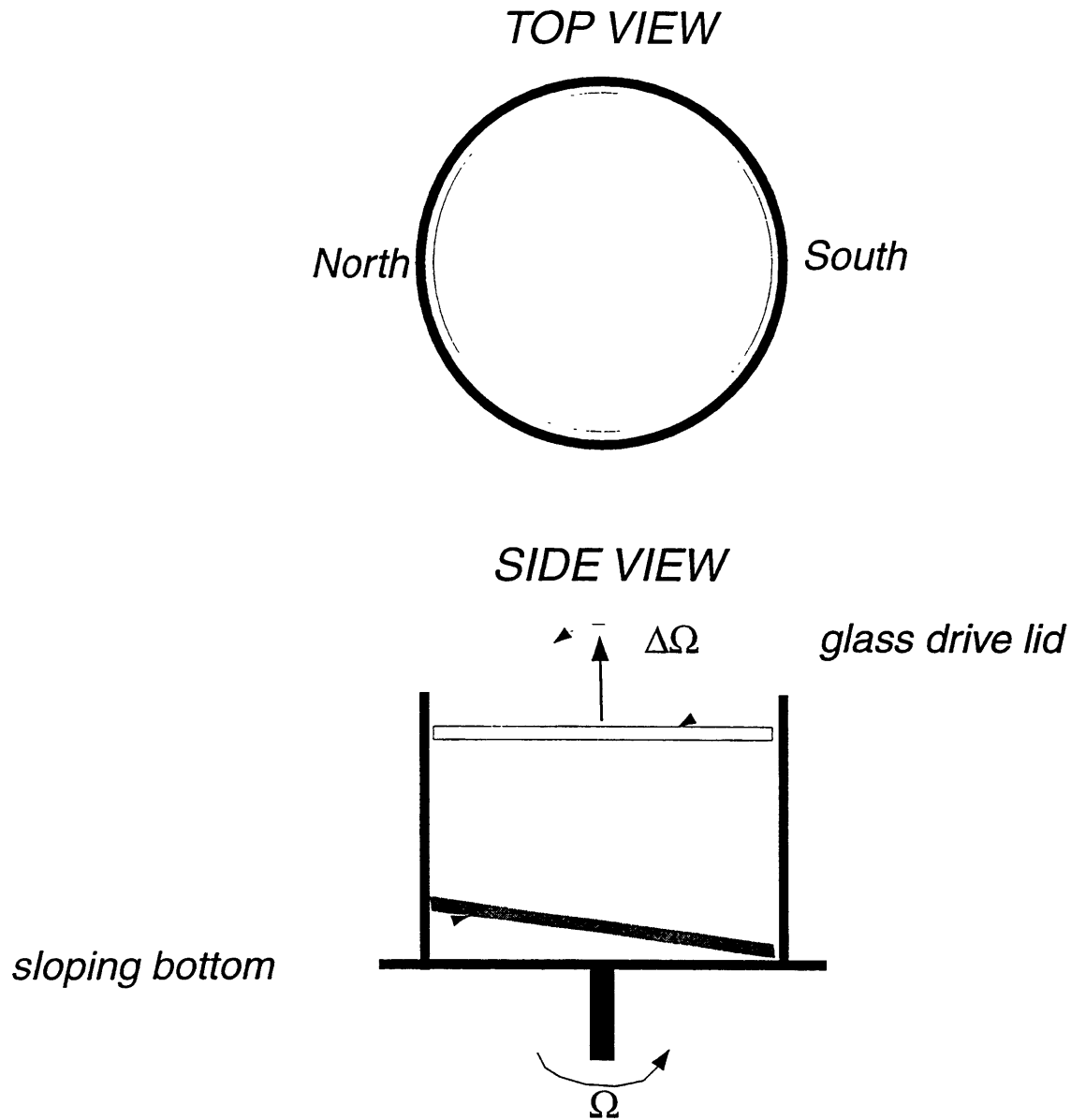


Figure Lab1: Schematic of 'sliced-cylinder' rotating tank apparatus. The entire tank system rotates at $\Omega=2$ rad/s, while a differentially rotating glass lid spins at $\Delta\Omega$, exerting a (variable) surface stress on the fluid. The false bottom is sloped to invoke a topographic beta effect. The resulting flow mimics a subtropical ocean basin with the shallow end of the tank analogous to the poleward or 'North' direction and the deep end representing the equatorward or 'South' direction.

VI. Velocity Calculations and Trajectory Images:

Trajectory diagrams of particles:

In addition to calculating $\vec{u}(x, y)$ fields from the images of particles in the tank, I created trajectory diagrams by adding together a number of images taken over some period of time. These trajectory diagrams are essentially time exposures of the particle locations and give a very nice qualitative picture of the flow field. Figure U1 contains a series of these diagrams throughout a range of $\delta = \frac{\delta_i}{\delta_M}$. They depict the transition from the single Munk recirculation ($\delta \leq 1.10$) to a double recirculation geometry ($1.10 \leq \delta \leq 1.40$) to a single inertial recirculation ($1.40 \leq \delta$). In these cases the lid rotation is steady so that $A_{osc} = 0$, $T_{osc} = \text{N/A}$. Note that the values of δ for these transitions are approximations based on the runs I performed; the only transition I mapped carefully was from a single Munk recirculation to a double recirculation, which occurs at $\delta = 1.10$ in the steady case.

At low values of δ (figure U1 a) the flow looks much like the analytical Munk solution with a broad, slow, southward interior flow and a thin, fast, northward boundary current on the ‘western’ side of the tank. The images do not extend across the full western boundary current in this figure due to the arrangement of the laser light sheet. (As mentioned above, I use the directional terms ‘north’ and ‘south’ to designate the shallow and deep ends of the tank, respectively and adopt a coordinate system with +x to the east and +y to the north.) As I increase the rate of lid forcing to $\delta = 1.00$ the inertial nature of the boundary current becomes more prominent, and the recirculation between the boundary current and the return flow becomes increasingly asymmetric across the west-east axis (Figure U1 b). Figure U1 c, d show the transition from a single Munk recirculation to a double ‘figure-8’ configuration: a Munk recirculation to the south and an inertial recirculation further north. Panel d, which depicts the flow at $\delta = 1.25$ clearly shows the hyperbolic point between the two recirculations. A single particle sits at or very near the hyperbolic point for the entire time ($t = 120\text{s}$) (this is marked by the white arrow in the figure). In the next few panels, as the lid forcing increases further, the inertial gyre grows in size and eventually shoulders out the Munk recirculation. If the lid forcing is increased

ever higher the inertial gyre continues to grow; at $\delta=3.00$ the inertial gyre fills the entire northwestern quadrant of the tank.

Figure U2 shows a trajectory diagram for a case with unsteady lid forcing ($\delta=1.25$, $A_{osc}=0.05$, $T_{osc}=131s$). This image has a somewhat different appearance from those in Figure U1, because of the much higher number of particles in the tank and the laser light over the entire western boundary current. Regardless, we can see that the area between the two recirculations is not as clean in this unsteady case as it is in the steady case depicted in Figure U1d. In the steady case a single hyperbolic point exists where the bounding trajectories of each recirculation intersect. With unsteady forcing this hyperbolic point moves around with time, so that in this time-exposure image the particle tracks display complex behavior. This is central to the lobe dynamics described above, and the images of the lobes in the tank highlight this point. (presented in section VII below)

In order to describe the flow in the laboratory tank in a more quantitative manner, I employed a method known as particle image velocimetry (PIV) for calculating the velocity field by diagnosing the movement of the particles.

PIV METHOD:

Particle Image Velocimetry (PIV) is a method of calculating a snapshot of the 2D velocity field $\vec{u}(x, y)$ in an experimental flow. Simply put, PIV involves seeding a flow with many particles, taking two successive pictures of the flow, and estimating how the particles have moved between the snapshots. I will present the basic theory and method of PIV, for a more detailed review see a text on the subject (e.g. Raffel, et al. 1998). First, the laboratory flow is seeded with neutrally buoyant particles small enough to follow the flow. Next, the lighting and imaging is arranged. Ideally, only the 2D plane of interest is lit. There are new methods under development for using PIV to calculate a 3D $\vec{u}(x, y, z)$ field, but the standard method, which I employ here, assumes most of the motion is in the 2D plane of interest (as it should be in this rotating experiment). In this experiment I use a laser sheet to light a thin horizontal slice of the tank (see lab setup in section V). The flow is then photographed at $t = t_0$ and $t = t_0 + \Delta t$ and the photos are imported into digital image files.

The velocity field can then be calculated by finding the difference in the locations of the particles between the two images $\Delta\vec{x}(x, y)$; $\vec{u}(x, y)$ is approximated by $\Delta\vec{x}(x, y)/\Delta t$.

The displacement field, $\Delta\bar{x}(x,y)$, is found by dividing each image into subregions or ‘windows’ and comparing corresponding windows in the two images. More specifically, the statistical correlation is calculated between each set of windows. This can be done either by actual spatial correlation calculations (which take a long time) or by calculating the correlation via a transform to the frequency domain (which is a little less precise, but much faster). The latter method rests on the fact that correlation in the spatial domain is equivalent to multiplication in the frequency domain.

In the spatial domain one would calculate the correlation between the two windows directly:

$$R(x,y) = \sum_{i=-M/2}^{M/2} \sum_{j=-N/2}^{N/2} \text{Im}_1(i,j) \text{Im}_2(i+x,j+y)$$

Here R is a function containing the strength of the correlation between the two image windows at each displacement (x,y). Each window Im_n is M x N pixels. The maximum peak in R(x,y) will give the displacement $\Delta\bar{x}(x,y)$.

I have chosen to calculate the correlation via a transform to the frequency domain. Once I have my two digital images, I calculate the spatial correlation as follows:

- 1) Start with matching windows:
 - $f(x,y) ==$ pixel values in image 1 window
 - $g(x,y) ==$ pixel values in image 2 window
- 2) Check to see that both regions have some particles.
- 3) Perform FFTs and multiply results (taking complex conjugate of second FFT):
 - $F == \text{FFT}(f)$
 - $G == (\text{FFT}(g))^*$
 - $H == F \times G$
- 4) Find correlation matrix by inverse transform:
 - $h == \text{FFT}^{-1}(H)$
- 5) Find the location of the maximum correlation to sub-pixel accuracy via Gaussian fitting in x and y:
 - $\Delta\bar{x}_1 ==$ peak location(h)
- 6) Stop and set $\Delta\bar{x} == \Delta\bar{x}_1$... or do a second pass.
- 7) The second pass (which I use in all of the results presented here) involves using the displacement found during the first pass to improve the choice of windows. I again use $f(x,y)$ from the first image, but this time choose a window from image 2 that is offset from x,y by $\Delta\bar{x}_1$. This improves the likelihood that all of the particles in the image 1 window

show up in the image 2 window, as explained below. Once this new $g(x, y + \Delta \bar{x}_1)$ is chosen steps 2-6 are repeated.

The above procedure is carried out for all the windows in the image. The number of windows is determined by the specified window size. In addition to choosing the window size, I can specify an overlap for successive windows. There are many criteria that go into choosing the window size and percentage overlap, some of which I discuss further below. For these results the window size is 36x36 pixels and the overlap is 25%. The PIV calculations were carried out in Matlab using a code provided to me by Karl Helfrich.

The challenge in designing a good PIV procedure is in balancing the advantages and disadvantages of various lab set-up and analysis choices (for more details on these choices see Willert & Gharib, 1991, and Adrian, 1991). In the lab the size, shape, and number of particles, lighting, camera settings, and Δt between images can all be altered. In the analysis the window size and overlap can be altered and various masking and filtering techniques can be employed. In any lab experiment there are technical restrictions, but the basic constraint is the character of the actual flow field. In this case the flow field is extremely slow. The velocity in the interior of the tank is $O(0.01)$ cm/s and the velocity in the boundary current is $O(0.1)$ cm/s. This slow flow made the choice of Δt tricky.

Although the PIV analysis should be good to sub-pixel accuracy, the results are more robust if $\Delta \bar{x} \geq 1$ pixel, so I wanted to choose a long enough time between snapshots. Yet, the choice of Δt has implications beyond displacement; this is where we begin to see the interplay between all of the alternatives mentioned above. The longer the time is between images, the lower the chances of a one to one correspondence between particles in the two images. This is due not only to particles leaving the sheet of laser light due to velocity perpendicular to the plane, but also to particles spinning such that they are reflecting light differently. In addition to these factors, computational time and memory space for storing the digital images became considerations in calculating the long time series of velocity (for very small Δt , you need many more images to cover a specified time). After performing a variety of tests I settled on Δt of 1 second.¹

¹ The Pulnix digital camera captures at a much more rapid rate of 30 frames per second. Testing demonstrated that frames this close together not only have a very small (subpixel) $\Delta \bar{x}$, but also produce extremely noisy results. At $\Delta t = 1/30$ s the resultant $\vec{u}(x, y)$ have many inconsistent vectors and fields

Another important consideration was the size of the particles. Ideally, the particles should be small enough to follow the flow well, yet large enough to show up clearly in the digital image. I chose to use particles that fell in the size range $180\mu m \leq d \leq 250\mu m$. I also wanted a high particle density, as investigations into the accuracy of PIV techniques have correlated high particle density with better results. I did not attempt to quantify the number of particles in the flow or the percentage of the image filled with particles, I found that I could estimate the number of particles I needed simply by watching the appearance of the flow.

Having decided the particle size and time between images, I then tested different sizes for the interrogation windows. The choice of window size, like the choice of Δt involves balancing a variety of effects. The method of PIV rests on the assumption that strain and rotation are small compared to translation on the scale of your window. This means we want a small window. However, we need a window size that is much larger than the displacement so that few particles leave or enter during the time between the two snapshots. In addition, the 'Nyquist criteria' implies we should choose $\ell/2 > \Delta \bar{x}$ where ℓ is the length of a window edge. This is a result of the transformation to the frequency domain. The Fourier transform involves an infinite integral, so in the course of the FFT the window is assumed to be periodic (this means any larger displacement will be aliased to misleading frequencies). Computational time is again a consideration in choosing window size; the smaller the windows, the more there are, and the longer the computation time. I settled for a window size of 36 pixels with an overlap of 25%. This resulted in a \bar{u} vector for each 27×27 pixel area, but these are not all independent calculations.

PIV Data presentation:

Having assembled a working procedure for PIV analysis I was able to calculate velocity fields for some of the flows. My main objective in calculating the velocity in the tank was to diagnose the time dependence in the flow. This required compiling a time series of many thousands of velocity fields, so for this analysis I chose to sample the velocity in a small subregion of the flow. I chose the eastern part of the inertial recirculation because I expected fairly high velocity and strong time dependence in this

calculated at successive times look very different. After testing a series of values I settled on $\Delta t = 1s$. This was the shortest value for which $\Delta \bar{x}$ in the region of interest was on the order of 1-2 pixels.

region. These $U(t)$ results are presented below, but first I introduce a few snapshots of $\bar{u}(x, y)$ over the entire western half of the tank.

Figure U3 shows the basic flow field for two cases. The panels a & b correspond to $\delta=1.25$, $A_{osc}=0.05$, $T_{osc}=131$ s, while panels c & d correspond to $\delta=1.00$, $A_{osc}=0.05$, $T_{osc}=204$ s (the upper panels show a case with double recirculation, the lower panels with single recirculation, these correspond to figure U1 panels d and b, respectively). North is at the top of each quiver plot. To the right of each quiver diagram is a plot showing the y -component of the velocity, $v(x, y)$, at three different cross-sections of the flow. Note that the western boundary current itself is not well resolved in the quiver plots, but does show as a maximum in the $v(x, y)$ plots. This is in part due to the choice of window size and Δt , but is not really a concern since we focus on a different region for our time series. The PIV analysis produces sensible results, with a boundary current ($v>0$) near the wall and a return flow ($v<0$) in the interior at each cross-section. As we would expect the speeds are higher in the $\delta=1.25$ case. The magnitudes of these velocities are low, and in fact come from areas of the flow where $\Delta \bar{x} < 1$ pixel so the uncertainty on the $\bar{u}(x, y)$ is fairly high. Nevertheless, the velocity calculation method manages to capture the broad characteristics of the flow, even in very slow regions.

I now present a time series of the velocity in order to demonstrate that the unsteady lid forcing produces a similar unsteadiness in the flow, where: $U(t) = \sqrt{u^2 + v^2}$. In this case $\delta=1.25$, $A_{osc}=0.15$, $T_{osc}=131$ s. $\bar{u}(x, y, t)$ is calculated in the interior branch of the inertial recirculation. I chose this region because it is the most active area for lobe formation (see discussion of lobes in section VII below).

Figure U4 shows a quiver plot of $\bar{u}(x, y)$ over the entire region with a rectangle outlining the subregion where I calculated $U(t)$. The outer rectangle specifies the size and location of the images used as raw input into the PIV routine. The inner rectangle specifies the region over which $U(t)$ was actually calculated.² Also notice there are two sets of $\bar{u}(x, y)$ arrows on figure U4. These represent velocity fields calculated at $t = t_o$ and $t = t_o + T_{osc} / 2$. They give a qualitative indication of the unsteadiness at the lid oscillation period.

² The PIV routine is more accurate if you calculate U over some subsection of your raw image, because on the second pass the image 2 window can be translated outside of the calculation area.

The time series $U(t)$ as well as the power spectrum density of this time series are shown in Figure U5. $U(t)$ is given in cm/s over a period of 1060 seconds. One image was captured every second and $\vec{u}(x,y)$ was calculated from each pair of images. Each of these calculations resulted in $\vec{u}(x,y)$ with four vectors (see four vectors in inner rectangle in figure U4). The magnitudes of these four vectors were averaged for each $\vec{u}(x,y)$ and then compiled to give $U(t)$.

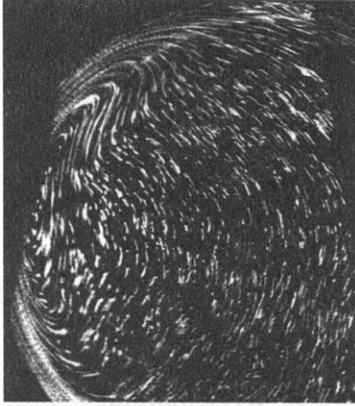
Two periods immediately catch the eye in the velocity record and PSD: $T = O(3s)$ and $T = O(100s)$. These correspond to the rotation period of the tank, $T = \pi s$, and the oscillation period of the lid, $T = 131s$. The strength of the peak at $T = 131s$ in the PSD confirms that the unsteady lid forcing results in variable speed in the tank. From Figure U4, some variable direction in the velocity is also probable.

Some, if not all, of the signal at the fastest period in $U(t)$, $T = \pi s$, is an artifact of imperfections in the rotating tank and imaging system. The cable carrying data from the camera must pass through a rotating coupling so that a signal at the period of rotation is not at all surprising. In addition to the problem with the camera signal, one can see some rapid unsteadiness in the laser light, (the whole screen flashes). The light from the laser travels to the tank through a fiber optic cable which must pass through a rotating optical coupling in order to pass onto the rotating table. It is unclear how much of the flashing in the laser images is due to this coupling and how much is due to the camera problem. There could, of course, be an actual unsteadiness in the flow at $T = \pi s$ due to some mechanical imbalance in the rotating table. In all likelihood, the signal in the PIV velocity field at this high frequency is due to a combination of these effects.

In any case, the time series and PSD clearly show unsteadiness in the flow at the period of the lid oscillation, $T_{osc} = 131$ seconds. Unlike at the much faster $T = 3.14s$ period, there is no reason to suspect mechanical or imaging errors contributing to a signal at this period. In the following section I present images of dye in the tank that indicate the exchange lobes are dominated by exactly the lid forcing frequency.

Figure U1: Time exposure trajectory images of particles in the tank illustrating general flow regimes. Panels a-f correspond to increased lid forcing ($\delta = 0.75, 1.00, 1.10, 1.24, 1.40, 1.56$), and the lid forcing is *steady* in all cases. All of these images are composites of 60 snapshots taken two seconds apart, so that the image shows the movement of the particles over 120 seconds total. Panels a & b show a single ‘Munk’ recirculation. Panel c shows the transition to (panel d) a double recirculation. Panel e shows a transition back to a single recirculation, in this case (panel f) an inertial recirculation.

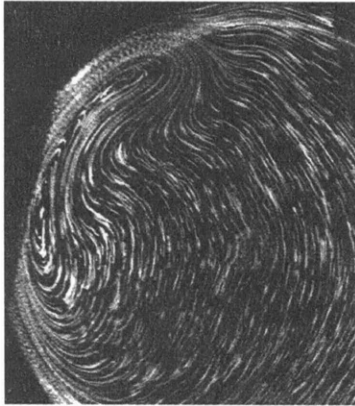
a. $\delta=0.75$



b. $\delta=1$



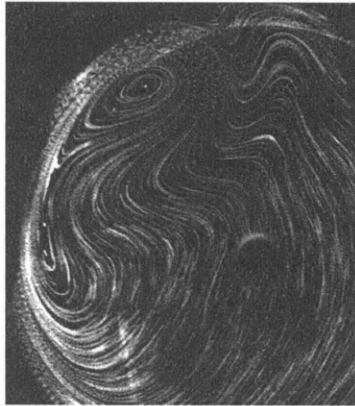
c. $\delta=1.1$



d. $\delta=1.25$



e. $\delta=1.4$



f. $\delta=1.55$

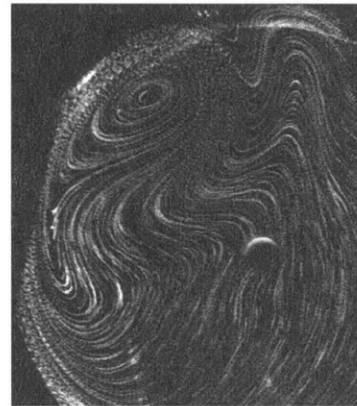


Figure U2: Time exposure trajectory diagram for *unsteady* lid forcing at $\delta=1.25$. The period of the lid oscillation is $T_{osc}=131s$ and the normalized amplitude is given by $A_{osc} = .05$. The total time shown is 180s (image is composed of 90 individual snapshots taken at $\Delta t = 2s$). Notice there is no longer a distinct hyperbolic point in this image as there is in the steady case (Figure U1d), but rather a hyperbolic area between the two recirculations.

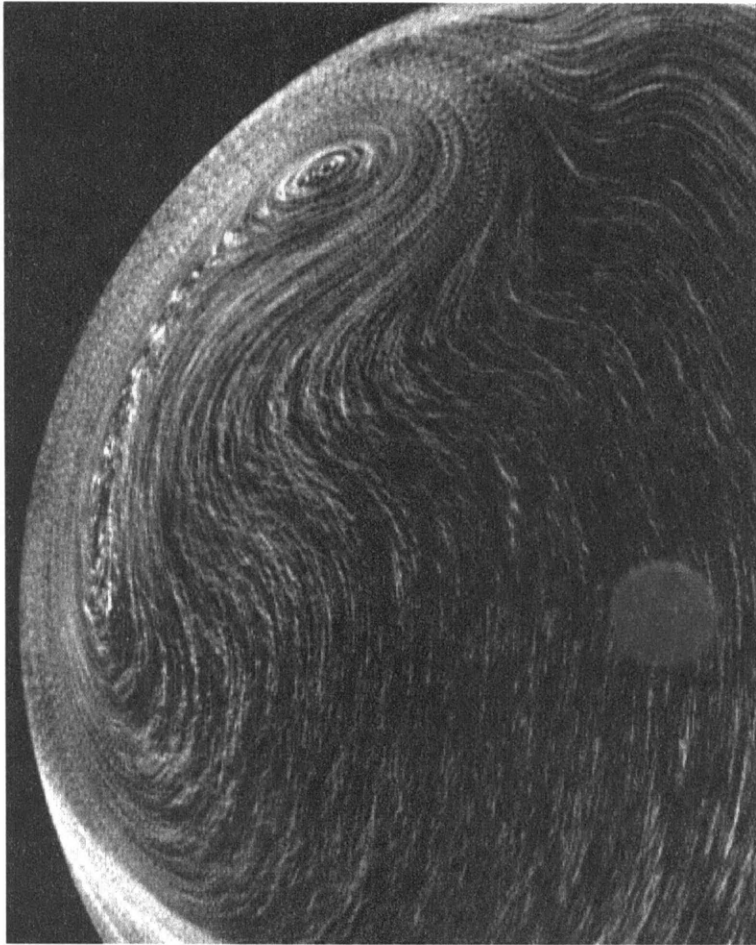


Figure U3: Quiver plots and velocity plots for two cases, panels a & b: $\delta=1.25$, $A_{osc}=0.05$, $T_{osc}=131$ s (double recirculation) and panel c & d: $\delta=1.00$, $A_{osc}=0.05$, $T_{osc}=204$ s (single recirculation). The velocities plotted here are averages over 6.2 seconds which is twice the shortest period described below ($T=3.14$ s). Six image pairs are used with $\Delta t=1.03$ s between each pair. In quiver plots (a & c) the arrow lengths are arbitrarily scaled. The velocity $v(x,y)$, the y-component of $\vec{u}(x,y)$ is shown in panels b & d as a function of distance from the western edge of the image.

Figure U3

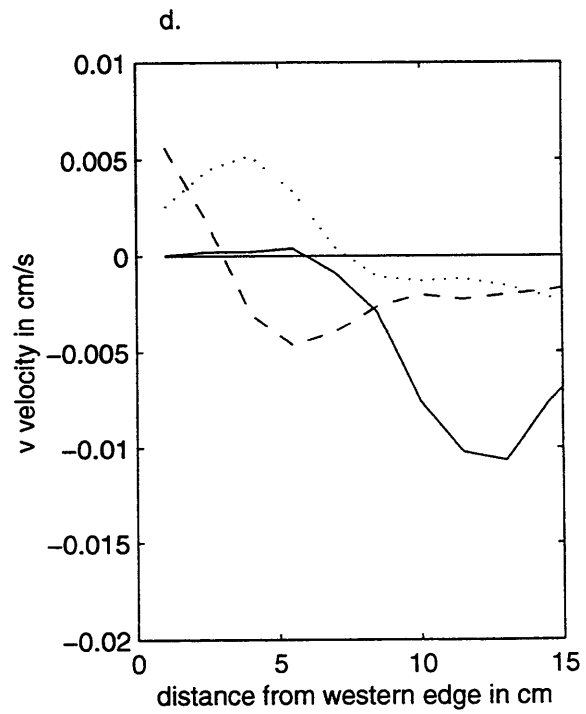
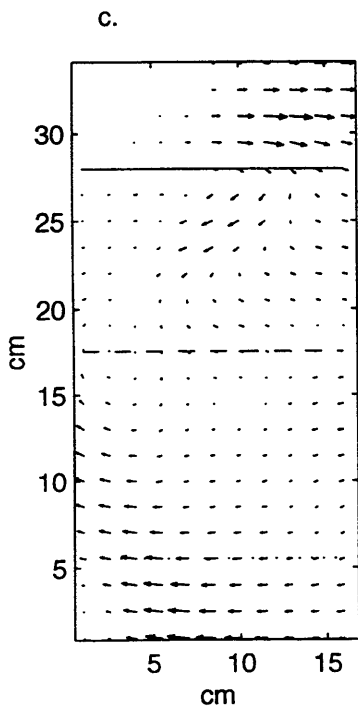
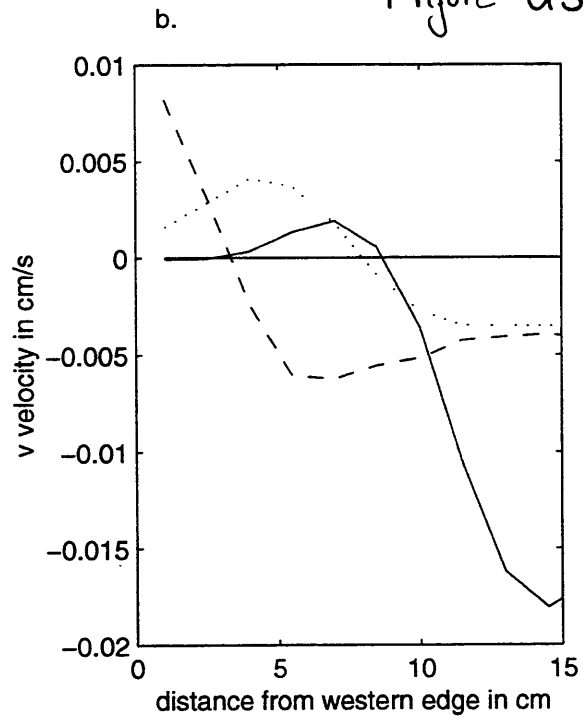
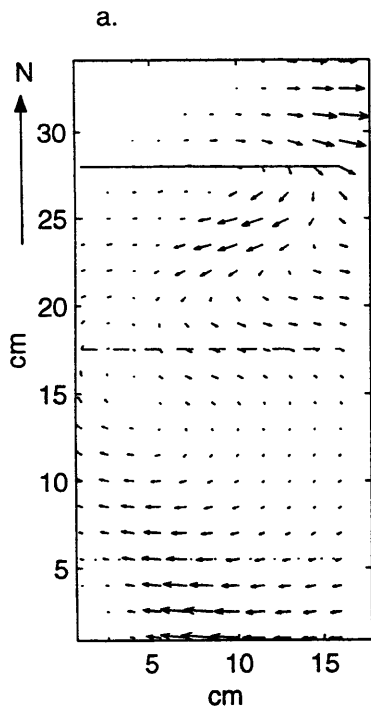


Figure U4: Quiver plot for $\delta=1.25$, $A_{osc}=0.15$, $T_{osc}=131$ s. The velocity vectors are calculated as in Figure U3. The two sets of $\vec{u}(x,y)$ arrows represent velocity fields calculated at $t = t_o$ and $t = t_o + T_{osc} / 2$. The outer rectangle corresponds to the image area captured for each $\vec{u}(x,y)$ calculation in the time series. The inner rectangle outlines the actual area over which the velocity was calculated (see footnote in text). Notice the four resultant velocity vectors within the inner rectangle, these are the vectors that are averaged into the final magnitude in the $U(t)$ time series.

Figure U4

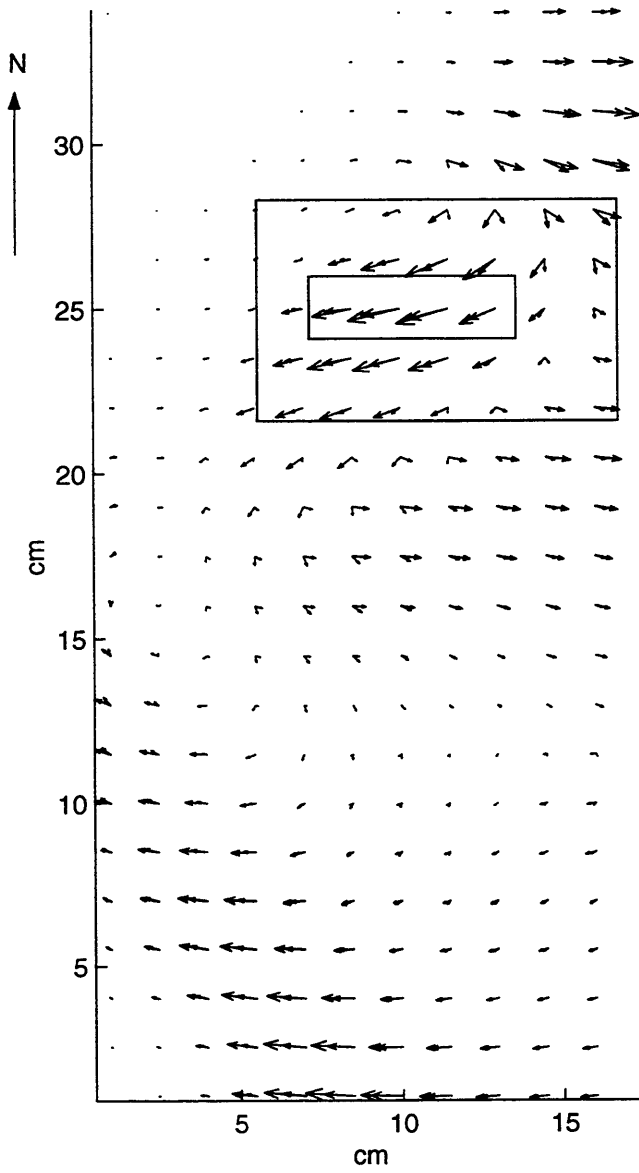


Figure U5: a: Time series $U(t)$. Velocity in cm/s over a total of 1060 seconds. The velocity was calculated using the PIV routine outlined in the text with $\Delta t=1$ s. Four $\vec{u}(x, y)$ vectors were calculated each second and averaged to this $U(t)$ (see Figure U4). b: Power Spectrum Density (PSD) in cm^2 / s shown (solid line) as a function of frequency (Hz). The PSD was calculated using Thomson's multi-taper method with 4 windows. The dashed lines represent the 95% confidence interval.

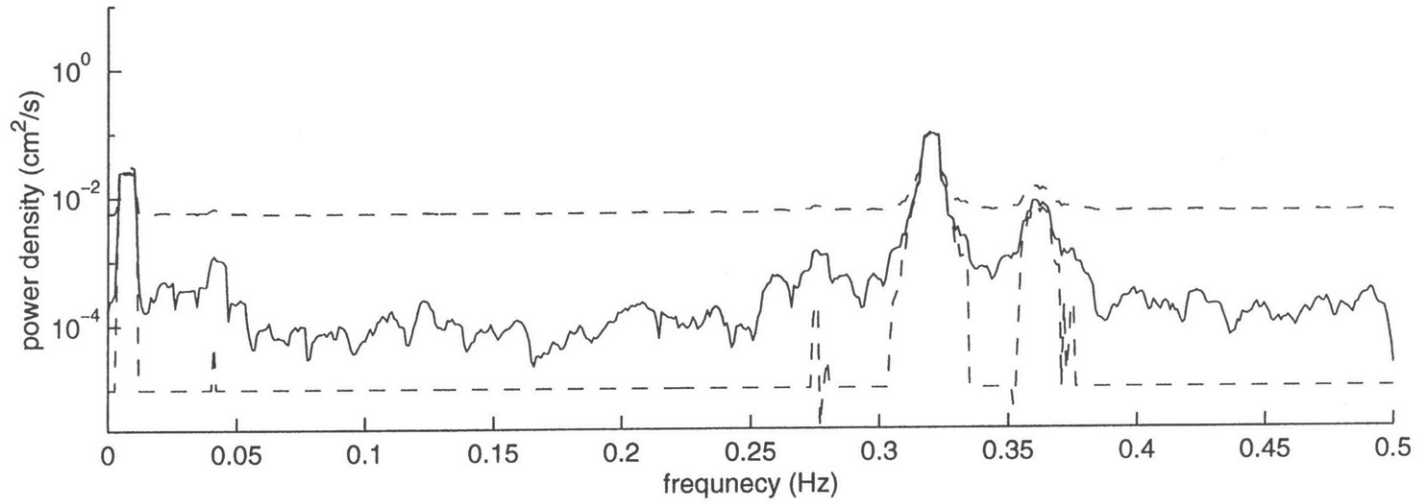
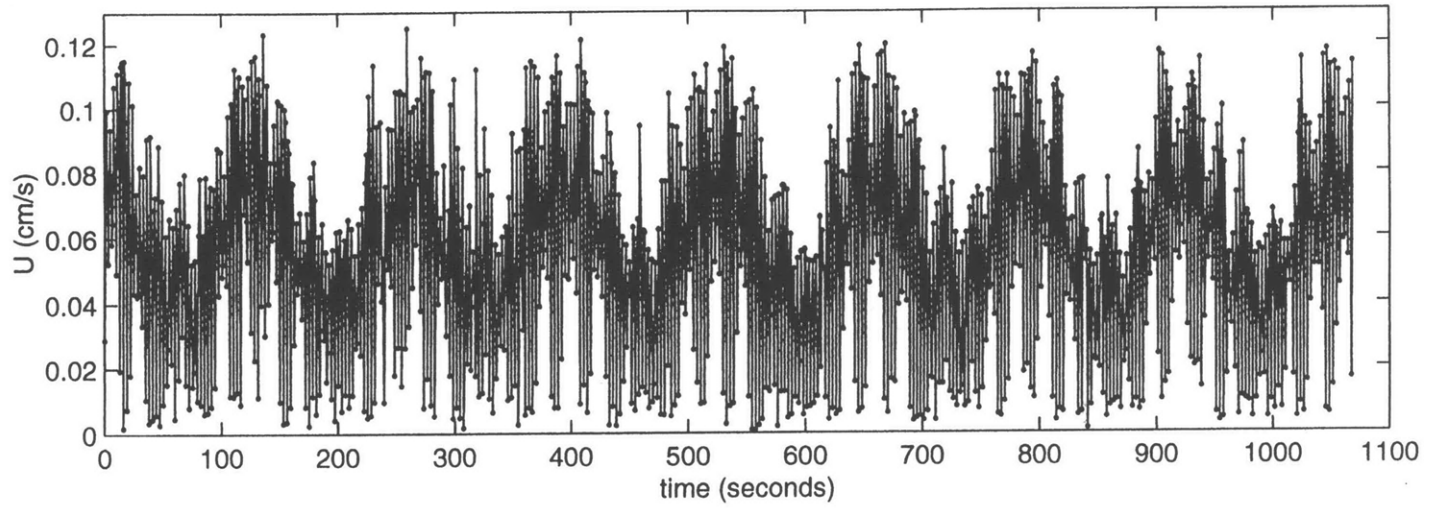


Figure U5

VII. Dye Evidence for Exchange Lobes:

In the previous section I described the structure of the velocity field in the tank, emphasizing the time dependence resulting from the unsteady lid forcing. In section IV I outlined the profound implications this unsteadiness can have on a flow field involving a hyperbolic geometry; as the stable and unstable manifolds tangle, lobes form the turnstile mechanism for chaotic advection and radically increased exchange. Here I present images of dye in the lab tank that indicate the existence of lobes in just such a geometry. This is done by injecting dye so that it traces the approximate path of the unstable manifold leaving the hyperbolic region toward the North. Unfortunately, it was not possible to trace out the shape of the stable manifold, so that we only see half of the lobe boundaries. This is because we do not know where the stable manifold comes from as it approaches the hyperbolic point. We can trace the unstable manifold because we know where it leaves the hyperbolic point. Nevertheless, the structure of the lobes is easy to see, as is the increase in lobe size as the unsteadiness or the average rotation rate is increased.

The images presented in this section are for the range of $\delta = \delta_I / \delta_M$ for which a double recirculation geometry exists with steady lid forcing. As illustrated above in figure U1, this figure-eight configuration exists in the (approximate) range $1.10 < \delta < 1.40$. Figure L1 illustrates this basic hyperbolic geometry for a case with $\delta=1.25$ and *steady* lid rotation. Because the flow is nearly steady, the dye streaklines trace out approximate streamlines (with thickening in the line due to molecular diffusion and double diffusion of the dye mixture). The dye is released continuously into the western edge of the Munk recirculation. In the upper panel we see a snapshot of the flow nine minutes after the dye injection is started (this time is arbitrarily set to $t=0$). The dye, which initially leaves the needle heading north, (or to the left in this figure), has split upon encountering the hyperbolic point; some dye has returned to the south in the Munk recirculation and some dye has continued north to loop around the inertial recirculation. At the time this photo is taken, this north-looping dye is encountering the hyperbolic point from the other direction.

The lower panel of figure L1 shows the same flow twelve minutes later (the time above this plot is in units of time normalized by the lid rotation period T_{rot}). Now we can see each recirculation surrounded by dye, with clear fluid in the center. The two recirculations have quite different appearances; this is due to a number of factors including

the higher volume of dye in the southern recirculation due to injection location and the lower velocities in the southern recirculation which allow for more diffusion, as it takes longer for a parcel to transit this slower recirculation. Another asymmetry exists between the western and eastern edges of the recirculating region; the western edge is darker due to the newly injected dye and appears smoother than the eastern edge. This is due to the high velocities in the western boundary current and much slower advection in the interior.

This image of an orderly figure-eight is radically altered when a slight unsteadiness is added to this flow. As noted above, when the flow is subject to a perturbation the hyperbolic point no longer remains stationary, and the trajectories bounding the recirculation (manifolds) begin to oscillate, fold, and intersect each other. The dye leaving the hyperbolic point to loop around the northern recirculation no longer neatly approaches the hyperbolic point again on its way south (as it does in Figure L1 panel a). This is because the dye is tracing the unstable manifold, and is separated from the stable manifold. The contortions of the unstable manifold are demonstrated in the time series in figure L2. This collection of images traces the progression of a streakline in the tank where $\delta=1.25$, $A_{osc}=.05$, and $T_{osc}=131s$. The time printed above each image is normalized by the lid oscillation period, T_{osc} , with $t=0$ set arbitrarily at eight minutes after dye injection is started. The close similarity in the appearance of the streakline at $t=0$ and $t=1.0$ confirms that the periodicity of the exchange lobes is exactly that of the lid forcing.

The separation of the stable and unstable manifolds can be inferred by comparing the dye lines from the steady and unsteady cases. In the steady case (figure L1a) the dye leaving the hyperbolic point on the unstable manifold (in the western boundary current) must also lie on the stable manifold because it clearly approaches the hyperbolic point again on the interior side of the recirculation. In the unsteady case (figure L2a) the dye is never on the stable manifold, but instead meanders back forth into the interior and into the recirculation itself. Theoretically, the unstable manifold should oscillate back and forth in this manner, approaching infinitely close to the hyperbolic point without ever reaching it.

There are a number of additional features to note in figure L2. Although I was unable to trace the exact location of the stable manifold, it is possible to glean something of the shape of the exchange lobes from the unstable manifold alone. If we consider the steady case presented in figure L1 to outline the approximate (Eulerian) average recirculation for this case, then clearly fluid is being carried into and out of the recirculation by exchange lobes. The dye that is meandering into the recirculation at $t^*=0$ (where

$t^*=t/T_{osc}$) is visible inside the recirculation at $t^*=0.6$, and similarly another lobe curling in at $t^*=1.0$ is visible inside at $t^*=1.6$. The lobes transporting fluid out of the recirculation into the interior appear at the same periodicity, with the lobe stretching south at $t^*=1.8$ occupying the same place the previous lobe sat at $t^*=0.8$. One interesting note is the thickening of the dye lines due to subsequent lobes carrying dye inside the recirculation (compare $t^*=0.6$ to $t^*=1.6$). This implies that some of the fluid imported into the recirculation during one period is exported out during a subsequent period. I explore this further below in a brief discussion of the lobe areas and implied recirculation flushing times.

The asymmetry between the two recirculations that was evident in the steady case reasserts itself here more dramatically. While there are huge contortions in the unstable manifold of the inertial recirculation, the unstable manifold of the Munk recirculation is not even clearly distinguishable. This is again due in part to a higher volume of dye and more diffusion in the Munk recirculation, but there are other important factors.

One may be that the winding time necessary for a parcel to complete a recirculation is much longer in the Munk recirculation than in the inertial recirculation. I can approximate the winding time by noting when the first dye makes it back to the location of the needle where it was injected (see figure L4 where the Munk recirculation is almost at this point). At $\delta=1.25$ at both $A_{osc}=0.05$ and 0.15 this winding time is approximately thirteen minutes, or six times the oscillation period. (Note that the winding time is the same regardless of the amplitude of unsteady forcing, this confirms the persistence of the coherent structures in this flow, even with large time-dependence). In the inertial recirculation, the other hand, the winding time (see table 1 and discussion below) is $O(1.5)$ times the oscillation period. In discussing previous work on these dynamical lobes we noted that in many cases the forcing period (Lagrangian times scale) is much longer than the winding time (Eulerian time scale) so that $T_w \ll T_{osc}$. It is interesting that we see lobes in the inertial recirculation where $T_w = O(T_{osc})$, and the lack of lobes in the Munk recirculation may be due to the fact in that region $T_w \gg T_{osc}$. On the other hand, there could be lobes forming that are either very small or packed closely together so we cannot see them in the dye streaklines.

Another time series of unstable manifold behavior is presented in figure L3. Figure L3 illustrates a case similar to L2, but with stronger unsteady forcing (where $\delta=1.25$,

$A_{osc}=0.15$, and $T_{osc}=131s$). The excursions of the unstable manifold are even more extreme, presumably resulting in larger lobes and more rapid exchange. At first glance it appears that the recirculation region itself is larger, but as I discuss below in the discussion of lobes areas, I do not believe this to be true. As in the previous figure, the periodicity of the lobes is apparently closely aligned with the forcing period and lobe exchange into and out of the recirculation is obvious. Again the winding up of the manifold inside the recirculation implies that some imported fluid will be rapidly exported.

A rough calculation of the area of the lobes was carried out for the two cases pictured in figure L2 and L3. Both of these runs have the same background lid rotation rate, but the amplitude of the oscillation around that background was higher in one case. This calculation was based on the assumption that every lobe must have equal area. This follows from two separate facts. First, each subsequent lobe replaces the previous lobe of the same type once every period. (one ‘type’ is a delivery lobe importing fluid into the recirculation, the other is a retrieval lobe exporting fluid). Second, unless the recirculation is growing or shrinking, the same amount of fluid that is imported into the recirculation must be exported. This leads to the conclusion that every lobe must have the same area if the flow is periodic.

Figure L4 contains hand-drawn approximations of lobes enclosing (approximately) equal areas. I started with the images from $t=1.0$ in Figures L2 and L3 and found lobes by drawing a line to approximate the stable manifold approaching the hyperbolic point.¹ I placed this line by trial and error, and settled for a line which resulted in approximately equal areas for the three lobes that are visible in each image. The lines and lobes for the $A_{osc}=0.05$ case are darkened on the left side of Figure L4 (likewise $A_{osc}=0.15$ is shown on the right). It is important to note that this is a rough calculation as I am guessing the location of the stable manifold and there are other choices for line location which will result in equal lobe areas.

The purpose of this exercise was to garner a rough idea of the location of the stable manifold and to approximate a flushing time for each recirculation. In order to find a flushing time, I need to know not only the lobe areas, but also the area enclosed by the ‘recirculation’. I consider the ‘recirculation’ to be the area traced by the undisturbed

¹ I did attempt the reverse of this process, choosing the ‘recirculation’ outline from the steady case and testing to see if the resulting lobes had equal areas. The lobes that resulted from this process did not have

manifolds (dye streakline) from the steady case, and this area is shown in black in Figure L5a. For comparison I show the area enclosed by the ‘recirculation’ in both of the unsteady cases from the previous figure (L5 b & c). This is the area enclosed by the unstable and stable manifolds approximated by the dye streakline and the arbitrary line chosen for the lobe calculation. Encouragingly, the areas of all three ‘recirculations’ are very close at $14 \pm 1 \text{ cm}^2$ (see table Lobes1). The lobe areas for the slightly unsteady case were small, requiring about nine lobes to equal the area of the recirculation. For the case with stronger forcing the lobes were much larger, requiring only three lobes to equal the total area. If the lobes did in fact deliver and collect fluid from the entire recirculation, these numbers would imply flushing times of $T_f = O(9 \times T_{osc})$ for $A_{osc} = 0.05$ and $T_f = O(3 \times T_{osc})$ for $A_{osc} = 0.15$. In reality the flushing is more complicated as the lobes probably do not fill the entire area inside the recirculation, as discussed below in relation to invariant KAM tori.

We can compare these flushing times with the winding time necessary for a parcel to complete a recirculation. We can approximate a winding time from the time series images. In both figure L2 and figure L3, the parcel of dyed fluid that is just beginning to form a delivery lobe at $t^* = 0.2$ has wound around inside the recirculation to nearly the same position by $t^* = 1.8$. This results in an approximate ratio of flushing time to winding time of $T_f / T_w \approx 6$ at forcing amplitude $A_{osc} = 0.05$ and $T_f / T_w \approx 2$ for $A_{osc} = 0.15$. (see Table Lobes1)

I will return to noting the actions of these lobes in discussing KAM tori in section VIII and in my conclusions (section IX). In this section I have shown: 1) lobes formed by the intersections of the manifolds are mapped onto each other at $t = T_{osc}$, 2) the winding time for the inertial gyre is $O(1.5)$ the forcing time, while in the Munk recirculation $T_w \gg T_{osc}$, 3) it is possible to approximate lobe areas and flushing times for the ‘recirculation’ in the unsteady cases, 4) flushing is much more rapid in the case with higher unsteady forcing. Having illustrated the lobe mechanism responsible for chaotic advection in these hyperbolic geometries, in the next section I diagnose the advective stirring (or lack thereof) in a variety of cases by calculating the effective diffusivity from images of the dye.

equal areas. This shows that the ‘recirculation’ has a different shape in the unsteady cases, although the shapes resulting from my calculations do have the same area as the steady recirculation.

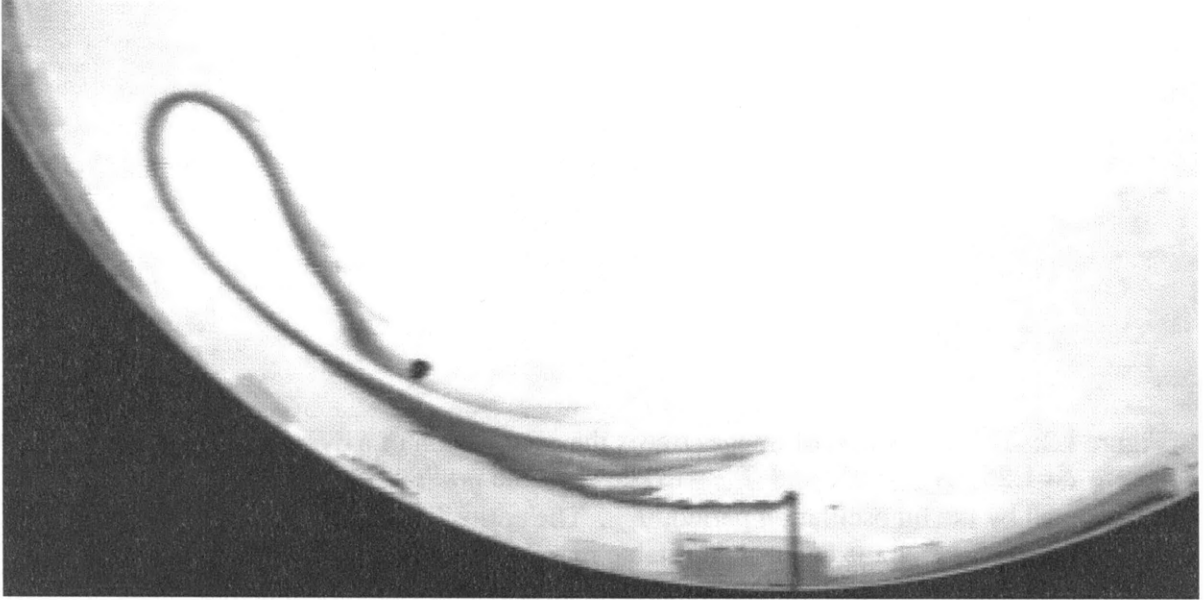
Table Lobes1:

$A_{osc} = \Delta\Omega_{lid} / \Omega_{lid}$	Recirculation Area (cm^2)	Lobe Size (cm^2)	T_f / T_w
0 (steady)	13.94	N/A	N/A
0.05	13.76	1.4-1.6	6
0.15	13.55	3.5-4.4	2

Figure L1: Dye streakline for a double recirculation (figure-eight) run, $\delta=1.25$ with *steady* lid rotation. Images are at nine minutes and twenty-one minutes after the dye injection is begun. Time above each figure is normalized by the lid rotation period T_{rot} , with $t=0$ arbitrarily chosen at nine minutes. Orientation of the figure is such that the western boundary current is running to the left along the bottom of the image. The dark line extending from the edge of the tank into the flow is the dye needle used for injection. The end of the needle extends into the Munk recirculation, while the inertial recirculation is further to the left (north).

a.

$$t / T_{osc} = 0$$



b.

$$t / T_{osc} = 5.5$$

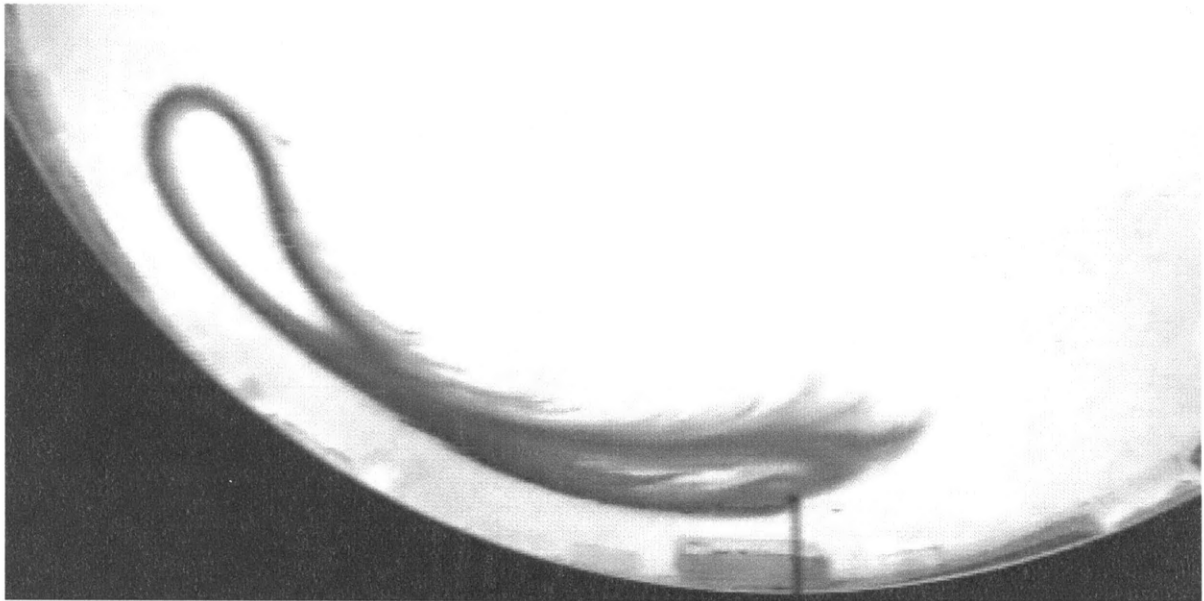
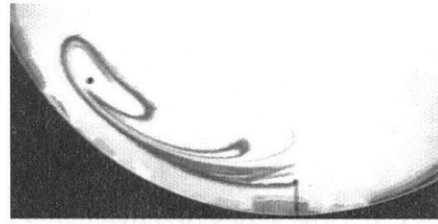


Figure L2: This collection of images traces the progression of a dye streakline in the tank where $\delta=1.25$, $A_{osc}=.05$, and $T_{osc}=131$ s. The time printed above each image is normalized by the lid oscillation period, T_{osc} . The entire figure covers two full oscillation periods, during which the contorted unstable manifold of the inertial recirculation indicates the shape of the exchange lobes.

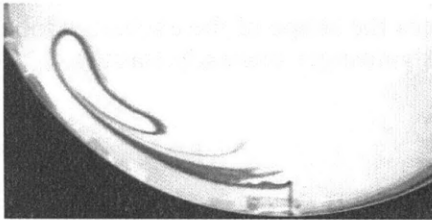
$t / T_{osc} = 0$



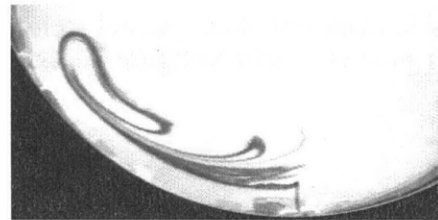
$t / T_{osc} = 1$



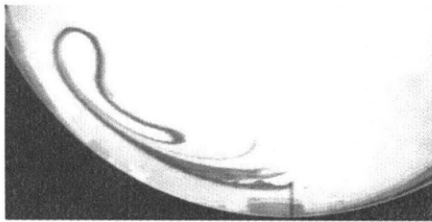
$t / T_{osc} = 0.2$



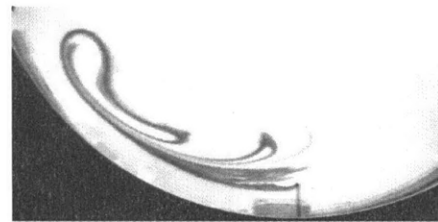
$t / T_{osc} = 1.2$



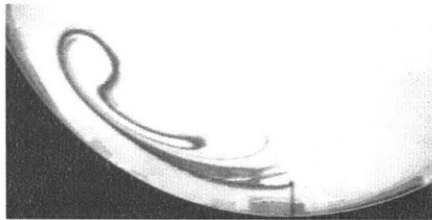
$t / T_{osc} = 0.4$



$t / T_{osc} = 1.4$



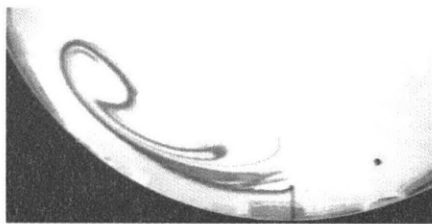
$t / T_{osc} = 0.6$



$t / T_{osc} = 1.6$



$t / T_{osc} = 0.8$



$t / T_{osc} = 1.8$

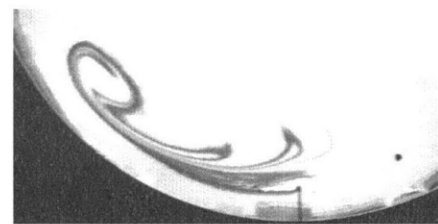
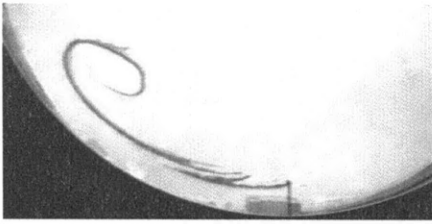


Figure L3: Time series of a dye streakline in the tank where $\delta=1.25$, $A_{osc}=0.15$, and $T_{osc}=131$ s. The time printed above each image is normalized by the lid oscillation period, T_{osc} . The entire figure covers two full oscillation periods, during which the contorted unstable manifold of the inertial recirculation indicates the shape of the exchange lobes. This figure is similar to figure L2, but for a case with stronger unsteady forcing.

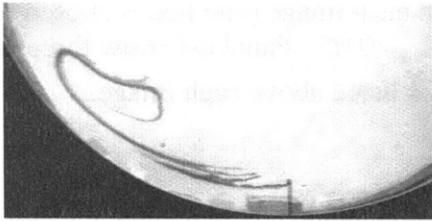
$t / T_{osc} = 0$



$t / T_{osc} = 1$



$t / T_{osc} = 0.2$



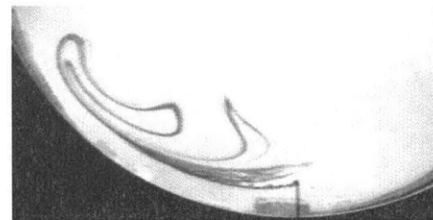
$t / T_{osc} = 1.2$



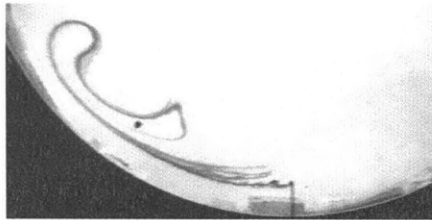
$t / T_{osc} = 0.4$



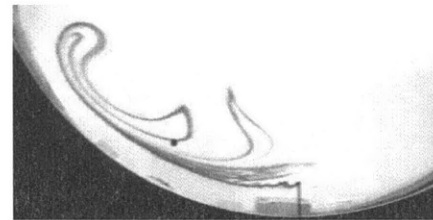
$t / T_{osc} = 1.4$



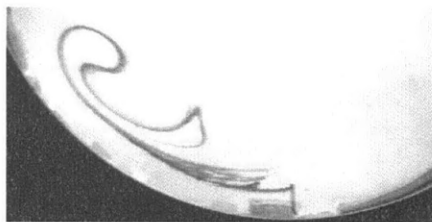
$t / T_{osc} = 0.6$



$t / T_{osc} = 1.6$



$t / T_{osc} = 0.8$

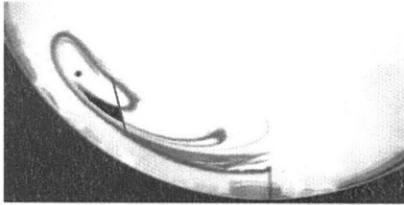


$t / T_{osc} = 1.8$

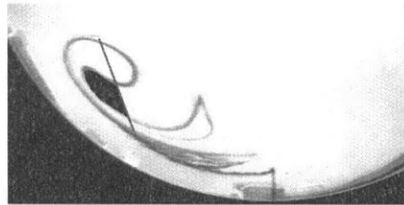


Figure L4: Exchange lobes for two unsteady cases at $\delta=1.25$ and $T_{osc}=131s$. Hand-drawn approximations of exchange lobes are shown in black on dye images. Hand-drawn line approximating stable manifold is also shown on each image (one line is chosen for each forcing). Panel a-c show the three lobes for $A_{osc}=0.05$. Panel d-f show three lobes for $A_{osc}=0.15$. The area of the black region (cm^2) is listed above each image.

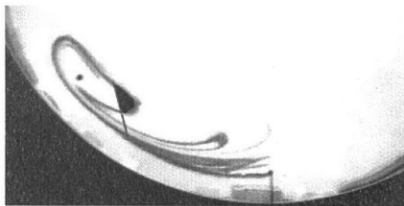
Area = 1.45 cm²



Area = 3.8 cm²



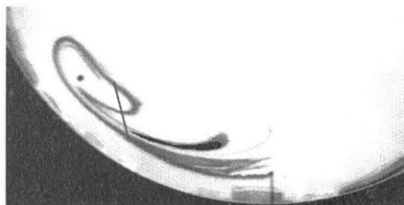
Area = 1.42 cm²



Area = 3.54 cm²



Area = 1.57 cm²

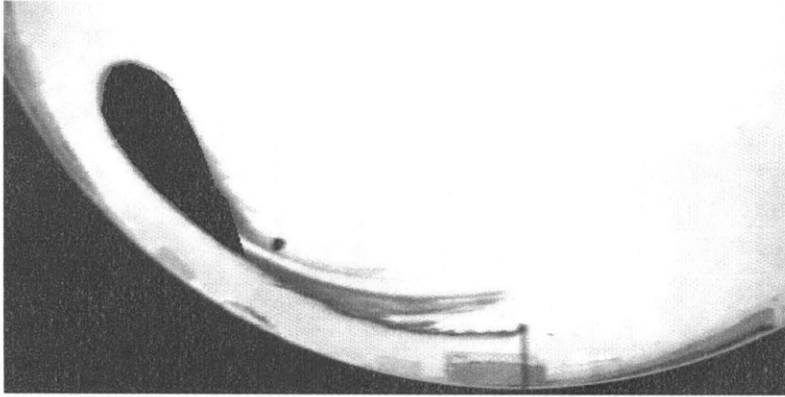


Area = 4.36 cm²

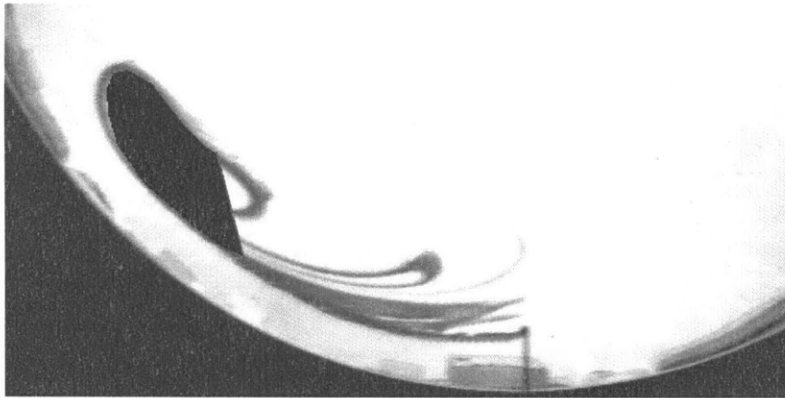


Figure L5: Recirculation region for steady case and two unsteady cases. Panel a shows hand-drawn recirculation from dye streaklines for steady case, $A_{osc} = 0$. Panel b-c show unsteady cases $A_{osc} = 0.05$ & $A_{osc} = 0.15$, respectively. The boundary of the recirculation is drawn along the unstable manifold until intersection with the line from Figure L5 (stable manifold), and then follows this line back to the hyperbolic point. The area of the black region (cm^2) is listed above each image.

Area = 13.94cm²



Area = 13.76cm²



Area = 13.55cm²



VIII. Effective Diffusivity Calculations:

Background on Effective Diffusivity:

The overall idea of effective diffusivity is to quantify the mixing in a flow by diagnosing the geometric complexity of a tracer field. The advection-diffusion equation for a tracer is rewritten by incorporating the advective stirring into the diffusion term. The resulting ‘effective’ diffusion coefficient k_{eff} depends on both the contortion in the tracer field and the molecular diffusivity.

Nakamura (1995, 1996) derived an expression for effective diffusivity by rewriting the advection-diffusion equation for a tracer so that the advection term is incorporated into the diffusion. This is accomplished by first describing the area $A(C,t)$ enclosed by a given contour C of the tracer (here I adopt the notation used by Haynes and Shuckburgh(2000)). This area may be non-contiguous and the total A includes all ‘islands’ in which the tracer concentration c is greater than or equal to C . Because $A(C,t)$ is a single-valued function, we can inversely define $C(A(C,t),t)$ as the value of c for which a given area A is enclosed at the moment t . This allows a rewriting of the advection-diffusion equation as follows.

Our original equation takes the form:

$$\frac{\partial c}{\partial t} + J[\psi, c] = \nabla \cdot k \nabla c + S \quad (1)$$

where c represents the concentration of some tracer, the Jacobian represents advection, the diffusive term represents non-advective transport and diffusion, and S represents a source or sink term. I will assume $S=0$ and that the flow is two-dimensional, although neither of these are necessary to the derivation. I also assume that each contour is closed, so that the boundary of the domain is a constant contour. Then with incompressibility:

$$\nabla \cdot \bar{u} = 0 \quad \bar{u} = \bar{u}(x, y)$$

we integrate (1) over the Area= $A(C,t)$, and employing Reynolds Transport Theorem, we can write:

$$\frac{\partial C(A,t)}{\partial t} = \frac{\partial}{\partial A} \left(k L_c^2 \frac{\partial}{\partial A} C(A,t) \right) \quad (2)$$

where the square of the effective length is given by:

$$L_e^2 = \frac{\langle |\nabla c|^2 \rangle}{(\partial C / \partial A)^2} \quad (3)$$

and $k_{eff} = kL_e^2$. Again as in Shuckburgh, $\langle (\cdot) \rangle$ denotes average over the area between adjacent tracer contours and is defined by:

$$\langle (\cdot) \rangle = \frac{\oint (\cdot) \frac{dl}{|\nabla c|}}{\oint \frac{dl}{|\nabla c|}} \quad \text{or, equivalently} \quad \langle (\cdot) \rangle = \frac{\partial}{\partial A} \iint (\cdot) dA$$

We can diagnose the interplay between advection and diffusion by studying the r.h.s. of (2). This term looks like the diffusion term on the r.h.s. of (1), but the importance of stretching and stirring of tracer contours is explicit in the inclusion of the effective length. This effective length diagnoses the convolution of the tracer contours, and will grow large as the fluid is stirred by advection. The effective length is related to the actual length of the contour by:

$$L_e^2 = L^2 \left(\overline{\frac{1}{|\nabla c|}} \right) \overline{|\nabla c|} \geq L^2 \quad \text{where } \overline{(\cdot)} = \frac{\oint (\cdot) dl}{\oint dl}$$

so that $L_e^2 = L^2$ only if the gradient of the tracer concentration is equal everywhere on the contour. Otherwise the effective length is always longer than the actual length. As a fluid becomes well-stirred long filaments of tracer appear. These result in high gradients throughout the well-stirred region. This process is reversible, but any mixing that occurs across these contours is not. Thus irreversible (diffusive or turbulent) mixing is more likely in regions of high (advective) stirring. The effective diffusivity $k_{eff} = kL_e^2$ captures the importance of stirring in bringing about mixing.¹

Various investigators have employed this diagnostic to characterize mixing in actual and numerical flow fields. Nakamura (1996) examines k_{eff} in a numerical simulation of Kelvin-Helmholtz instability. In other work (Nakamura (1995) and Nakamura & Ma (1997)) calculate k_{eff} from satellite measurements and GCM predictions of nitrous oxide in

¹ As both of these processes, stirring creating high gradients and diffusion eroding them, act simultaneously, complicated feedbacks arise. Nonetheless, unless a fluid is completely homogenous, high advective stirring will always result in enhanced diffusive mixing. This is obvious in the mathematical formulation presented above and has been confirmed empirically by Nakamura (1995).

order to characterize the mixing in the southern hemisphere stratosphere. Haynes and Shuckburgh (2000) employ a kinematic model based on observed (ECMWF) stratospheric winds to advect a numerical tracer with the advection-diffusion equation given above (2).

Results from these investigations indicate that: 1) effective diffusivity characterizes the structure of the underlying flow independent of the particular tracer employed, 2) high values of k_{eff} correspond to mixing regions while low values occur in barrier regions, 3) the magnitude of k_{eff} is dependent on the magnitude of k , but the structure is not (as long as k is spatially uniform), and 4) when an atmospheric observational velocity field is continuously applied to calculate $k_{eff} = kL_c^2$, the flow is independent of initial tracer conditions after an adjustment time (of one month). I will return to these points in discussing my results.

These researchers also clarify the usefulness of this diagnostic. Effective diffusivity can be calculated from a snapshot of the tracer field and the calculation itself includes only integrals and derivatives with respect to the area A within contours. This is advantageous because line integrals (involving edge-finding routines) are difficult to perform numerically. In addition, the nature of the measurement is such that, although calculated from a snapshot, it implicitly contains some ‘memory’ of the flow history. This is because the tracer contours at any time are the result of all recent stirring, or a series of recent stirring events. In these experiments a stirring event is a ‘turnstile’ exchange of a dynamical lobe. In the work on atmospheric mixing mentioned above, stirring events are often the result of large-scale wave-breaking. Effective diffusivity is not useful for diagnosing particular stirring events; it is useful for describing the cumulative effect of these events. (See Haynes and Shuckburgh (2000) for further discussion of the difference between this method and other methods based on calculations of particle separation, etc.)

Procedure for Effective Diffusivity Calculations:

In these experiments the tracer is dye injected into the laboratory tank and I calculate L_e^2 from digital images of the dye patterns. I prepared and spun up the tank in the manner described in the laboratory section above. I then began injecting dye into the flow. The dye was injected at a constant rate for a set period (twenty-three minutes), so that the volume of dye in each case is approximately equal. The dye was injected along a radius of the tank, close to the western wall. The distance from the wall could be varied, so that for some runs I was feeding dye into the western boundary current and for others I was feeding dye into the Munk recirculation. (This set-up is the same as the one used to produce the images of lobes presented in the previous section). Some L_e^2 calculations are from images taken nine minutes after the dye pump is stopped, others are taken twenty minutes later. In the latter cases this adjustment time is much longer than the winding time required for one recirculation of the dye around the entire pattern.

This particular procedure for initializing a tracer field in the tank has a strong effect on the resultant L_e^2 . I could have chosen other procedures, such as initializing the tracer field with some volume of dye distributed over features of interest in the flow (i.e. each of the recirculations). This particular method proved to be the most experimentally viable, and allows me to compare ‘like’ cases where the dye is released in the same location, and also to show some interesting features of the structure by injecting the dye in slightly different locations. These results for L_e^2 are therefore not meaningful in their absolute value, but rather in their relative magnitude.

In order to guarantee consistency in the calculations, all relevant laboratory and analysis techniques were carried out in the same manner for every run. Each digital image was ‘masked’ in order to remove all dark pixels that were not dye (i.e. the dye injection needle, the edges of the tank, etc.). I did this by creating a mask from an image taken at the start of each run before any dye was injected into the flow. I then applied this mask to the dyed image and use the following procedure to calculate effective length:

$$L_e^2 = \frac{\frac{\partial}{\partial A} \iint |\nabla c|^2 dA}{\left(\frac{\partial C}{\partial A}\right)^2} \quad (4)$$

where the concentration value c is an integer (0-255) assigned to each pixel location in the digitization process, C is the chosen contour of concentration (where high values of C correspond to dark areas of dye), and A is the area enclosed by C , $A(C,t)$.

First, the linear gradient ∇c was calculated using centered finite differences (at edges one-sided differences were used). The remaining calculation was completed in a step-wise manner, starting at the highest value of C , which corresponds to the darkest dye and the smallest area. For each value of C the total number of pixels with $c > C$ gave the area = $A(C)$. The magnitude of $|\nabla c|^2$ on these pixels was then summed to approximate the area integral in the numerator of (4). When $A(C)$ and $\iint |\nabla c|^2 dA$ had been found for every value of C (from 255 to 0), the two area derivatives were calculated using centered finite differences. The last step was a conversion from $pixel^2 \rightarrow cm^2$ to give $L_e^2 (cm^2)$. This effective length can be plotted as a function of either C or A . We can garner different information from each and I present plots of both types below.

Results of Effective Diffusivity Calculations:

In this section I present comparisons of L_e^2 for steady and unsteady flows with and without hyperbolic regions. I find L_e^2 is significantly higher in unsteady flows with hyperbolic regions than in the other cases. This is evidence of the enhanced mixing generated by tangled manifolds and the associated turnstile lobe exchange. I show this through a number of comparisons.

First, I compare the effective length for two steady cases: one single recirculation (without a hyperbolic point) and one double recirculation (with a hyperbolic point). Because the flow is steady, the change in geometry does not significantly effect mixing, and the resultant effective lengths are similar. Next, I compare *unsteady* cases. With unsteady forcing the effective lengths for double recirculation cases far outstrip those for the single recirculations. The initial steady comparison clarifies that these differences are not due to the higher inertia in the double recirculation geometry ($\delta=1.25$ for double, $\delta<1.10$ for single). This difference in mixing ability is instead due to the turnstile lobe exchange. I also present further evidence of the importance of the change in geometry by

showing a plot of L_e^2 vs. δ and I end with a note about the spatial distribution of effective length, and its component terms.

Figure K1 shows the similarity in L_e^2 for the steady cases. The top panel contains L_e^2 plotted as a function of contour value, C . The solid line is for the single recirculation case ($\delta=1.00$) pictured in panel b. The dashed line corresponds to the double recirculation case ($\delta=1.25$) depicted in panel c. In both cases the dye is injected into the western part of the Munk recirculation. (The asymmetries in the double recirculation case are discussed above in relation to figure L1). I have noted consistent periodic minima in L_e^2 that appear approximately every 12 contour values, but I am unsure of their origin. They do not affect comparison.

Figure K2 again presents a comparison of effective length for the two geometries, but here the flow is unsteady with $A_{osc}=0.05$. The maximum L_e^2 for $\delta=1.25$ is more than three times that for $\delta=1.00$. Here the dye was injected into the western boundary current outside the Munk recirculation, which gives rise to some interesting contrasts with Figure K1. The dye was injected for 23 minutes and photos were taken at $t=54$ minutes. Note that the dashed line ($\delta=1.25$) was calculated from the image shown in Figure K6, panel b.

Because the dye is injected inside the recirculation in K1 and does not mix into the interior or boundary current, the values of effective length remain low, $O(100 \text{ cm})$. When the dye is injected into the boundary current (and the flow is unsteady) L_e is $O(400 \text{ cm})$ for the double recirculation and $O(200 \text{ cm})$ for the single recirculation. In addition to these differences in magnitude, Figure K1 and K2 differ in the distribution of L_e^2 . When the dye does not mix much, the longest effective lengths remain at high contour values: the dye is concentrated and high gradients exist in only a few locations, as in Figure K1. Figure K2, in contrast, shows the maximum effective lengths at lower contour values, corresponding to long, lighter, filamented dye regions. We see this shift in distribution of effective length in other well-stirred cases.

An even more dramatic transition is depicted in Figure K3. In order to compare a number of *unsteady* cases, I plot the mean value of L_e^2 as a function of $\delta = \delta_l / \delta_M$ (at $t=32$ minutes in panel a & and at $t=54$ minutes in panel b). In addition, I present the full range of L_e^2 for one case at each value of δ (panels c & d). The open circles are cases with the dye is injected inside the western part of the Munk recirculation in each case, so that the

dye initially leaves the needle heading north, and then recirculates back south. The asterisks represent cases with dye injected into the very middle of the Munk recirculation.

We can clearly see a sharp increase in L_e^2 at the transition to a double recirculation, hyperbolic geometry around $\delta=1.13$. Because of the existence of the hyperbolic point, the dye pattern for the double recirculation pattern displays a complex dependence on the location of the dye injection (even within the Munk recirculation) which I explore this further below. The uncertainty bars in Figure K3 are based on repeated runs at $\delta=1.25$ and $\delta=0.75$. The repeat runs at the former value show a much larger spread, so this range is used as an outside estimate for uncertainty at all values of δ .

Notice in panel d the jump in total area covered by dye in the hyperbolic case, $\delta=1.25$. This is because only dyed pixels contribute to the calculation of effective length, and as the dye stretches and diffuses into previously clear fluid, the total area of dyed pixels increases (and the area of very dark pixels decreases). This is another indication of increased stirring and mixing in the unsteady hyperbolic case.

Photos of three representative flows are presented in K4. These images are from three of cases shown in Figure K3. From top to bottom the panels depict $\delta=0.75$, 1.00, and 1.25, respectively. Notice that the scale is larger on the top panel. The prominent difference between these photos and those from the steady case is the remnant exchange lobes evident towards in the interior in panel c. The lobes we saw in the previous section had a thin, streakline quality, as the images were taken near the beginning of a run, $t \approx 0$ (10 minutes). This image shows the lobes at $t=54$ minutes, after enough previous lobes have wrapped up inside the inertial recirculation that new lobes carry out only fluid that has been imported in at some point since the dye began. The clear fluid in the center of the inertial recirculation (still there after fifty-four minutes!) is the experimental evidence for invariant KAM tori. Note that even with unsteady forcing the dye fills a simple recirculation area (without lobes) in the non-hyperbolic cases.

As further evidence of the difference between the runs with and without hyperbolic points, I present two contrasting cases in Figure K5. I compare cases with steady and unsteady forcing in a single recirculation geometry (top panel) and double recirculation geometry (lower panel). Effective length is plotted as a function of contour value C and the scale on both plots is the same. We can clearly see unsteadiness has a negligible effect on the single recirculation and a large effect on the double recirculation. In addition, this figure contains independent measurements of L_e^2 from three experiments at the same

parameter settings and dye injection location (blue lines on bottom panel). These give some idea of the uncertainty in this calculation. All three of these cases have a mean and maximum value that is much higher than the steady case (as evidenced in Figure K3), but their detailed structure is not consistent. This is due to a number of factors. In some cases the tank water was used for more than run so that the contrast of the dye water to tank water was somewhat variable. This accounts for the low values of effective length in the range $10 < C < 60$ for case q4: background color in the tank made the light, wispy part of the dye pattern somewhat indistinguishable. There is also some uncertainty in the measurement of Δr (injection location) and some variation in the rate at which dye is pumped into the tank, and these may be the reasons that case q6 has low effective lengths at the highest values of C (darkest dye). These runs are meant to encompass all such experimental and laboratory variables affecting reproducibility.

In Figure K6 I illustrate the effect of injecting dye in different locations. Panel a shows mean effective length as a function of Δr (injection location). Open circles represent unsteady, hyperbolic cases ($\delta=1.25$ and $A_{osc}=0.05$). Crosses represent unsteady, non-hyperbolic cases ($\delta < 1.25$ and $A_{osc}=0.05$). All of these measurements are at $t=54$ minutes. Δr is measured in cm from the western tank wall. Photos in panels b, c, & d show dye patterns for runs at $\Delta r=2.5$, 3.9, and 5.0.

Panel b depicts the sole case with dye injected in the western boundary current, outside of the Munk recirculation ($\Delta r=2.5$). This image encapsulates the effect of turnstile lobe exchanges every 131 seconds for fifty-three minutes. As the dye first left the needle it traveled in a large circulation path outside of both recirculations, but the lobe exchange proceeded to work the dye further and further in towards the hyperbolic point and into the recirculations. The role of the lobes in this stirring is confirmed by runs at the same Δr in steady hyperbolic cases and unsteady non-hyperbolic cases, during which the dye remained on an outer path for the entire run.

The rest of the circles in panel a represent eight cases with the dye injected at various locations within the Munk recirculation, ($\Delta r > 3.0$). As mentioned above, these dye patterns display a rich behavior in this hyperbolic case that is not apparent in the single recirculation cases. At $\Delta r=3.5$, dye was injected in western Munk recirculation (dye headed north initially). At $3.5 < \Delta r \leq 4.5$ dye was injected into middle of Munk recirculation and initial dye movement was very slow and in both directions. At $\Delta r \geq 5.0$

the dye was injected into the eastern part of the Munk recirculation, and the dye moved south from the needle.

Most of the runs when dye was injected into the Munk recirculation look very much like the run in panel d (see discussion below). The only notable exception to this ‘typical’ appearance is the case presented in panel c ($\Delta r=3.9$). During this interesting run, the dye was injected into the middle of the recirculation and remained almost completely isolated within the very center of the Munk recirculation. Faint wisps of dyed fluid did leak out into a pattern similar to that in panel d, but these are very hard to see, and were not distinct enough in the digital image to effect L_e^2 . This case results in low L_e^2 . I presume this pattern is due to the invariant KAM tori. If in this case I happened to inject dye inside an invariant tori, it should never get out into the surrounding fluid, except by molecular diffusion.

Panel d depicts a typical dye pattern for these cases. The photos in panels b & d are astonishing in that they could almost be negatives of each other. The dye fluid in panel b clearly marks lobes that initially carried fluid into the recirculations, while the dye in panel d marks fluid that was exported out. Also note the small patch of clear fluid in the middle of the inertial recirculation in panel d and the similarity between the clear region Munk recirculation in panel b and the dyed fluid isolated in the same area in panel c. These patterns are presumably related to the invariant KAM tori mentioned above.

We can acquire some further intuition into the structure of effective length by considering its components. Figure K7 presents a deconstruction of L_e^2 for a run at $\delta=1.25$ and $A_{osc}=0.05$ and dye injected into the western part of the Munk recirculation.

Effective length is plotted in panel b. The linear gradient contribution, $\langle |\nabla c|^2 \rangle$ (see eq. 3), is plotted in panel c and the area gradient contribution, $\left(\frac{\partial C}{\partial A} \right)^{-2}$, is plotted in panel d.

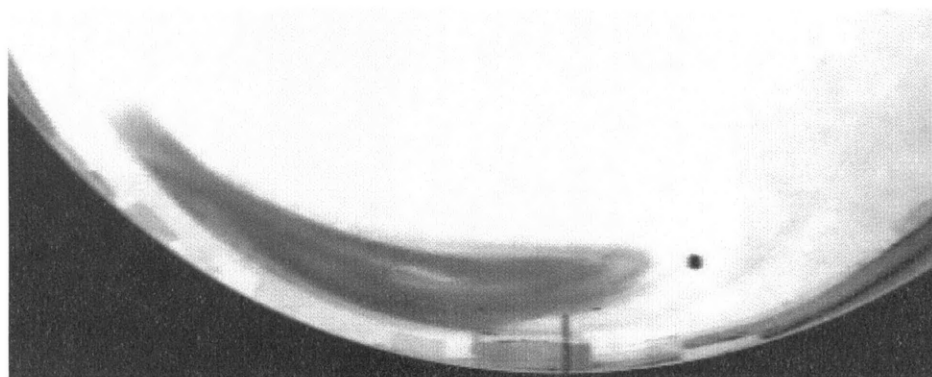
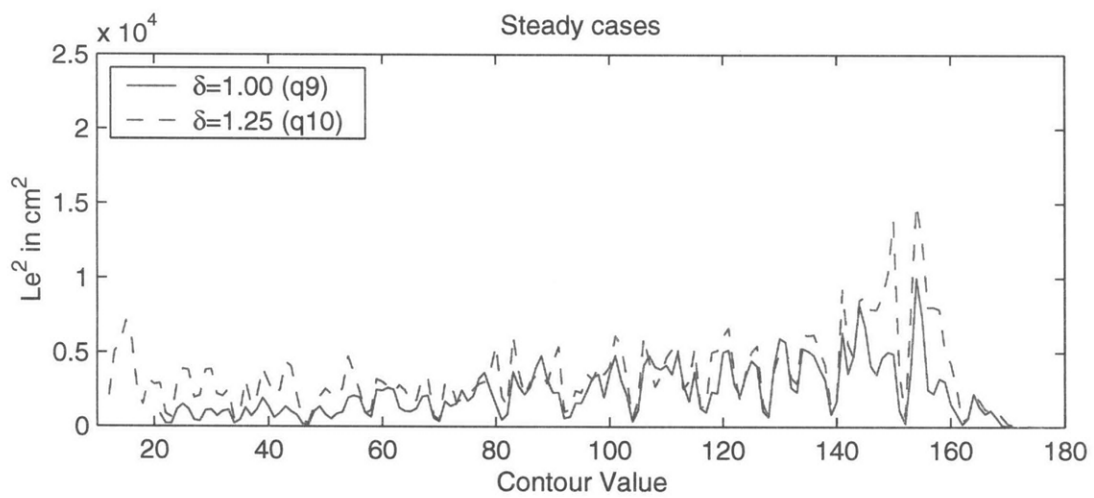
These terms are scaled as is L_e^2 , so that $\langle |\nabla c|^2 \rangle \times \left(\frac{\partial C}{\partial A} \right)^{-2} = L_e^2 (cm^2)$. The magnitude of the linear gradient term is clearly much larger, but the area term plays an important role at the highest contour values. This maximum in the area term (panel c) at $C \approx 145$ corresponds to the dark regions inside the Munk recirculation and ringing the inertial recirculation (the contours on Figure K7a are at $C = 50, 100$, and 145). In these regions the linear gradients are low, but there is a large jump in the area inside contours as one leaves these dark regions and moves into the wispy, lighter contours. I suspect the linear gradients are low

and the area gradients are also low because these dark regions have become largely homogenized. The maximum values of the linear gradient term at lower values of c correspond to the highly contorted dye patterns in the newest exchange lobes ($80 < C < 120$), which are surrounded by the high gradients indicative of advective stirring. The maximum value of L_e^2 ($25 < C < 80$) occurs in the older lobes which are wrapped up on the very outside of the dye pattern. These lobes were initially due to very high advective stirring, but now have slightly lower values of $\langle |\nabla c|^2 \rangle$ and higher values of $\left(\frac{\partial C}{\partial A}\right)^{-2}$ than the newer lobes. I think this is due to some amount of diffusion across the high property gradients. This hints at the complicated interplay between advection and diffusion that results in well-mixed regions of fluid.

Figure K8 presents the same information as Figure K7, but here the dye is injected in the western boundary current, outside of the Munk recirculation (this is the photo shown in Figure K5b). The dye is much more well-mixed in this case, with highly striated regions visible to the naked eye. This is shown in the magnitude of effective length, which is O(2-3) times the magnitude of L_e^2 in Figure K7. In sharp contrast to the previous case, here the shape of L_e^2 as a function of C is almost completely determined by the $\left(\frac{\partial C}{\partial A}\right)^{-2}$ term.

In this section I have presented calculations of effective length, L_e^2 , for steady and unsteady flows with and without hyperbolic regions. I have shown that L_e^2 is significantly higher in unsteady flows with hyperbolic regions than in the other cases. This is evidence of the enhanced mixing generated by tangled manifolds and the associated turnstile lobe exchange. Through use of the effective diffusivity diagnostic, k_{eff} , I have quantified the effects of chaotic advection in a laboratory flow.

Figure K1: Panel a presents a plot of Effective Length as a function of contour value C . Effective Length squared L_e^2 in cm^2 is compared for the two different geometries (single and double recirculation) in the *steady* case. The dye was injected for $t=23$ minutes, these photos and calculations were taken at $t=54$ minutes. The cases correspond to $\delta=1.00$ (solid line) and $\delta=1.25$ (dashed line) and are calculated from the dye images in panels b & c, respectively. In both cases the dye is injected near the edge of the southern Munk recirculation.



$\delta=1.00$



$\delta=1.25$

Figure K2: Effective length squared, L_e^2 (cm^2), as a function of contour value C for two *unsteady* cases ($A_{osc}=0.05$) with dye injected outside the recirculation in the boundary current: a single recirculation at $\delta=1.00$ and a double recirculation at $\delta=1.25$. The dashed line represents a hyperbolic, figure-8, flow; the solid line represents a non-hyperbolic flow. The dye was injected for 23 minutes and photos were taken at $t=54$ minutes. Note that the dashed line ($\delta=1.25$) was calculated from the image shown in Figure K6, panel b.

Figure K2

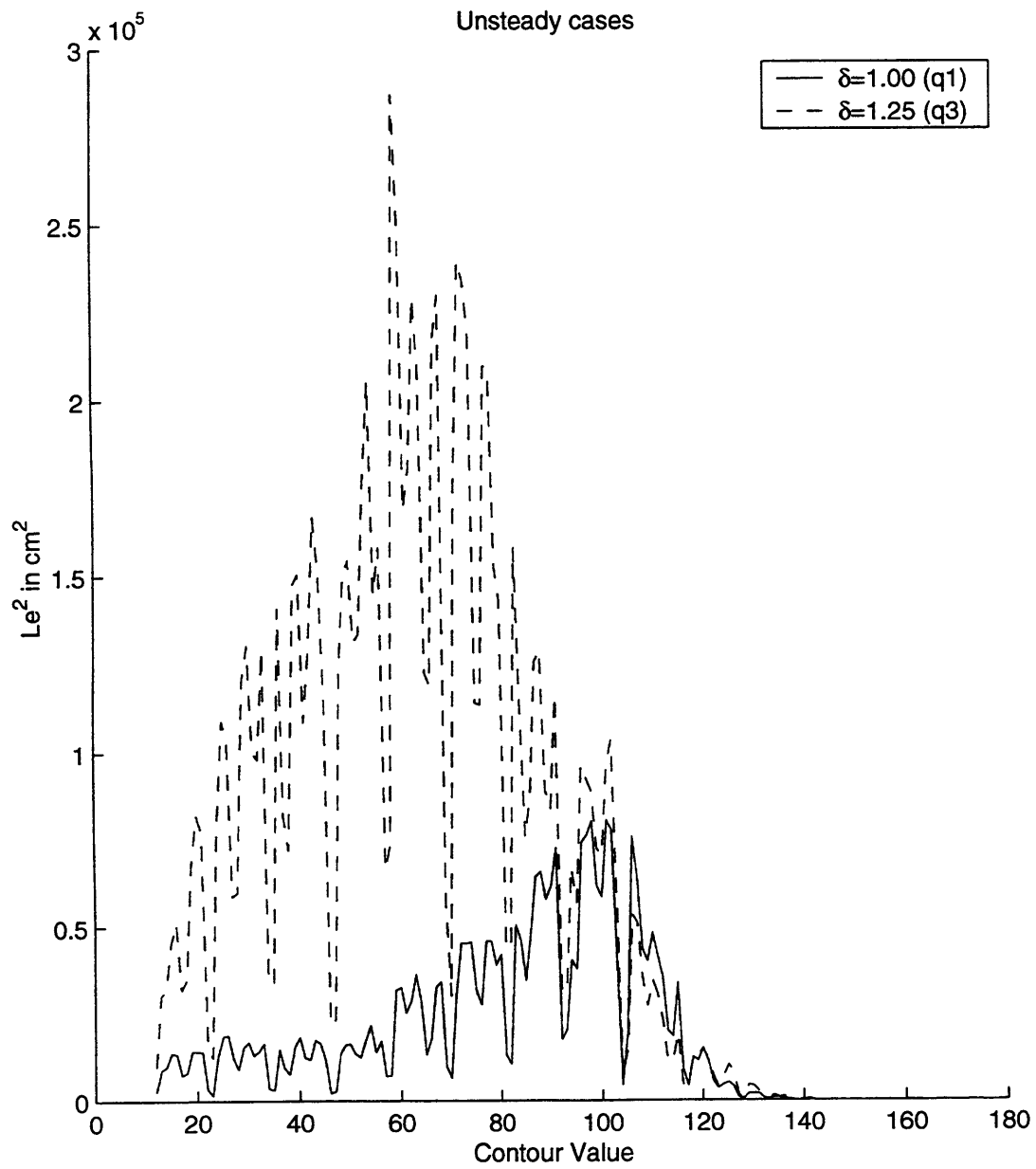


Figure K3: Effective length squared, L_e^2 (cm^2), in *unsteady* cases presented as a function of δ (panels a & b), contour value (panel c), and area (panel d), where $A_{osc}=0.05$ in all cases. Mean of L_e^2 calculated at $t=32$ minutes and 54 minutes are shown in panels a & b, respectively (dye was injected for 23 minutes in all cases). Open circles represent cases with dye injected into the western or eastern part of the Munk recirculation and asterisks represent cases with dye injected into the very center of the Munk recirculation. The uncertainty bars in Figure K3 are based on repeated runs at $\delta=1.25$ and $\delta=0.75$. In panels c & d solid lines represent all single recirculation cases with $\delta < 1.13$, and the dashed line represents the double recirculation case, $\delta=1.25$.

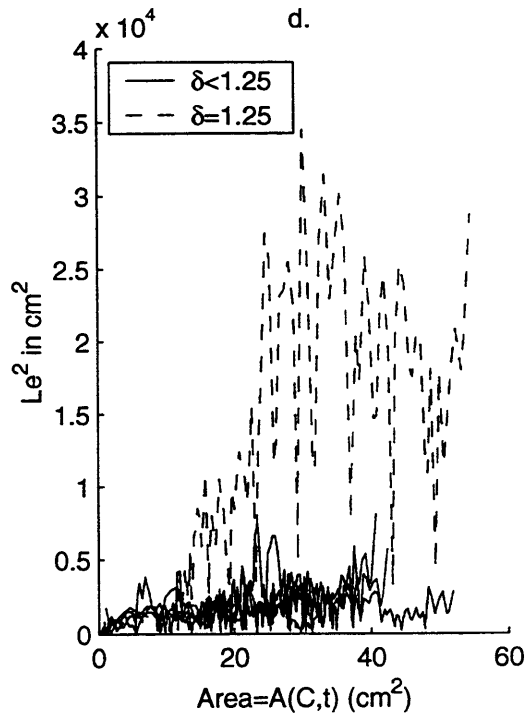
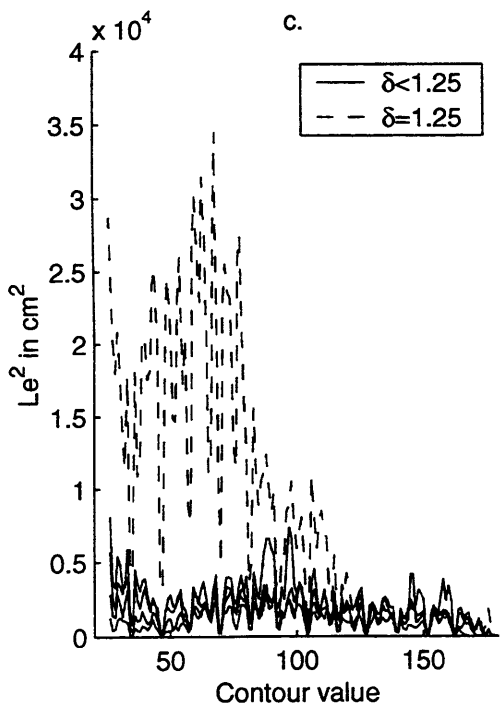
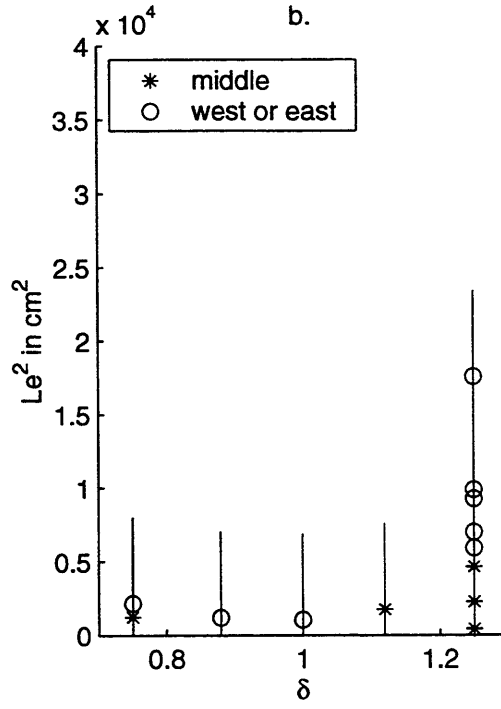
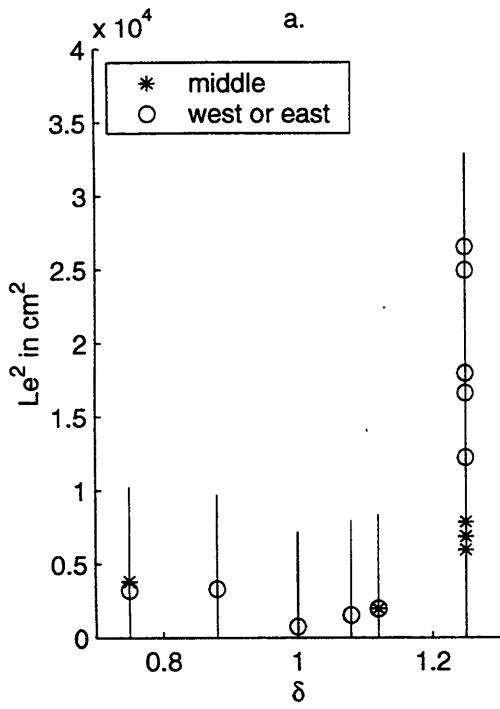
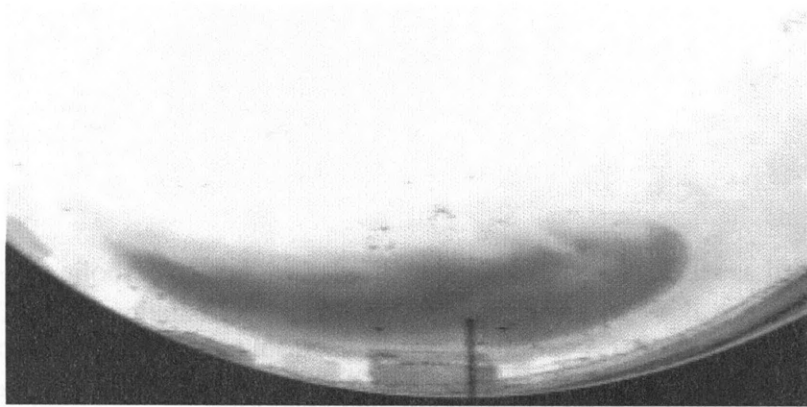
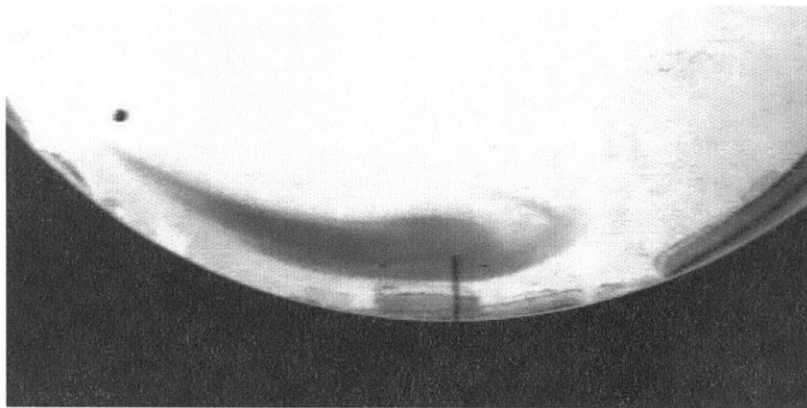


Figure K4: These photos depict the change in structure of the dyed fluid as the lid forcing is increased in *unsteady* cases ($A_{osc} = 0.05$). Photos correspond to cases in Figure K3c at $\delta = 0.75, 1.00,$ and 1.25 . Compare with the photos for steady case in Figure K1.

$\delta=0.75$



$\delta=1.00$



$\delta=1.25$

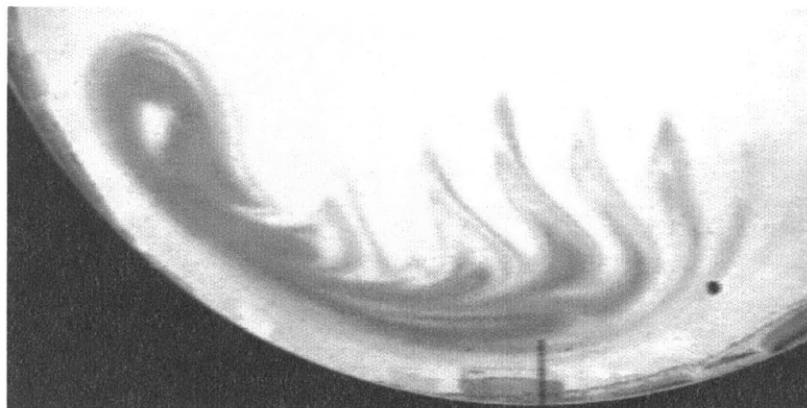


Figure K5: Top panel: $L_e^2 (cm^2)$ in single recirculation, non-hyperbolic geometry, as a function of contour value. Dye is injected within Munk recirculation at $\delta=1.00$. (steady case is solid line, unsteady ($A_{osc}=0.05$) dotted). Bottom panel: Same as top panel, but for double recirculation, hyperbolic geometry ($\delta=1.25$). Multiple (dash/dot) lines represent three experiments at the same parameter settings.

Figure K5

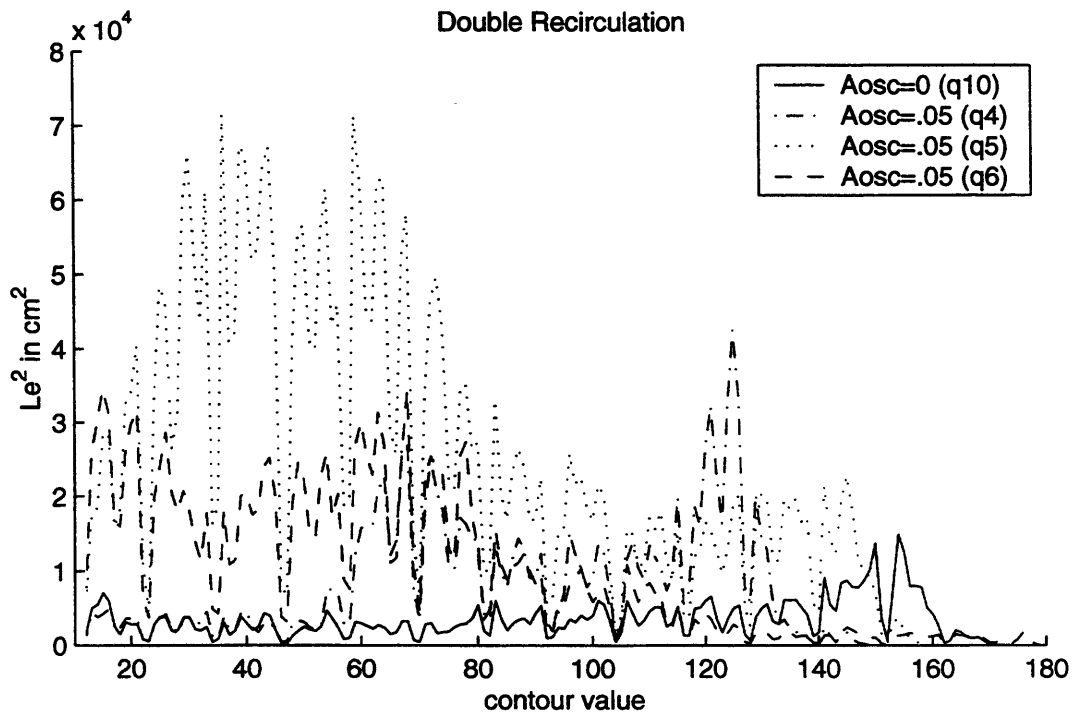
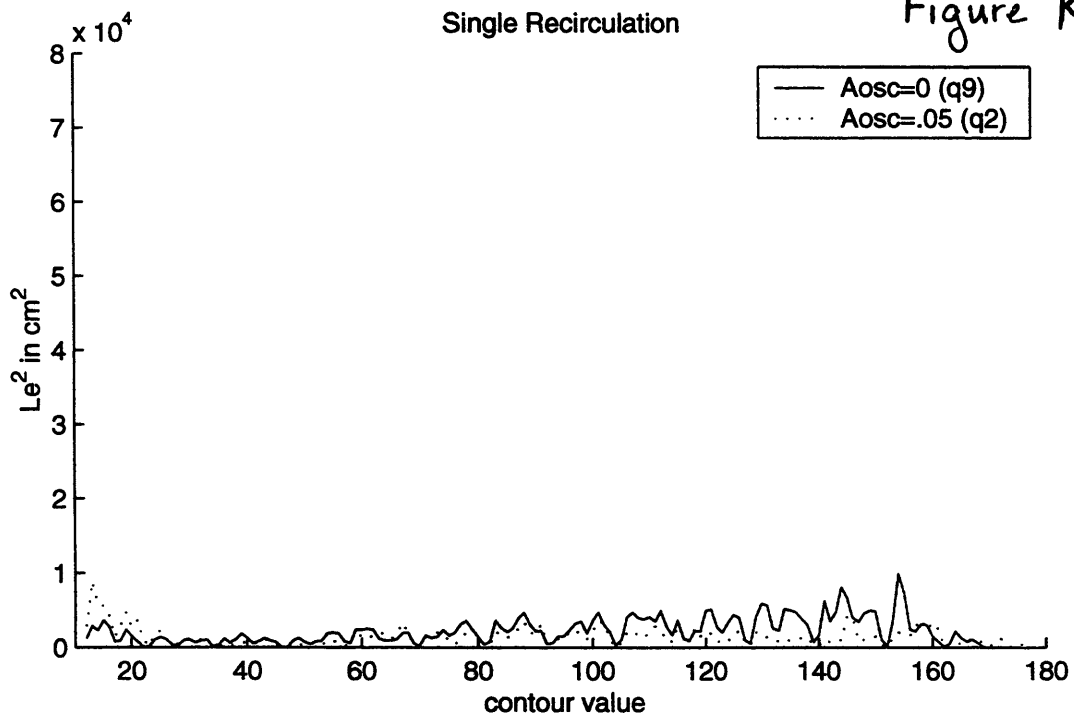


Figure K6: a. Mean Effective length as a function of injection location Δr for *unsteady* cases ($A_{osc}=0.05$ for all cases). Hyperbolic cases ($\delta=1.25$) are open circles. Non-hyperbolic cases ($\delta<1.25$) are crosses. Δr is measured in cm from the western tank wall. Panel b shows dye injected in western boundary current ($\Delta r=2.5$). Panel c & d show dye injected into the center and eastern parts of the Munk recirculation. ($\Delta r=3.9$ & 5.0).

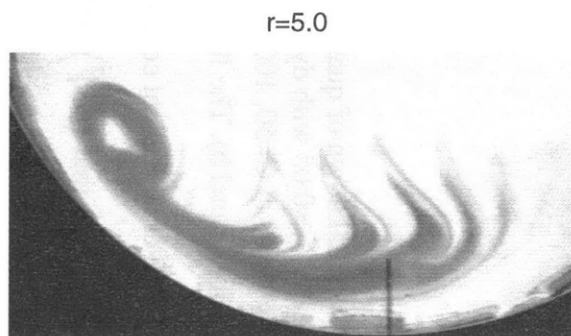
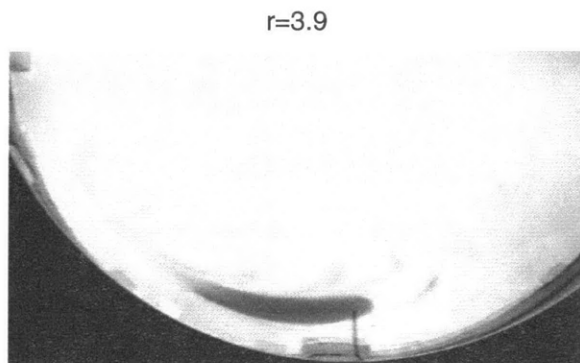
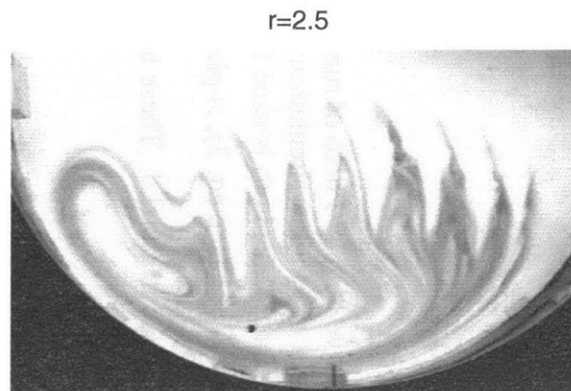
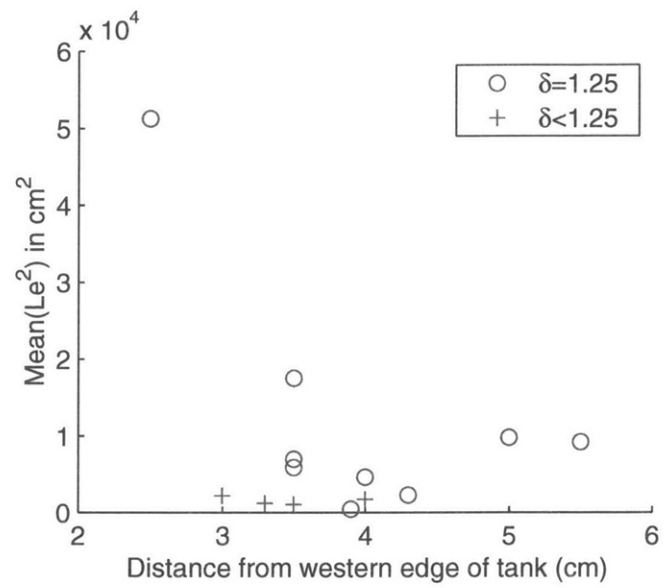


Figure K7: Breakdown of quantities contributing to effective length. Photo of run at $\delta=1.25$ and $A_{osc}=0.05$ with dye injected in the western part of Munk recirculation with overlaid contours at $C=50, 100,$ and 145 is shown in panel a. This photo is used for L_e^2 calculation (panel b). The linear gradient contribution, $\langle |\nabla c|^2 \rangle$ (see eq. 3), is plotted in panel c and the area gradient contribution, $\left(\frac{\partial C}{\partial A}\right)^{-2}$, is plotted in panel d. These terms are scaled as is L_e^2 , so that $\langle |\nabla c|^2 \rangle \times \left(\frac{\partial C}{\partial A}\right)^{-2} = L_e^2 (cm^2)$.

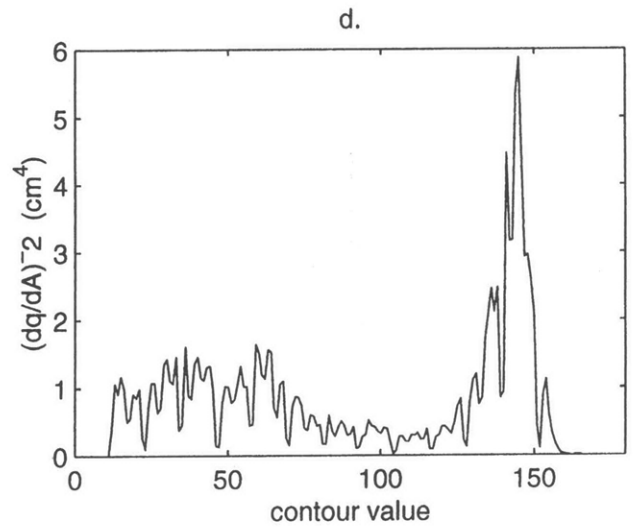
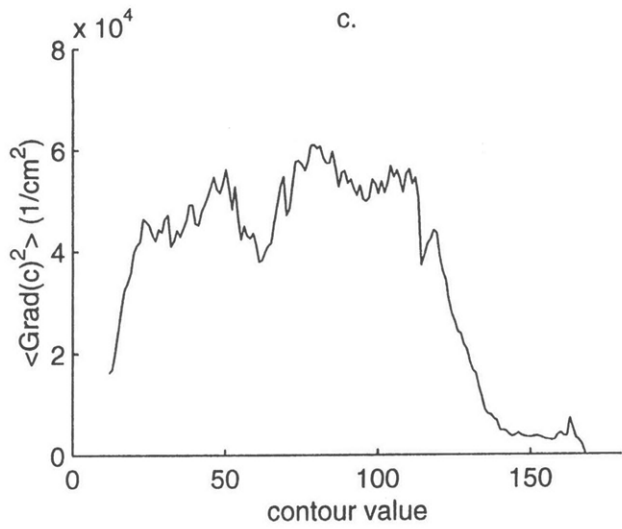
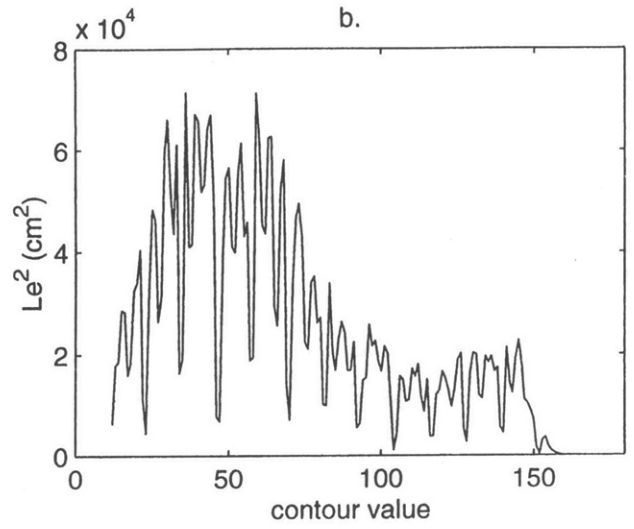
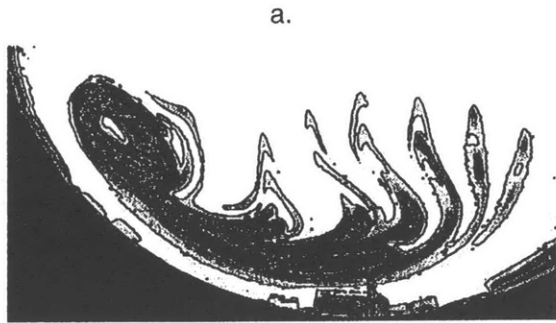


Figure K8: Same as Figure K7 but for a case with dye injected into the western boundary current outside of the Munk recirculation. In this case contours in panel a are at $C= 25, 75,$ and 100.

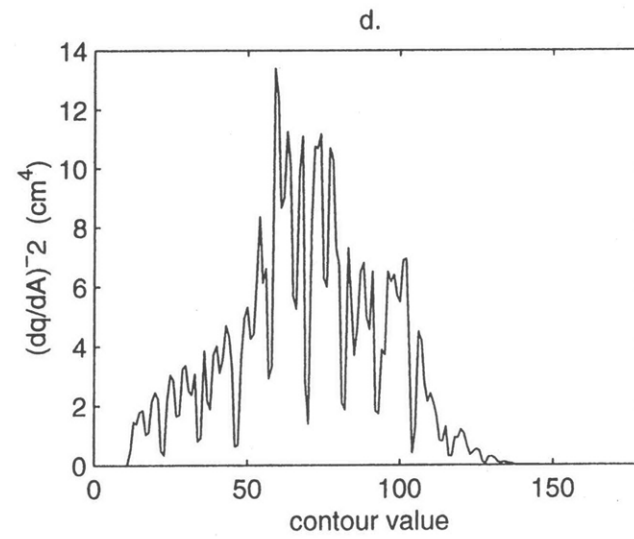
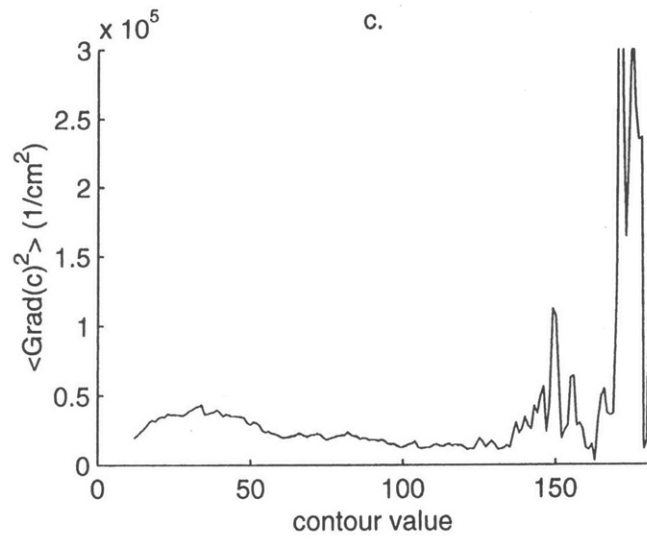
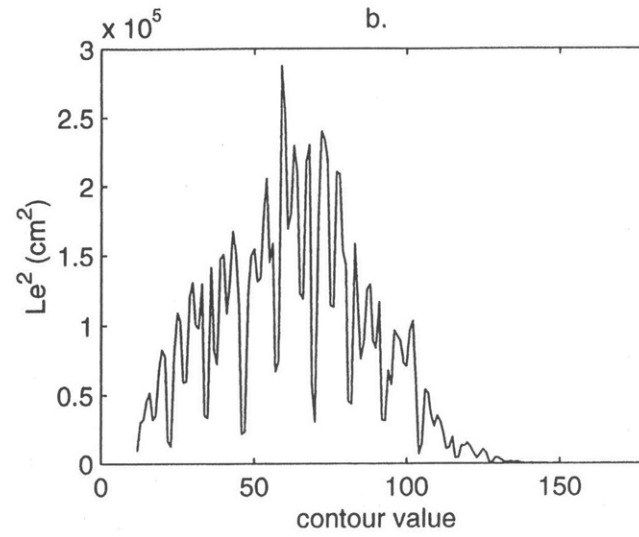
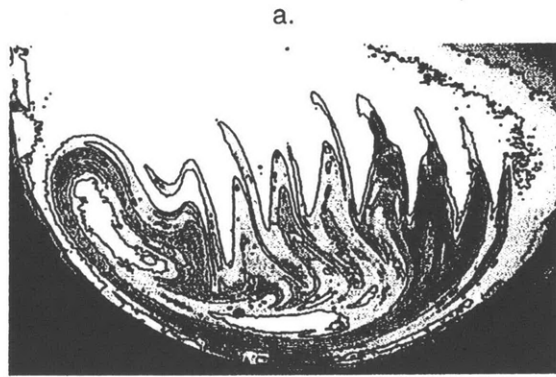


Figure K8

IX. Conclusion:

This thesis work was motivated by the question: Does the existence of a hyperbolic point in a recirculation geometry radically increase the mixing in a flow? The experimental results and analysis presented above indicate that of the two recirculations investigated, the figure-8, hyperbolic geometry clearly results in higher mixing. Furthermore, this mixing is due in large part to chaotic stirring by exchange lobes. Since the increased mixing in the figure-8 geometry is due to the manifolds associated with a hyperbolic point, one important question for future work is whether a similar type of chaotic advection occurs near hyperbolic areas in the oceans. In this conclusion I first summarize my results, then make some comparisons with the oceanographic observations mentioned in Sections II & III, and finally suggest directions for possible future work.

I investigate two flow geometries in a sliced-cylinder rotating tank experiment: a single recirculation and a double, figure-8, recirculation. The double recirculation flow contains a hyperbolic point while the single recirculation does not. I compare these two flows with both steady and unsteady forcing (introduced by rotating the lid at a constant or variable rate). In the steady case, the double recirculation has a homoclinic geometry, with the unstable manifolds of the hyperbolic point coinciding with the stable manifolds of that same point. When some time dependence is introduced we expect that the stable and unstable manifolds will no longer coincide, but will instead intersect (theoretically an infinite number of times) and form exchange lobes. The single recirculation does not have a hyperbolic point and therefore should have neither manifolds nor exchange lobes.

I demonstrate the existence and importance of these exchange lobes in the hyperbolic laboratory flow. Their existence is shown by dyeing fluid near the unstable manifold of the double recirculation. In the steady case this dye streakline traces out a simple curve around the boundary of the inertial gyre, confirming that the stable and unstable manifolds coincide. In the unsteady case the dye streakline forms a series of meanders, first bending into, and then out of, the inertial recirculation. Although I am unable to show the exact location of the stable manifold in this case, the meandering dye clearly indicates the location and movement of the exchange lobes. In unsteady single recirculation cases similar dye streaklines do not result in looping patterns; without a hyperbolic point there are no exchange lobes.

Further confirmation that the dye streakline indicates lobes in the hyperbolic case is supplied by a time series of velocity in the tank. The time series and associated power spectrum density clearly show unsteadiness in the flow at the lid oscillation (forcing) period. The loops in the dye streakline are mapped onto each other (indicating exchange lobes mapped onto the space occupied by the previous lobe) at exactly this period.

Although I am not able to trace the stable manifold directly in the laboratory, I am able to draw a line approximating the portion of the stable manifold approaching the hyperbolic point. This line is drawn so that the resulting lobes enclose equal areas, as they should in a periodic flow. A 'recirculation' boundary can then be identified for the unsteady cases by tracing the unstable manifold up to the first intersection with the line approximating the stable manifold, and then following that line. The resulting recirculation areas are approximately equal to the steady recirculation area, regardless of the amplitude of unsteady forcing.

I find that the size of the resulting exchange lobes is strongly dependent on the amplitude of the unsteady forcing. Using the lobe areas and the recirculation areas I calculate approximate flushing times, which represent the time to replace all fluid that is exchanged. I approximated ratios of flushing time to winding time: $T_f / T_w \approx 6$ at forcing amplitude $A_{osc} = 0.05$ and $T_f / T_w \approx 2$ for $A_{osc} = 0.15$. The much larger lobes in the case with stronger time dependence ($A_{osc} = 0.15$) give rise to a very short flushing time. These rapid flushing times testify to the vital role lobes can play in homogenization of the recirculation and exchange between the recirculation and other regions. In addition, I observe a region inside the recirculation which is unaffected by the lobes and remains unmixed (and unstirred) with its surroundings; the size of this region is much smaller in the case with stronger unsteady forcing. This inner region is surprisingly persistent, considering the efficiency of dye mixing in the rest of the fluid, and may be related to invariant KAM tori.

In general, these laboratory results are in line with previous analytical and numerical work on lobe dynamics. One interesting feature of these experiments is that the forcing period is equal to or less than the winding time, T_w , required for a parcel to circumnavigate a recirculation $T_w = O(T_{osc})$. Chaotic advection is generally favored when the characteristic Eulerian time scale, here T_{osc} , is much less than the Lagrangian time scale, here T_w . This time scale separation is consistent with coherent structures and persistence of hyperbolic

trajectories over many cycles of parcel motion. However, there is not a formal requirement that $T_w \ll T_{osc}$ and, indeed, $T_w = O(T_{osc})$ in this laboratory experiment.

The complex dye patterns in the hyperbolic cases are dramatic demonstrations of the effects of chaotic advection. The dye is stretched and folded into highly contorted patterns in the hyperbolic cases, while in the non-hyperbolic cases the dye simply recirculates around a small area. In order to quantify the results of strong or weak advective stirring on the mixing ability of the flows, I employed a diagnostic known as effective diffusivity, κ_{eff} and a corollary known as effective length, L_e .

The squared effective length was calculated from images of dye in the tank. The results clearly show that in steady flows the effective length is relatively low and not strongly influenced by the existence of a hyperbolic point. With even slight time dependence in the flow, this ceases to be true and the effective lengths for the hyperbolic cases were much larger than those for the single recirculation. The initial steady comparison clarifies that these differences are not due to the higher inertia in the double recirculation geometry ($\delta=1.25$ for double, $\delta<1.10$ for single), but are instead due to enhanced stirring generated by tangled manifolds and the associated turnstile lobe exchange. In addition to comparing the mean value of effective length for different geometries, I briefly note the spatial distribution of L_e^2 through a discussion of the dependence of effective length on contour value.

At the outset of this thesis I outlined a series of questions about recirculations between a fast boundary current and a slow interior flow. The results outlined above allow me to answer many of these questions with regards to the laboratory flow and make some suggestions about analogues in the ocean. I can now identify how altering the geometry of the recirculation region affects the mixing characteristics of the flow: introducing a hyperbolic point into an unsteady flow drastically increases the advective stirring and the overall mixing. I can also identify the important dynamics that underlie the mixing in these laboratory flows as chaotic advection and diffusion (both molecular diffusion and double diffusion of the tank water and the dye mixture).

I also asked other questions about the mixing along the edges of the recirculation(s). Are particles more likely to exit back into the boundary current or into the interior flow to the east? How quickly is the fluid inside the recirculations homogenized. The answers to these questions are very different in the unsteady hyperbolic case than in the non-hyperbolic and/or steady case. In the former case, the mixing is determined by the

efficiency with which the lobes exchange fluid with the interior and boundary current and stir fluid within the recirculation. In the latter cases the exchange with outside regions and homogenization within the recirculation are both slow processes, largely dependent on diffusion and the ballistic effects of varying recirculation speed at different distances from the center of the recirculation.

In a periodic flow with homoclinic geometry (my figure-8 case), the lobes on either side of the recirculation must have equal area, so that equal amounts of fluid should be exchanged with both the boundary current and the interior. It appears, however, that the lobes have very different shapes on either side of the recirculation, so that while they transport equal amounts of fluid, the fluid is transported far into the interior, and only barely into the boundary current. Although I did not observe the entire lobe outlines, I confirmed that the lobes did not reach far into the boundary current by injecting dye outside of the figure-8 into the boundary current. In these cases dye only mixed into lobes on the interior side of the recirculations. This confirms that while the same amount of fluid should come from (and be delivered to) the wbc and interior, only fluid on the very edge of the wbc makes it into the recirculations, while fluid far into the interior can be captured in the lobes. This particular homoclinic geometry has some behaviors in common with the heteroclinic jet geometry explored by other investigators, but also shows some interesting differences.

In a heteroclinic geometry (with periodic forcing) the lobes on either side of the recirculation need not be the same size. Rogerson, et al. (1999) tracked lobes numerically in a heteroclinic jet geometry and found large lobes reaching far into the 'interior' (region away from the jet) and small lobes which did not stretch far into the jet. The authors also found invariant regions within the recirculations (presumably KAM tori), but due to the difference in lobe sizes, the invariant regions sat much closer to the jet edge of the recirculations, whereas the immune regions in these homoclinic experiments appear approximately in the middle of the recirculating region.

We would like to distill information from lab results that would be useful in both interpreting past observations and planning future work. Almost all deep oceanographic observations are Eulerian in nature (i.e. point measurements such as current meters or hydrographic surveys). There are Lagrangian observations, namely float studies, but these are rare in the deep ocean. Part of the purpose of this work was to take a step toward being able to say something about Lagrangian effects (of chaotic advection) given a Eulerian

(mean) flow field. Theoretically, if we know the mean streamlines of a flow (basic geometric configuration) and the dominant unsteady time scales, we may be able to say whether we expect chaotic advection by lobe exchange to be important, without having to observe it directly. In addition, we would like to be able to do the reverse, that is go from complicated Lagrangian float track data to some picture of the Eulerian field. In locations where floats display hyperbolic behavior, the ideas of chaotic advection might help interpretation of complex tracks.

Needless to say, neither task is simple. The oceans are far more complicated than the laboratory for many reasons, including the existence of multiple (and changing) time scales and water masses. Nevertheless, I believe this work has made a contribution toward answering the question of whether chaotic advection could occur near hyperbolic points in the ocean. First, I have shown that exchange lobes arise in a periodic fluid flow when the unsteady time scale is on the order of the Lagrangian time scale or winding period. This is important since many time scales exist in the real ocean, and often unsteadiness occurs on a period that is comparable to the local Lagrangian time scale.

Second, I was able to find the approximate shapes of lobes. My results confirm earlier work in the heteroclinic jet geometry which indicates that stirring should reach much further into interior than into jet. This information could be helpful in interpreting tracer measurements. For example, these results would indicate that it would take a relatively long time for a signal to mix from the boundary current into the recirculation, but once there the signal would quickly spread throughout the recirculation and into the interior of the basin. This hypothesis could be tested in the ocean by comparing the time at which a tracer anomaly arrives at different offshore locations. This is done in the Abaco region by Molinari, et al. 1998. Their figure 1 shows the time at which an anomalous LSW salinity and potential temperature signal arrived at various locations within the DWBC and local meso-scale recirculation, and may in fact indicate that the tracer spreads more rapidly throughout the recirculation and into the interior than it did in initially moving from the DWBC into the recirculation. Further work with this sort of data with lobe dynamics in mind could prove fruitful.

Third, I was able to show the effects of chaotic advection in high values of effective diffusivity. Since κ_{eff} is a global measurement, it may be an easier diagnostic to apply to oceanographic data, than a local, lobe-finding effort. Of course, the question remains, if high values of κ_{eff} are found, are they related to chaotic advection or some other efficient

mixing process? It may be possible to answer that question by analyzing the spatial distribution of κ_{eff} . Due to uncertainty in the $L_e^2(C)$ functions, I did not attempt a detailed analysis of the spatial distribution of κ_{eff} , but work by Nakamura (1995, 1997) and Haynes & Shuckburgh (2000) have successfully focused on identifying barriers to mixing by analyzing the spatial distribution of κ_{eff} . This could be helpful in identifying chaotic advection since the spatial distribution of effective diffusivity or other measurements such as parcel separation or variance in the velocity field will show clear spatial inhomogeneity in fields dominated by chaotic advection. Effective diffusivity (or effective length) could be calculated from tracer data collected in the ocean if the horizontal resolution was high enough.

It seems likely that there are some regions in the ocean where chaotic advection might be a vital mechanism for mixing. Any region characterized by persistent coherent structures involving hyperbolic points may be influenced by lobe dynamics. Examples might include the region near the Flemish Cap where the interior circulation of the Labrador Sea meets the North Atlantic Current and the area around the San Salvador Spur at 24N. Float tracks in both of these regions display extremely complex, and in some cases hyperbolic, behavior. Further analysis would be required to determine whether chaotic advection is important in these areas.

There were some questions about these tank recirculations which I was unable to answer. These were: How is the travel time of a fluid particle affected by the presence or absence (and type) of a recirculation? What are statistics of individual particle trajectories? What are the Lyapunov exponents for these flows? Future work attempting to answer these questions would be valuable and could be done by tracking the paths of individual particles in a laboratory flow. Experiments incorporating unsteadiness on multiple time scales might also be interesting.

The long term goal of this type of work is to decide whether chaotic advection is an important mechanism in stirring oceanic flows. One could imagine organizing observational programs for direct observation or re-analyzing existing data sets, in addition to performing further laboratory experiments. If we were able to identify the effects of chaotic advection in one region, we might be able to extend the results to other recirculation regions, based on underlying flow configuration, unsteady time scales, etc. without direct observations. Eventually, we would like to be able to say something about the complicated Lagrangian trajectories excited by chaotic advection given a Eulerian mean flow and the

relevant unsteady time scales. We would also like to be able to say something about the Eulerian flow given the complex Lagrangian trajectories. The methods of dynamical systems, in particular the chaotic advection mechanism of lobe dynamics, could prove useful in meeting both of these goals.

Appendix A: Programming of oscillating lid forcing

In this appendix I outline the mechanical apparatus and FORTRAN code used to force the rotating lid on the sliced-cylinder laboratory tank. I first outline the mechanical system. The differentially rotating lid of the tank is forced via a band connected to a drive wheel. This drive wheel is rotated by a Superior Electric precision gear-head motor (model SE23-100-M000). The motor receives commands from a Toshiba T5200/100 computer via a MetraByte DASH-16 interface card (model 14048 REV.D3 PC6542). The motor step distance is fixed, but by specifying the time between steps through the computer system we are able to control the angular velocity of rotation.

For this application we desire a sinusoidal oscillation of the lid about a steady background rotation:

$$\Delta\Omega_{unsteady} = \Delta\Omega(1 + A_{osc} \sin(2\pi t / T_{osc}))$$

Where $\Delta\Omega$ is the (user specified) background lid rotation rate in radians/sec and A_{osc} and T_{osc} are the amplitude and period of oscillation, respectively. I control the lid motion via a FORTRAN code programmed to calculate time intervals between motor steps. I achieve the sinusoidal variation about a steady state by specifying a periodic variation in time intervals about a fixed time interval. The FORTRAN code (modified from a code originally developed by J. Salzig and O. Bokov) thus allows control of both the amplitude and the period of the oscillation.

The code translates the user specified rotation into total number of motor steps by:

$$steps = oangle(radians) \times \frac{400}{2\pi} \times grr \times drr \times cycles$$

where 'oangle' is the (user specified) total angular distance (of the lid) per oscillation, the factor 400 gives the number of motor steps per gear rotation, 'grr' specifies the gear ratio between the motor and the drive wheel, 'drr' specifies the drive ratio between the drive wheel and the lid, and 'cycles' is the (user specified) number of oscillations. For these experiments $oangle = 2\pi$ so that T_{osc} is always equal to the time it takes the lid to rotate once. Initially other oscillation periods were used, but unsteadiness was always observed at the rotation period, presumably due to some small imperfections in the glass lid. T_{osc} 'Cycles' is determined for each run depending on the desired run time.

The code then calculates the motor velocity in steps/sec needed to drive the steady component of the lid rotation rate (or background rotation rate for the oscillating case):

$$v_{con} \left(\frac{steps}{sec} \right) = \Delta\Omega \times \frac{400}{2\pi} \times grr \times drr$$

where, as above, $\Delta\Omega$ is the (user specified) lid rotation rate in radians/sec. I choose this rotation rate in order to control $\delta = \delta_l / \delta_M$, which is related to the Reynolds number of the flow in the tank (see main text). The time to wait between each step is just the inverse of this motor velocity: $t_{con} = 1/v_{con}$. For the steady case the motor movement is then accomplished by looping through the total number of steps, each time sending a 'step' command to the motor after a specific number of ticks on the computer clock. Our clock is set to 100 kHz so that a step command is sent after $ticks = t_{con} \times 100,000$.

For an oscillating velocity profile the sinusoidal component is determined from the user specified ' A_{osc} ' or amplitude of oscillation as a percentage of the background rotation rate. This component is: $v' \approx v_{con} \times A_{osc} \times \sin(m)$. Here m represents integers from 1 to

$n/4$ and n is calculated by determining the minimum array size needed to capture a sine wave of the desired amplitude(see below). Since $t' = 1/v'$ I can calculate the time steps needed to arrive at a new velocity combining the steady and oscillating components:

$$v = v_{con} + v' = \frac{1}{t_{con}} + \frac{1}{t'} = \frac{t' + t_{con}}{t' t_{con}}$$

As for the steady case the motor movement is then accomplished by looping through the total number of steps, each time sending a 'step' command to the motor after $ticks = t \times 100,000$ where $t = 1/v$.

In constructing the actual iterative process I needed to balance two computational limitations. I could have fully calculated the necessary time to wait upon each loop though the stepping process, but this would have slowed the stepping process too much. I could also have calculated and stored the entire time wait array in advance, but because the number of motor steps required to accomplish one oscillation cycle is of order one million, this array proved too large for memory. I instead balanced these needs by creating a shortened command array of time steps values. This works because the amplitude of the oscillation is small compared to the background stepping rate and the 'step' command is given after an *integer* number of ticks. The necessary range is calculated using the length of one full oscillation $nz = step/cycles$ by finding the maximum oscillation time step value:

$$t'_{max} = \left(v_{con} \times amp \times \sin \frac{(nz/4 - 1)2\pi}{nz} + 1 \right)^{-1}$$

and then finding the maximum and minimum number of ticks between steps associated with that t'_{max} . (i.e. $ticks_{max} = 100,000 \times t'_{max} \times t_{con} / (t'_{max} + t_{con})$). This range of ticks then determines the length array such that each integer value between these two is represented. This array is produced initially and then stretched over the length of the full array during the iterative process. In addition only one quarter of a wavelength of the sine wave is contained in the array and is simply mirrored in the looping process as the movement is activated.

Appendix B: Initial recirculations forced by topography in tank

In the initial stages of this investigation I considered creating recirculations along the course of the western boundary current in a few different ways. First, I attached a short O(4 cm), full-depth, meridional barrier to the western wall of the tank. As the western boundary current negotiated this obstacle it separated from the end of the barrier and rejoined the western wall further north, so that a cyclonic recirculation formed north of the barrier. I decided against this particular geometry because most of the observations of recirculations along the deep western boundary currents in the ocean were offshore of the currents. I was very interested in the interactions between the current, recirculations, and interior flow, which this geometry did not allow.

My next attempt was to force recirculations over bumps attached to the bottom of the tank. I chose cylinders or hemispheres a few cm in diameter and investigated the flow with one or two bumps sitting offshore of the western boundary current. These obstacles effectively constrained columns of fluid (Taylor columns) and the result was small-scale

offshore recirculations. The problem with this arrangement was in fact the effectiveness of the Taylor constraint. Very little exchange appeared to occur between the recirculating fluid and the fluid in the boundary current. Since it was this exchange I wished to investigate, I decided to utilize the recirculations that arise naturally in the rotating sliced-cylinder tank. There were some clear advantages to forcing the recirculations topographically. The two topographic recirculations were much more symmetric than the inertial and Munk recirculations. In addition I could investigate both the single and double recirculation geometry at identical forcing parameters (where as forcing a single Munk recirculation required $\delta = 1.00$, while the double recirculation required $\delta > 1.13$).

Further investigation of these topographic recirculations would prove very interesting, especially since a number of the recirculations observed along the actual deep boundary currents in the ocean appear to be indirectly (i.e. over bumps or depressions) or directly (i.e. by sidewalls) constrained by topography. I found the smoothest recirculation flow when I used hemispherical bumps. In addition, the bumps needed to be transparent, since in order to see the dye I lit the tank from below. I actually obtained the majority of these bumps at commercial stores, where I found cat toys, plastic Easter eggs, and packaging in the necessary shapes.

Acknowledgments:

I am grateful for funding provided by a National Defense Science and Engineering Graduate Fellowship from September 1999-January 2001 and for funding from ONR#N00014-99-1-0258 and NSF#OCE-9616949 from September 1998-August 1999.

I would like to thank the many people who have helped me with various components of this project. From the first days of brainstorming, through sorting out the laboratory apparatus and procedures, and analyzing final results many people in the Physical Oceanography Department and Rinehart Coastal Research Laboratory at WHOI assisted and guided me in various ways. My especial gratitude goes to Larry Pratt, my advisor, and Karl Helfrich, who allowed me to use his rotating tank apparatus for these experiments. I would like to thank Claudia Cenedese, John Salzig, and Judith Wells for assistance in the laboratory; Cecilie Mauritzen, Mike McCartney, and Fiamma Straneo for invaluable education in the relevant oceanographic observations; Emily Shuckburgh for insights into effective diffusivity; and Chris Jones for helpful discussions about lobe dynamics. I also affectionately thank Heather Hunt, my officemate, and my fellow students in the joint program, for camaraderie, programming tips, and general sanity maintenance. Lastly, I am deeply grateful to my parents, my brother Brian, and the other friends and family who have seen me through this, and especially Brendan Riordan, who keeps me joyful.

References:

- Adrian, R.J. Particle-Imaging Techniques for Experimental Fluid Mechanics. *Annual Review of Fluid Mechanics*. 23, 261-304 (1991).
- Beardsley, R.C. A laboratory model of the wind-driven ocean circulation. *J. Fluid Mech (JFM)*. 38, 255-271 (1969).
- Beardsley, R.C. and K. Robbins. The 'sliced-cylinder' laboratory model of the wind-driven ocean circulation. Part 1: Steady forcing and topographic Rossby wave instability. *JFM*. 69, 27-40 (1975).
- Beardsley, R.C. The 'sliced-cylinder' laboratory model of the wind-driven ocean circulation. Part 2: Oscillatory forcing and Rossby wave resonance. *JFM*. 69, 41-64 (1975).
- Bower, A.S. and H.D. Hunt. Lagrangian Observations of the Deep Western Boundary Current in the North Atlantic Ocean Part 1: Large-scale pathways and spreading rates. *JPO*. (in press).
- Bower, A.S. and H.D. Hunt. Lagrangian Observations of the Deep Western Boundary Current in the North Atlantic Ocean Part 2: The Gulf Stream-Deep Western Boundary Current crossover. *JPO*. (in press).
- Clarke, R.A. and J.C. Gascard. The formation of Labrador Sea Water. I. Large-scale processes. *JPO*. 13, 1764-1778 (1983).
- Curry, R.G., M.S. McCartney, and T.J. Swift. Oceanic transport of subpolar climate signals to mid-depth subtropical waters. *Nature*. 391, 575-577 (1998).
- del-Castillo Negrete D., and P.J. Morrison. Chaotic Transport by Rossby waves in a shear flow. *Phys. Fluids A*. 5, 948-65 (1993).
- Fine R.A. and R. L. Molinari. A continuous deep western boundary current between Abaco (26.5) and Barbados (13N). *Deep Sea Research*. 35, 1441-1450 (1988).
- Fine, R.A. Tracers, time scales and the thermohaline circulation: The lower limb in the North Atlantic Ocean. *Reviews of Geophysics*. 33 supplement, 1353-1365 (1995).
- Gana, S. and C. le Provost. Circulation and flux of the central North Atlantic in 1983/1984 estimated by inverse analysis of TOPOGULF hydrological data. *Journal of Marine Systems*. 4, 67-92 (1993).
- Griffiths, R.W. and A.E. Kiss. Flow regimes in a wide 'sliced-cylinder' model of homogeneous beta-plane circulation. *JFM*. 399, 205-236 (1999).
- Haynes, P. and E. Shuckburgh. Effective diffusivity as a diagnostic of atmospheric transport, Part I: stratosphere. *JGR*. 105 (D18), (2000).
- Hogg, N. G. On the transport of the Gulf Stream between Cape Hatteras and the Grand Banks. *DSR*. 39, 1231-1246 (1992).
- Johns, W. E., D.M. Fratantoni, and R.J. Zantopp. Deep western boundary current variability off northeastern Brazil. *DSR*. 40, 293-310 (1993).
- Johns, E., R. A. Fine, and R. L. Molinari. Deep flow along the western boundary south of the Blake Bahama Outer Ridge. *JPO*. 27, 2187-2208 (1997).
- Kawase, M. Effects of a concave bottom geometry on the upwelling-driven circulation in an abyssal ocean basin. *JPO*. 23, 400-405 (1993).
- Lavender, K.L., R.E. Davis, and W.B. Owens. (2000) Mid-depth recirculation observed in the interior Labrador and Irminger seas by direct velocity measurements. *Nature*.

- 407, 66-69 (2000).
- Leaman, K.D. and P.S. Vertes. Topographic influences on recirculation in the Deep Western Boundary Current: Results from RAFOS float trajectories between the Blake-Bahama Outer Ridge and the San Salvador "Gate". *JPO*. 26, 941-960 (1996).
- Lee, T.N., W.E. Johns, R.J. Zantopp, and E.R. Fillenbaum. Moored observations of Western Boundary Current variability and thermohaline circulation at 26.5N in the subtropical North Atlantic. *JPO*. 26, 962-982 (1996).
- Losier, M.S, L.J. Pratt, A.M. Rogerson, and P.D. Miller. Exchange geometry revealed by float trajectories in the Gulf Stream. *JPO*. 27, 2327-2341 (1997).
- Mauritzen, C. and S. Hakkinen. On the relationship between dense water formation and the "Meridional Overturning Cell" in the North Atlantic Ocean. *DSR I*. 46, 877-895 (1999).
- McCartney, M.S. Recirculating components to the deep boundary current of the northern North Atlantic. *Progress in Oceanogr.* 29, 283-383 (1992).
- Miller, P.D., C.K.R.T. Jones, A.M. Rogerson, and L.J. Pratt. Quantifying transport in numerically generated velocity fields. *Physica D*. 110, 105-122 (1997).
- Miller, P.D., L.J. Pratt, K.R. Helfrich, and C.K.R.T. Jones. Lobes analysis of an island recirculation. (submitted to *JPO*. January, 2001).
- Molinari, R.L., R.A. Fine, W.D. Wilson, R.G. Curry, J. Abell, and M.S. McCartney. The arrival of recently formed Labrador Sea Water in the Deep Western Boundary Current at 26.5N. *Geophysical Research Letters*. 25, 2249-2252 (1998).
- Munk W. and C. Wunsch. Abyssal recipes II: energetics of tidal and wind mixing. *DSR I*. 45, 1977-2010 (1998).
- Nakamura, N. Modified Lagrangian-mean diagnostics of the stratospheric polar vortices. Part 1: Formulation and analysis of GFDL SKYHI GCM. *JAS*. 52, 2096-2108 (1995).
- Nakamura, N. Two-dimensional mixing, edge formation, and permeability diagnosed in an area coordinate. *JAS*. 53, 1524-1537 (1996).
- Nakamura, N. and J. Ma. Modified Lagrangian-mean diagnostics of the stratospheric polar vortices. Part 2: Nitrous oxide and seasonal barrier migration in the CLAES and SKYHI GCM. *JGR*. 102, (D22) 25,721-25,735 (1997).
- Nof, D. and D. Olson. How do western abyssal currents cross the equator? *DSR*. 40, 235-255 (1993).
- Pedlosky, J., L. J. Pratt, M. A. Spall, and K. R. Helfrich. Circulation around islands and ridges. *Journal of Marine Research*. 55, 119-1251 (1997).
- Pedlosky, J. *Geophysical Fluid Dynamics*, 2nd ed. Springer-Verlag, New York. (1987).
- Pedlosky, J. and H.P. Greenspan. A simple laboratory model for the oceanic circulation. *JFM*. 27, 291-304 (1967).
- Pickart, R.S., D.J. Torres, and R.A. Clarke. Hydrography of the Labrador Sea during active convection. (submitted to *JPO*. June 2000).
- Pickart, R.S., et al. (Lab Sea Group) The Labrador Sea deep convection experiment. *Bulletin of the American Meteorological Society*. 79, 2033-2058 (1998).
- Pickart, R. S., M. A. Spall, and J.R.N. Lazier. Mid-depth ventilation in the western boundary current system of the subpolar gyre. *DSR I*. 44, 1025-1054 (1997).
- Polvani, L.M. and J. Wisdom. Chaotic Trajectories around an elliptical vortex patch in a constant and uniform background shear flow. *Phys. Fluids A*. 2, 123-126 (1990).

- Pratt, L.J., M.S. Losier, and N. Beliakova. Parcel Trajectories in Quasigeostrophic Jets: Neutral Modes. *JPO*. 25, 1451-1466 (1995).
- Raffel, M., C. Willert, and J. Kompenhans. Particle Image Velocimetry: a practical guide. Springer-Verlag, New York. 1998.
- Rogerson, A.M, P.D. Miller, L.J. Pratt, and C.K.R.T. Jones. Lagrangian Motion and Fluid Exchange in a Barotropic Meandering Jet. *JPO*. 29, 2635-2655 (1999).
- Rom-Kedar, V., A. Leonard, and S. Wiggins. An analytical study of transport, mixing, and chaos in an unsteady vortical flow. *JFM*. 214, 347-394 (1990).
- Schmitz, W.J. and M.S. McCartney. On The North Atlantic Circulation. *Rev. of Geophysics*. 31, 29-49 (1993).
- Spall M.A. Wave-induced abyssal recirculations. *JMR*. 52, 1051-1080 (1994).
- Spall M.A. Dynamics of the Gulf Stream/Deep Western Boundary Current crossover. Part I: Entrainment and recirculation. *JPO*. 26, 2152-2168 (1996).
- Spall M.A. Dynamics of the Gulf Stream/Deep Western Boundary Current crossover. Part II: Low-frequency internal oscillations. *JPO*. 26, 2169-2182 (1996).
- Speer, K.G. and M.S. McCartney. Bottom water circulation in the western North Atlantic. *JPO*. 22, 83-92 (1992).
- Stephens, J.C. and D.P. Marshall. Dynamical Pathways of the Antarctic Bottom Water in the Atlantic. *JPO*. 30, 622-640 (2000).
- Van Aken, H.M. The hydrography of the mid-latitude northeast Atlantic Ocean I: the deep water masses. *DSR*. 47, 757-788 (2000).
- Wiggins, S. Chaotic Transport in Dynamical Systems, Interdisciplinary Applied Mathematics, Vol. 2. Springer-Verlag. Berlin (1992).
- Wijffels, S.E., M.H. Hall, T. Joyce, D. J. Torres, P. Hacker, and E. Firing. Multiple deep gyres of the western North Pacific: A WOCE section along 149E. *JGR*. 103, (C6) 12985-13009 (1998).
- Willert, C.E. and M. Gharib. Digital Particle Image Velocimetry. *Experiments in Fluids*. 10, 181-193 (1991).
- Winters, K. and E. D'Asaro. Diapycnal flux and the rate of fluid mixing. *JFM*. 317, 179-193 (1996).